Cavitation in Blunt Traumatic Brain Injury

by

Christopher Paul Eckersley

Department of Biomedical Engineering
Duke University

Date:_____
Approved:

_____
Cameron 'Dale' Bass, Advisor

_____
Jason Luck

_____
Marc Sommer

_____
Gianmarco Pinton

_____
Joel Morgenlander

Dissertation submitted in partial fulfillment of
the requirements for the degree of Doctor
of Philosophy in the Department of
Biomedical Engineering in the Graduate School
of Duke University

2021

ABSTRACT

Cavitation in Blunt Traumatic Brain Injury

by

Christopher Paul Eckersley

Department of Biomedical Engineering
Duke University

Date:_____
Approved:

_____
Cameron 'Dale' Bass, Advisor

_____
Jason Luck

_____
Marc Sommer

_____
Gianmarco Pinton

_____
Joel Morgenlander

An abstract of a dissertation submitted in partial fulfillment of the requirements for the degree of Doctor of Philosophy in the Department of Biomedical Engineering in the Graduate School of Duke University

2021

Copyright by
Christopher Paul Eckersley
2021

Abstract

Traumatic Brain Injury (TBI) has become a marquee injury of this generation, prevalent in both military and civilian populations (Meaney 2014). Blunt impacts to the head are the known cause of approximately 1.7 million of TBI hospitalizations per year (Meaney 2014), and while mild TBI has the highest incidence (approximately 75% of TBIs) the injuries range from mild concussions to life threating severe bleeding within the brain (Meaney 2014).

Due to wide spread prominence, blunt impact TBI has garnered a wealth of academic research interest focusing on the full spectrum of the biological scale, from subcellular and cellular response, to global human body modeling. The foundational theory of current blunt impact TBI research is neurological tissue damage by simple shear strain caused by motion of the skull (Cullen 2016, Alshareef 2020). While this likely contributes to tissue damage, its global perspective does not provide a satisfactory solution to the focal symptomology of TBI etiology. This is most likely because there are less appreciated mechanisms of injury contributing to TBI such as shear shock formation or cerebrospinal fluid (CSF) cavitation.

The focus of this dissertation is to unpack the role of CSF cavitation in blunt impact TBI and contribute an important piece missing from the mechanistic understanding of TBI. This work develops an acoustic biomarker that indicates transient cavitation collapse,

uses this biomarker to investigate cavitation mechanisms, observes cavitation in fresh, non-frozen, full body pig cadaver blunt impact testing, and provides clinical implications for transient cavitation through a reanalysis of live subhuman primate seminal data. It takes advantage of the large magnitude wideband acoustic emission of transient cavitation collapse, advanced acoustic sensor technology, and novel acoustic analysis methods to uncover a piece of the mechanistic mystery surrounding blunt impact TBI.

There are five major conclusions reached in this dissertation. 1: The blunt impact head kinematics that induce cavitation are not significantly influenced by neck strength or cervical muscle activation. 2: Broadband acoustic emissions can be used as an acoustic biomarker to detect the incidence of transient cavitation collapse through the skull. 3: Compliance of the vessel containing a cavitating medium significantly influences the levels at which cavitation occurs during a blunt impact. 4: Blunt impact CSF cavitation occurs in a fresh, non-frozen, uncompromised pig cadaver head at impact levels below catastrophic injury thresholds. 5: Brain contusions are a potential clinical implication of transient cavitation collapse.

Due to a lack of tools and technology, previous work on blunt impact cavitation was restricted to experimentation with limitations prohibiting the direct study of intracranial transient CSF cavitation. This innovative work provides direct observation of blunt impact CSF cavitation that benefits tools, injury risk functions, safety device design, and detection methodologies.

Dedication

I would like to dedicate this work to my parents Tim and Sue Eckersley. Their hard work and sacrifice have provided me the freedom to pursue my scientific aspirations. Without their love and support, this would not have been possible.

Contents

Abstract iv

List of Tables xii

List of Figures xiii

Acknowledgements xvii

1. Introduction 1

1.1 Statement of the Problem 1

1.2 Clinical Significance 6

1.3 Specific Aims 9

2. Literature Review 12

2.1 Traumatic Brian Injury 12

2.1.1 Mechanisms of Traumatic Brain Injury 12

2.1.2 Clinical Definitions and Treatment 14

2.2 Neuroanatomy 17

2.2.1 Cerebrospinal Fluid and Ventricular System 17

2.2.2 Meningeal Layer 20

2.2.3 Brain Regions and Functions 22

2.3 Neck Musculature and Head Kinematics 24

2.4 Cavitation 26

2.4.1 Theory 26

2.4.2 Mechanism of Injury 32

2.4.3 Cavitation in Soft Tissues 34
2.4.4 Cavitation in Head Surrogates 34
2.4.5 Cavitation in the Brain 36
2.4.6 Outstanding Issues in Cavitation Literature 38
2.5 Acoustic Emissions 39
2.5.1 Theory 39
2.5.2 Wavelet Transform 41
3. Role of Neck Musculature in Head Kinematics 45
3.1 Objectives 45
3.2 Methods 48
3.3 Results 52
3.4 Discussion 57
3.5 Conclusions 60
4. Development of an Acoustic Biomarker for Blunt Impact CSF Cavitation 62
4.1 Objectives 62
4.2 Methods 62
4.2.1 Laser Induced Cavitation Tests 64
4.2.2 Blunt Impacting Device 65
4.2.3 Acrylic Head Surrogate 67
4.3 Results 69
4.3.1 Laser Induced Cavitation Tests 69
4.3.2 Acrylic Head Surrogate 72

4.4 Discussion 75

4.5 Conclusion 77

5. The Role of Container Compliance in Cavitation 79

5.1 Objectives 79

5.2 Methods 81

5.2.1 Acrylic Pig Head Surrogate Experimental Testing 81

5.2.2 Numerical Finite Element Modeling of Experimental Tests 85

5.3 Results 88

5.3.1 Acrylic Pig Head Surrogate Experimental Results 88

5.3.2 Numerical Finite Element Modeling Results 92

5.4 Discussion 96

5.5 Conclusions 102

6. Blunt Induced Cavitation in a Pig Model 103

6.1 Objectives 103

6.2 Methods 104

6.2.1 Repetitive Impacts for Cavitation Detection 104

6.2.2 Perfused Pig Cadaver to Investigate Clinical Implications of Cavitation ... 108

6.3 Results 110

6.3.1 Repetitive Impacts for Cavitation Detection 110

6.3.2 Perfused Pig Cadaver to Investigate Clinical Implications of Cavitation ... 115

6.4 Discussion 119

6.5 Conclusions 126

7. Clinical Implications of Cavitation in the Human Population 128

7.1 Objectives 128

7.2 Methods 129

7.2.1 Methodology of Live Animal Tests in Literature Investigating Intracranial Bleeding 129

7.2.1.1 Ommaya *et al.* - 1968 130

7.2.1.2 Ommaya *et al.* - 1971 131

7.2.1.3 Gennarelli *et al.* - 1972 131

7.2.1.4 Gennarelli *et al.* - 1979 133

7.2.1.5 Ono *et al.* - 1980 133

7.2.2 Finite Element Modeling of Past Experimental Conditions 134

7.2.3 Retrospective Study of Brain Bleed Cases 135

7.3 Results 136

7.3.1 Results of Live Animal Tests in Literature 136

7.3.1.1 Ommaya *et al.* - 1968 136

7.3.1.2 Ommaya *et al.* - 1971 137

7.3.1.3 Gennarelli *et al.* - 1972 138

7.3.1.4 Gennarelli *et al.* - 1979 139

7.3.1.5 Ono *et al.* - 1980 139

7.3.2 Finite Element Modeling Results 140

7.3.3 Retrospective Study of Brain Bleed Cases 143

7.4 Discussion 144

7.5 Conclusions 154

8. Conclusions 156

8.1 Major Contributions 156

8.2 Minor Contributions 159

8.3 Future Work 160

References 162

Biography 176

List of Tables

Table 2-1: Standard Galsgow Coma Scale Scoring (Teasdale, 1974) 14

Table 2-2: CSF Constituent Composition 18

Table 2-3: Functions of the Cortex Lobes (Kandel, 2013) 23

Table 2-4: Gross Brain Regions and Associated Function 24

Table 3-1: Specifications of Head Impactors 49

Table 3-2: Impactors and Initial Velocities for Impact Scenarios 50

Table 4-1: Material Properties of Acrylic and Skull 68

Table 5-1: Material properties for elastic materials 87

Table 5-2: Fluid material properties and Mie-Grüneisen constants 87

Table 5-3: Alternative compliance cases and material properties 88

Table 6-1: Quartile Risks of Cavitation of Four Injury Metrics 115

Table 7-1: Summary of Live Animal Testing Investigating Intracranial Bleeding 130

Table 7-2: Summary of Acceleration Magnitudes (Gennarelli, 1972) 132

Table 7-3: Summary of SIMon Model Impact Conditions 135

List of Figures

Figure 1-1: Six Clinical Profiles of Concussion (Collins, 2014) 7

Figure 2-1: Ventricular System of the Human Brain (Wikimedia Commons) 19

Figure 2-2: Diagram of the Meningeal Layer 21

Figure 2-3: Illustration of Brain Lobes (Wikimedia Commons) 22

Figure 2-4: Example phase diagram illustrating cavitation and boiling 27

Figure 2-5: Cavitation bubble radius for low (green) and high (blue) driving pressure (Shmuel Ben-Ezra, Wikimedia Commons) 31

Figure 2-6: Illustration of damaging phenomena upon cavitation collapse 33

Figure 2-7: Representative plots of the Morlet wavelet in time and frequency domains . 44

Figure 3-1: (a) Sagittal view of the impact locations tested. 51

Figure 3-2: Peak resultant linear acceleration and peak resultant angular acceleration injury metrics for different neck activation states 55

Figure 3-3: Peak resultant linear acceleration and peak resultant angular acceleration injury metrics for different neck experimental testing conditions 56

Figure 4-1: Distribution of the acoustic noise prior to blunt impact. 64

Figure 4-2: Drawing of water tank setup for laser-induced cavitation tests. 65

Figure 4-3: (A) Illustration of overall blunt impactor. (B) Picture of impactor used for blunt tests. 67

Figure 4-4: Coup (Left) and contre-coup (Right) of full sized surrogate. Accelerometer mounted on the coup and acoustic sensors mounted on contre-coup. 68

Figure 4-5: Laser induced positive cavitation 70

Figure 4-6: Wavelet transform of hydrophone signal from laser induced cavitation formation 71

Figure 4-7: Negative control of laser induced cavitation. 71

Figure 4-8: Blunt impact positive cavitation large bubble 73

Figure 4-9: Blunt impact positive cavitation small bubble 74

Figure 4-10: Wavelet transform of blunt impact negative control test 75

Figure 5-1: Comparison of contre-coup pressures in a rigid vessel with and without a membrane 80

Figure 5-2: Images of the pig head surrogate 82

Figure 5-3: Labeled diagram of the numerical finite element model. 87

Figure 5-4: A: Representative wavelet transform of cavitation collapse in pig head surrogate 89

Figure 5-5: HIC cavitation risk plots 90

Figure 5-6: Peak resultant linear acceleration cavitation risk plots 91

Figure 5-7: Peak resultant angular acceleration cavitation risk plots 91

Figure 5-8: HIP cavitation risk plots of the foramen (black, AD score = 56.4) and solid (grey, AD score = 25.8) pig head acrylic surrogates. 92

Figure 5-9: Comparison of the resultant linear accelerations the numerical model and the experiment 93

Figure 5-10: Pressure comparison of the average of four elements on the contre-coup ... 93

Figure 5-11: Increasing container stiffness increases contre-coup strain frequency 94

Figure 5-12: Comparison of contre-coup wall strain and adjacent pressure for model with a container stiffness of 300 kPa 95

Figure 5-13: Comparison of contre-coup wall strain and adjacent pressure for acrylic model, container stiffness of 3,000 kPa 95

Figure 5-14: Comparison of contre-coup wall strain and adjacent pressure for container stiffness of 30,000 kPa 96

Figure 5-15: Cross correlation analysis comparing contre-coup pressure traces of same level impact of the finite element model with and without silicon membrane. 99

Figure 6-1: A) Illustration of surgical cut sites on cadaver pig head. B) Sensor mounting points on cadaver skull. C) Impact location of cadaver head in all tests. 105

Figure 6-2: Cannulation of carotid artery and external jugular vein. 109

Figure 6-3: Example wavelet transform of positive cavitation in cadaveric pig 110

Figure 6-4: Example wavelet transform of negative cavitation from full body pig cadaver tests. 111

Figure 6-5: Wavelet transform of acoustic signal in an air filled cranium negative control 112

Figure 6-6: Wavelet transform of the acoustic signal in a rigid polyurethane filled cranium negative control 112

Figure 6-7: Cavitation risk plot of HIC for cadaveric pig 113

Figure 6-8: Cavitation risk plot of angular accel. for cadaveric pig 114

Figure 6-9: Cavitation risk plot of linear accel. for cadaveric pig 114

Figure 6-10: Cavitation risk plot of HIP for cadaveric pig 115

Figure 6-11: Wavelet transform of perfused pig head impact test showing acoustic biomarker positive for cavitation collapse. 116

Figure 6-12: Wavelet transform of perfused pig head impact test that does not show acoustic biomarker of cavitation collapse. 117

Figure 6-13: Superior (Left) and inferior (Right) images of the fixed pig cadaver brain following perfusion of Evans blue. 118

Figure 6-14: Close up images of the parenchyma on the impact coup 118

Figure 6-15: Images of 5 mm brain slices for positive cavitation (Left) and negative cavitation (Right) tests. 119

Figure 6-16: Comparison of wavelet transforms between high and low frequency sensors from positive cavitation pig cadaver blunt impact test 124

Figure 7-1: Peak angular acceleration and duration of 40 impact tests (Ommaya, 1968) 130

Figure 7-2: Frontal and occipital impact sites directed approximately through the head center of gravity (Ommaya, 1971) 131

Figure 7-3: Illustration based on Ommaya *et al.* of the combined bleeding locations of all 15 tests that resulted in macroscopic damage 136

Figure 7-4: Lateral (left), ventral (center), and dorsal (right) illustrations of cumulative contusion and bleeding locations 137

Figure 7-5: Results of a study investigating stress concentrations due to rotation in the sagittal plane based on Ommaya *et al.* 138

Figure 7-6: Peak pressure distribution from an occipital impact 141

Figure 7-7: Peak strain distribution from an occipital impact 141

Figure 7-8: Peak pressure distribution from a frontal impact 142

Figure 7-9: Peak strain distribution from a frontal impact 142

Figure 7-10: Peak pressure distribution from a lateral impact 143

Figure 7-11: Peak strain distribution from a lateral impact 143

Figure 7-12: Peak negative pressure distributions in MPa of the same kinematic inputs for a frontal impact vs an occipital impact. 147

Figure 7-13: Peak effective strain distributions for an occipital and frontal impact with the same magnitude kinematic inputs. 148

Figure 7-14: Comparison diagram of pressure distributions from finite element modeling and contusion locations from Ommaya *et al.* 150

Figure 7-15: Comparison diagram of brain surface strain distributions from finite element modeling and subdural bleed locations from Ommaya *et al.* 152

Acknowledgements

I would like to thank my parents, Tim and Sue, for their love and support throughout this journey. Your sacrifice and hard work provided the foundation for me to build this work, and you are the inspiration that guide my endeavors. Next, thank you Maddie, Laura, Aunt Cindy, Uncle Hal, Grandma and Papa. Your open ear and thoughtful messages have meant the world, and lifted me during challenging moments. To my day one graduate friends: who knew a bunch of renegades would teach me so much about nature, friendship, and myself. I love you all and cannot wait for the amazing places we go. To the Injury Biomechanics Lab: Jay, Allison, Allen, Brian, Courtney, Maria, Joost, Mitchell, and Connie, there is no way I make it through the late nights, long days, and stressful presentations without the coffee breaks, support, and insightful contributions. Jason Kait, without your work and support I do not think the lab runs let alone any of my projects! I am forever grateful of your help, guidance, and friendship. Jason Luck, I cannot thank you enough for bringing me into the lab as a junior, I will never forget our first meeting in the prep room that sent me down the path of research. You have become both an insightful mentor and incredible friend. Dale, you have been the most supportive and understanding advisor that I could have ever asked for. I am proud to be a part of your research lineage, and honored to have you in my corner. To Steve and Greg, I cannot thank you all enough for the support and assistance you have provided to me in the machine shop since I was an undergraduate. Because of you two, I always had

a safe, fun, and productive time in the shop. At some point, I promise I will pay off all the vanilla milkshakes I have on my tab. To Lainie, Diego, and the teams up at the vivarium, I cannot thank you enough for your support and providing the tissue that was paramount to this work. Finally, thank you to my adventure partner Sami. You are a shining light in my life that has pushed me to the finish; I cannot wait to see what life has in store next!

1. Introduction

1.1 Statement of the Problem

Traumatic Brain Injury (TBI) has become a marquee injury of this generation, prevalent in both military and civilian populations (Meaney 2014). Recent literature (Lo 2020) indicates there is a reported age standardized rate of 605 TBIs per 100,000 United States citizens (James 2019), resulting in 2.9 million TBI related emergency department visits, hospitalizations, or deaths among all ages (CDC 2014) and approximately 17.4 billion dollars in direct injury related costs (Finkelstein 2006). Blunt impacts to the head were the known cause of approximately 1.7 million of these TBI hospitalizations (Meaney 2014), and while mild TBI has the highest incidence (approximately 75% of TBIs) the injuries range from mild concussion to severe bleeding within the brain (Meaney 2014).

When broken down by mode of injury, blunt impact TBI plagues populations in society differently. Based on United States adult emergency department visit data from 2014, ages 15 – 34 had the highest rates of TBI from motor vehicle crashes and being unintentionally struck by or against an object (200 and 172 cases per 100,000 population respectively), while ages 65+ saw highest rates of TBI due to unintentional falls (912 per 100,000 population) (CDC 2014). These three modes account for 78% of TBIs seen in the civilian population (CDC 2014).

These modes vary in a military population that experiences different daily threats. While personnel are in garrison, these same modes (motor vehicle crash, struck by object,

falls) account for approximately 53% of TBI while an additional 15% are caused by parachute accidents (Regasa 2019). However, in garrison TBI accounts for only 45% of military TBI injury, the remaining 55% occur when military personnel are deployed (Regasa 2019). When deployed, 66% of TBI are due to blast wave exposure (Regasa 2019). Despite the prevalence of blast induce TBI in deployed populations, blunt impact TBI remains a pertinent injury mode for military personnel.

Due to wide spread prominence, blunt impact TBI has garnered a wealth of academic research interest focusing on the full spectrum of the biological scale, from subcellular and cellular response to global human body modeling. Despite the varied range of focus, current research on blunt impact TBI can be categorized into several overarching questions of interest (Meaney 2014): What are the loading conditions that result in TBI? How are these loads transferred to the brain, and what characteristics of an impact are strong predictors of neurotrauma? What are the mechanisms by which neurological damage results in acute symptomology? What mechanisms of injury result in the greatest functional impairments, and do these have chronic injury consequences?

Despite the increased understanding of TBI etiology achieved, satisfactory conclusions to these fundamental questions continue to evade the research field. This research problem can seem unbounded in magnitude due to the complexity of the impact variables, neurological system, and human variability. However, when particular hurdles are cleared, a more nuanced understanding of blunt impact TBI will be reached.

The first is experimental technology to enable accurate experimentation and assessment in living models. The complexity of the neurological system makes it difficult to create biofidelic surrogates for study, meaning *in-vivo* experimentation is essential to a nuanced understanding of TBI etiology. In the past decade, injury biomechanics has witnessed vast improvements in on field sensor technology, real time imaging techniques, and symptomology diagnosis and treatment (Sussman 2016, O'Connor 2017, Kontos 2018, Knutsen 2020). However, these technologies still have not achieved satisfactory levels of accuracy, reliability, and repeatability.

For example, the limitations of these technologies have made it difficult to reach a consensus on the *in-vivo* properties of neurological tissue (Chatelin 2010). Furthermore, due to the brain's anatomical complexity, the field has not tested properties of many brain structures vital to TBI etiology, such as the interface between the skull, dura, and subdural space. This has made it challenging to understand the interaction of neurological structures under blunt impact loading. The accuracy of finite element models, a state of the art tool for TBI research, hinges on the understanding of these material properties and interactions. Until the field has achieved this understanding, the conclusions drawn from finite element models will be limited, regardless of the model's anatomical granularity.

These issues are primarily relevant to a large portion of TBI research focused on determining loading thresholds for injury. However, understanding the mechanisms by which these loading conditions damage tissue is equally important to unraveling the

complex etiology of TBI. The foundational theory for current injury threshold research is neurological tissue damaged caused a by a shear wave generated from rotational motion of the skull (Cullen 2016, Alshareef 2020). While this likely contributes to tissue damage, its global perspective does not provide a satisfactory solution to the focal symptomology of TBI etiology. This is most likely because there are less appreciated mechanisms of injury also contributing to TBI such as shear shock formation, and cerebrospinal fluid (CSF) cavitation.

The focus of this dissertation is to unpack the role of CSF cavitation in blunt impact TBI, and contribute an important piece missing from the mechanistic understanding of TBI. CSF cavitation was first proposed as a mechanism of injury in the 1950's, and has since been shown to have implications for neurological tissue damage if CSF cavitation occurs within the skull (Canchi 2017, Haniff 2017, Rapet 2019, Dougan 2020). However, whether CSF cavitation occurs under blunt impact loading conditions remains an unsettled question in the biomechanics community (Nusholtz 1997, Takhounts 2008, Singh 2015). This is due to two primary reasons; from a finite element modeling approach, the pressure threshold for CSF cavitation is debated due to the difficulty of recreating biofidelic conditions of *in-vivo* CSF (Takhounts 2008, Singh 2015, Salzar 2017). From an experimental approach, the skull serves as a barrier for observing cavitation phenomenon in the head with state of the art imaging techniques. This requires experimental methods

to use surrogates whose lack of biofidelity limits conclusions (Nusholtz 1995, Nusholtz 1997, Canchi 2017, Haniff 2017, Rapet 2019).

The collapse of transient cavitation bubbles have been shown to generate wideband point source acoustic emissions upon collapse (Young 1989). These cavitation acoustic emissions have been shown to be audible and highly specific, indicating cavitation formation can be identified from its acoustic output (Ilyichev 1989). Due to recent advances in acoustic sensing technology, literature has used acoustic emissions in the 1-3 MHz range to detect cavitation in soft tissue (Coleman 1996, Zhong 1997, Carstensen 2000, Li 2019). Due to the acoustic impedance mismatch and the viscoelastic properties of the skull and surrounding tissues, acoustic waves at these frequencies can be attenuated 10-30 dB through the skull, making them difficult to differentiate from noise (Fry 1978, Eckersley 2020). Lower frequencies emitted by cavitation collapse, while able to pass through the skull with less damping, are potentially not distinguishable from structural response of other events surrounding the impact. Because of this, any acoustic cavitation signal needs to be decomposed appropriately in both time and frequency space.

The wavelet transform is a technique for analyzing acoustic data in time and frequency space simultaneously. To determine frequency information, the acoustic signal is decomposed using a mother wavelet with particular frequency content that is compressed and dilated at a particular location in the signal. The technique translates each transformation through the signal to provide correlation values between the signal and

wavelet at given points in frequency and time.

To answer fundamental questions on the presence of cavitation in the brain under blunt impact loading, this work investigates the role of neck musculature in cavitation formation, develops an acoustic biomarker that indicates transient cavitation collapse, uses this biomarker to investigate cavitation mechanisms, observes cavitation in fresh, non-frozen, full body pig cadaver blunt impact testing, and provides clinical implications for transient cavitation through a reanalysis of live subhuman primate seminal data. It takes advantage of the large amplitude wideband acoustic emission of transient cavitation collapse, advanced acoustic sensor technology, and novel acoustic analysis methods to uncover a piece of the mechanistic mystery surrounding blunt impact TBI. Blunt impact TBI is a problem plaguing both civilian and military populations, and a foundational understanding of the injury mechanisms is pertinent to the development of preventative technologies, detection devices, and treatment plans.

1.2 Clinical Significance

With the rapid increase in awareness of the morbidity of less severe blunt impact TBI and the increased understanding of its acute and chronic effects on civilian and soldier health, it is imperative to develop a nuanced mechanistic understanding of TBI. Current state of the art clinical understanding of TBI has become refined with precise definitions, various subsets of TBI diagnosis, and patient specific treatment plans (Collins 2014, Kontos 2018, Doperak 2019). Clinicians have identified signs and symptoms of TBI that

span a breadth of impairments including cognitive, physical, emotional, and sleep (Kontos 2018). As an example, over 23 common symptoms have been identified for concussion alone, 11 of which warrant immediate medical attention (Kontos 2018). These do not even consider more severe injuries such as diffuse axonal injury and brain bleeds. Based on the treatment of thousands of patients, clinicians have grouped these symptoms into six clinical profiles (Figure 1-1). Patients then receive a specific active rehabilitative treatment plan based on which profiles their symptoms fall into and whether the profile is primary, secondary or tertiary.

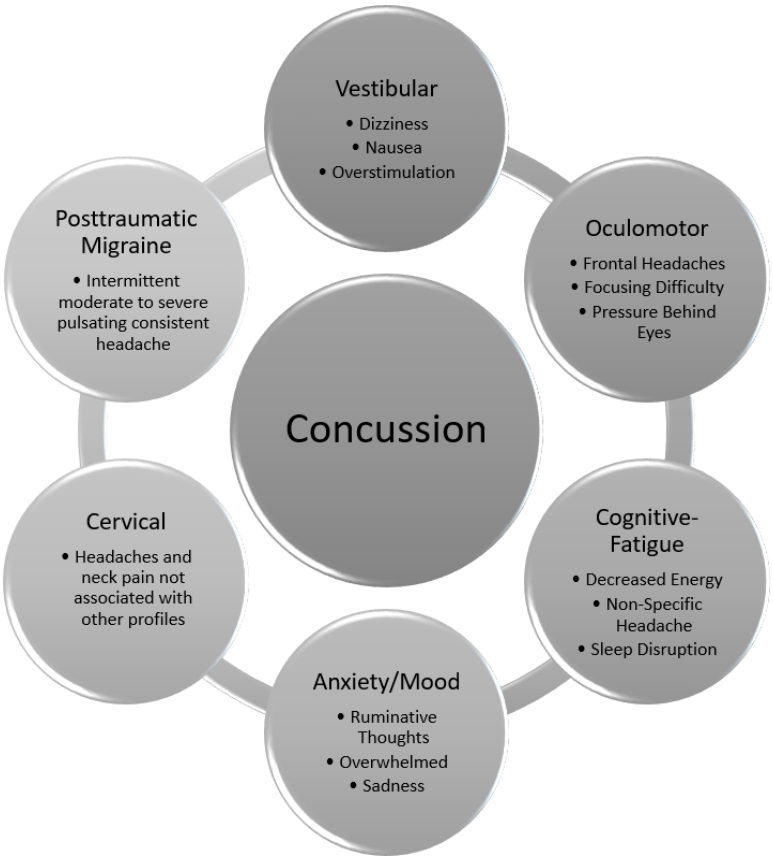

Figure 1-1: Six Clinical Profiles of Concussion (Collins 2014)

However, the mechanistic understanding of TBI does not currently capture this clinical refinement, limiting the effectiveness of injury criterion and prevention strategies. This work aims to investigate and uncover a particular mechanism of injury, cavitation. The work will: elucidate impact conditions that cause cavitation, determine where in the head cavitation is likely to cause injury, and uncover the specific pathology of cavitation. This work is imperative to transitioning the biomechanical understanding of TBI as a holistic injury, to a nuanced one, that provides specific injury locations from particular mechanisms. This will enable increasingly effective injury criterion, injury prevention strategies, and protective equipment.

My work is clinically significant because it provides an acoustic biomarker for the incidence of TBI within the head, a novel component to the toolbox of TBI detection and analysis. This differs from current TBI tools by providing the biofidelity of an uncompromised skull cavity as seen in epidemiology studies, with specific mechanistic motivation of the limited experimental methods. This work serves as a cornerstone for the development of more useful research tools, sensitive injury risk functions, effective safety devices, and accurate detection methods. This work will bolster the mechanistic understanding of TBI closer to the clinical refinement of the injury, and aid to propel clinical diagnosis and treatment of TBI even further.

1.3 Specific Aims

The objective of this dissertation is to complete a series of experiments that will deepen the understanding of a particular blunt impact TBI mechanism, CSF cavitation. This work develops a new tool for intracranial cavitation detection, uses this to detect blunt impact cavitation in a full body pig cadaver model, and provides clinical implications for CSF cavitation given a reanalysis of seminal live animal tests using modern tools and cavitation theory. The results of this work elucidate the blunt impact loading conditions that produce CSF cavitation and how this loading contributes to a particular TBI etiology. I used finite element modeling, surrogate model experiments, cadaveric pig testing, and retrospective data analysis to achieve this objective. The specific aims of this dissertation include:

1. *Investigate the role cervical muscle strength plays in blunt impact head kinematics and the biofidelity of common experimental neck conditions.*
2. *Develop and validate an acoustic signature for blunt induced cavitation formation through controlled model experiments.*
3. *Determine the role container compliance plays in transient cavitation to understand cavitation in biological systems.*
4. *Investigate cavitation formation under blunt impact in a cadaver pig model using this acoustic biomarker.*

5. *Reanalyze seminal live subhuman primate head injury data to provide novel insight to clinical implications of transient cavitation.*

I will use the results of these specific aims to inform these hypotheses:

1. Head kinematics do not vary with neck activation due to low short term human head-to-neck coupling; because of the lack of coupling, free-head experimental conditions have higher biofidelity than Hybrid III necks.
2. Upon collapse, cavitation bubbles will emit a wideband acoustic emission that is distinguishable from blunt impact noise and detected across the skull.
3. Blunt impact causes shear waves in a compliant container, generating transient localized volume increases, resulting in localized contre-coup pressure decreases.
4. Transient cavitation acoustic emissions can be detected through uncompromised pig cadaver heads, and intracranial CSF cavitation occurs at impact levels below catastrophic injury thresholds.
5. Reanalysis of seminal live subhuman primate testing with novel tools and cavitation theory will provide insight to clinical implications of CSF cavitation.

The achievement of these aims provides an innovative contribution to understanding the biomechanics of injury in the brain. This work provides a novel tool, an acoustic biomarker defined by frequency content and temporal location with respect to the impact event. This alleviates many of the limitations of previous experimental methods and enables blunt impact cavitation testing in a novel model, the

uncompromised head of a cadaveric pig. These tests provide empirical evidence for the presence of cavitation during blunt impact loading, and translate the injuries seen during positive cavitation tests to injuries observed in previous live subhuman primate testing. This innovative work provides a foundation for research tools, injury risk functions, safety device design, and detection methodologies.

2. Literature Review

This literature review summarizes the current body of work pertinent to this dissertation. I investigate traumatic brain injury mechanisms and clinical status, relevant neuroanatomy, cavitation theory and its potential for injury, and acoustic emission theory. This literature review provides context for the work presented in this dissertation and is a sampling of the full body of work on these topics.

2.1 Traumatic Brian Injury

2.1.1 Mechanisms of Traumatic Brain Injury

Two major loading modes can contribute to TBI, blunt impacts and primary blast wave loading. Blunt impact to the head results in an inertial transfer of momentum and energy that causes skull deformation and transformation that transmit stresses to the brain. This deformation and transformation produces damage in the brain through two potential primary mechanisms: pressure gradients due to linear compression waves that create predominantly tensile stresses, and tissue shear stress from rotational motion of the skull (Unterharnscheidt 1971, Thibault 1985, Margulies 1992, King 2003, Alshareef 2020). Biomechanics literature has decades of discussion on the relative importance of linear and angular acceleration of the skull in predicting TBI. In reality, however, since the skull is not a perfect sphere, 'pure' translational motion of the skull will produce rotational local strains in the brain, and large 'pure' rotational motions about the head center of gravity are not feasible owing to the head connection to the neck. So, both potentially play a role

in TBI in various combinations, as the complex geometry and anatomy create linear and rotational localized accelerations, regardless of kinematic input.

There are two additional, potential mechanisms of injury hypothesized to play a role in blunt impact TBI; formation and focusing of shear shock waves and CSF cavitation. While historically underappreciated in the biomechanics community, the presence of shear shock in the brain has recently been shown under physiologically relevant distances and kinematic inputs (Giammarinaro 2016, Espindola 2017, Giammarinaro 2018, Bigler 2020). The shear speed of sound in brain is approximately three orders of magnitude lower that the compressive speed of sound (2-5 m/s vs. 1500 m/s). This combined with brain nonlinear viscoelastic properties result in shear shocks forming in *ex-vivo* brain within a few centimeters of wave initiation (Espindola 2017, Bigler 2020). Furthermore the geometric curvature of the skull focuses and strengthens the inward propagation of shear waves, magnifying the effect of shear shocks (Giammarinaro 2018). While CSF cavitation has been theorized as a mechanism of TBI since the mid 1900's, recent advancements in experimental technology have enabled the further study of this phenomenon. Since it is the focus of this dissertation, a later section is dedicated to the review of cavitation as a mechanism of TBI.

Because the mode of loading for primary blast wave TBI is energy based with small brain strains to produce failure (Panzer 2012), very little deformation or translation of the skull occurs. Instead, the mechanism of injury is the phenomenon surrounding the

transfer of a high-speed pressure wave through the head. Specifically, localized stresses that arise at acoustic impedance mismatch interfaces and CSF cavitation from localized negative pressures (Bass 2012, Panzer 2012, Yu 2019). While primary blast wave TBI is not the focus of this dissertation, work investigating cavitation in blast injury laid the foundation for the acoustic tools and analysis used in this study (Yu 2019).

2.1.2 Clinical Definitions and Treatment

TBI is defined as a traumatically induced structural injury and/or physiologic disruption of brain function as a result of an external force (DoD 2009). The severity of TBI is often determined using the Glasgow Coma Scale (GCS) (Teasdale 1974) with grades of severe, moderate, or mild (McKee 2015). The GCS assigns a score 3-15 with higher values being less severe. Scores are determined based on clinically assessed values of ocular, verbal, and motor function (Table 1) (Teasdale 1974).

Table 2-1: Standard Galsgow Coma Scale Scoring (Teasdale 1974)

Eye Opening	Best Verbal Response	Best Motor Response
Spontaneous – 4	Orientated – 5	Obeying – 5
To Speech – 3	Confused – 4	Localizing – 4
To Pain – 2	Inappropriate – 3	Flexing – 3
None – 1	Incomprehensible – 2	Extending – 2
	None – 1	None – 1
Total GCS Score: 3 (Severe) – 15 (Mild)		

Severe TBI, associated with GCS scores of 3-8, is related to poor prognosis such as neurological disability, vegetative state, and death (McKee 2015). Symptoms of severe TBI are often due to subdural or subarachnoid bleeding, brain contusions, diffuse axonal

injury (DAI), or penetrating injuries. Commonly, patients with severe TBI have high risk of secondary brain injuries, particularly brain swelling (Hukkelhoven 2006). Acute treatment of severe TBI often requires sedation and management of intracranial pressure (ICP) through osmotherapy or extensive decompressive craniotomies (Maas 2008).

While moderate TBI, associated with GCS scores from 9-12, often results from the same injuries as severe TBI (subdural or subarachnoid bleeding, DAI, or brain contusions), patients experience more subdued symptoms such as lethargy and stupor. Moderate TBI is often treated similar to severe TBI; a CT scan determines the extent of bleeding and structural damage, and the patient is monitored to manage ICP levels. Due to the nature of trauma that causes moderate TBI, patients need to be closely observed because symptoms can quickly progress from moderate to severe.

Mild TBI (mTBI), associated with GCS scores from 13-15, accounts for an estimated 75-85% of TBIs (CDC 2003). While mTBI is often associated with no brain imaging changes, behavior consequences can have substantial morbidity. Because of this, many believe 'mild' to be a misnomer, as the injury is only mild in gross anatomical change to the brain, not in patient clinical symptomology (Kontos 2018). Therefore, mTBI is more commonly referred to as concussion by clinicians, as it provides a more precise reference to the context of the underlying mechanisms (McCrory 2017). Because it is not associated with the same gross physiological changes observed in moderate and severe TBI, concussion is more difficult to define resulting in a range of historical clinical definitions

(McCrory 2017, Kontos 2018). However, the closest consensus on a clinical definition arises from the Fifth International Conference on Concussion, where a group of healthcare specialists and sports organizations developed a consensus statement (McCrory 2017):

"Sport related concussion is a traumatic brain injury induced by biomechanical forces. Several common features that may be utilized in clinically defining the nature of a concussive head injury include:

- *SRC may be caused either by a direct blow to the head, face, neck or elsewhere on the body with an impulsive force transmitted to the head.*
- *SRC typically results in the rapid onset of short-lived impairment of neurological function that resolves spontaneously. However, in some cases, signs and symptoms evolve over a number of minutes to hours.*
- *SRC may result in neuropathological changes, but the acute clinical signs and symptoms largely reflect a functional disturbance rather than a structural injury and, as such, no abnormality is seen on standard structural neuroimaging studies.*
- *SRC results in a range of clinical signs and symptoms that may or may not involve loss of consciousness. Resolution of the clinical and cognitive features typically follows a sequential course. However, in some cases symptoms may be prolonged.*

The clinical signs and symptoms cannot be explained by drug, alcohol, or medication use, other injuries (such as cervical injuries, peripheral vestibular dysfunction, etc) or other comorbidities (eg, psychological factors or coexisting medical conditions)."

In sports, concussion was historically something to play through, or 'shake off' (Kontos 2018). When it was treated, patients were often prescribed rest with isolation or even sensory deprivation (sitting in a dark room), with mixed results (Kontos 2018). Recently, clinical treatment of concussion has shifted to a more active approach through rehabilitation based on particular symptomology. Collins and Kontos have built a novel treatment model that combines and formalizes innovative treatment strategies by clinicians (Collins 2014). The model breaks down the injury into six clinical profiles (Figure 1-1) based on characterizations of symptoms, impairments, risk factors, and clinical outcomes. A concussion patient is given a diagnosis that consists of any combination of the six profiles with primary, secondary, and tertiary designation. This provides a map for a targeted treatment plan with active intervention and rehabilitation strategies for motor and psychological deficits.

2.2 Neuroanatomy

This section reviews particular brain regions potentially vulnerable to cavitation injury, discussing structure, function, and symptomology that may result upon damage.

2.2.1 Cerebrospinal Fluid and Ventricular System

Cerebrospinal fluid (CSF) is the primary interface with brain matter making it a crucial component in understanding brain biomechanics. CSF surrounds and permeates the brain located in the subarachnoid space and ventricles. It is a clear fluid composed

primarily of water with small amounts of proteins, electrolytes, sugars, dissolved gasses, and other biological constituents (Table 2).

Table 2-2: CSF Constituent Composition

Molecule	CSF Composition
Water	99%
Sodium	138 mEq/L
Potassium	2.8 mEq/L
Chloride	119 mEq/L
Bicarbonate	22 mEq/L
Phosphorus	1.6 mg/dL
Calcium	2.1 mEq/L
Magnesium	2.3 mEq/L
Iron	1.5 g/dL
Urea	4.7 mmol/dL
Creatinine	1.2 mg/dL
Uric Acid	0.25 mg/dL
Carbon Dioxide Tension	47 mmHg
pH	7.33
Oxygen	43 mmHg
Glucose	60 mg/dL
Lactate	1.6 mEq/L
Pyruvate	0.08 mEq/L
Proteins	0.035 gm/dL

CSF experiences a complicated cycle of creation, flow, and absorption through the nervous system that indicates a more complex role than a protective buffer for the brain (Barshes 2005). Circulation of the CSF appears to act as a waste removal tool for the brains extracellular fluid, similar to the lymphatic system for other organs. Circulating CSF removes fat soluble, fat insoluble, and toxic molecules to maintain homeostasis within the brain (Barshes 2005)

Cavitation is hypothesized to occur in the CSF for two reasons. First, since it is composed of primarily water and few tissue components, it has slightly lower bulk modulus than all other brain components (neurological tissue, skull, dura, vasculature) (McElhaney 1973, Ganpule 2018). Lower bulk modulus indicates a lower speed of sound (Equation 2.1).

$$Speed\ of\ Sound = \sqrt{\frac{Bulk\ Modulus}{Density}} \qquad \text{Equation 2.1}$$

The shift from stable to transient cavitation occurs as the collapse speed of the bubble wall approaches the speed of sound in the material (Young 1989). This means transient cavitation is more likely to occur for a given bubble size in a material with a lower bulk modulus. Second, CSF is found in brain regions most susceptible to large negative transient pressure during a blunt impact. Experimental and modeling studies indicate largest negative pressures occur in boundary regions near the skull and locations of acoustic impedance change, such as the ventricles (Nusholtz 1995, Panzer 2012).

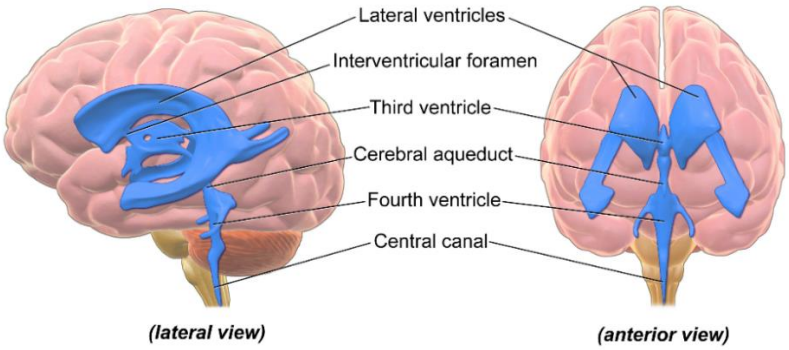

Figure 2-1: Ventricular System of the Human Brain (Wikimedia Commons)

The ventricular system of the brain is responsible for the production, transport, and removal of CSF and consists of four ventricles, two lateral, and two along the midline of the brain (Figure 2-1). The two lateral ventricles occupy large portions of the cerebrum and are located between the cerebrum and deep brain structures. The lateral ventricles both drain to the third ventricle, a slit like cavity along the midline of the brain between the halves of the diencephalon. The third ventricle connects to the fourth ventricle, a pyramid-like structure located on the anterior portion of the cerebellum. From the fourth ventricle, CSF drains to the subarachnoid space and down the spinal cord (Moore 2014).

2.2.2 Meningeal Layer

The meningeal layer consists of connective tissues that surround the brain and central nervous system components, separating them from overlying bone. The meninges serves three primary functions: protects the brain, provides supporting network for arteries, veins, and venous sinuses, and encloses the CSF filled subarachnoid space (Moore 2014). Three distinct membranes compose the meninges, the dura mater, arachnoid mater, and pia mater (Figure 2-2).

The dura mater (dura) is a thick, dense, fibrous, bilaminar membrane. The external periosteal layer adheres directly to the internal surface of the cranium, while the internal meningeal layer serves as a supporting layer, following the external surface of the brain. The two layers are intimately fused except where the dural sinuses and infoldings occur. The dural infoldings are influential to brain biomechanics by creating a material mismatch

between the stiffer dura and softer nervous tissue. The most significant infoldings are the falx cerebri (the infold that runs down the longitudinal cerebral fissure and separates the two brain hemispheres) and the tentorium cerebelli (the infold that meets the falx cerebri at the posterior of the brain and separates the occipital lobes and cerebellum) (Jones 2010).

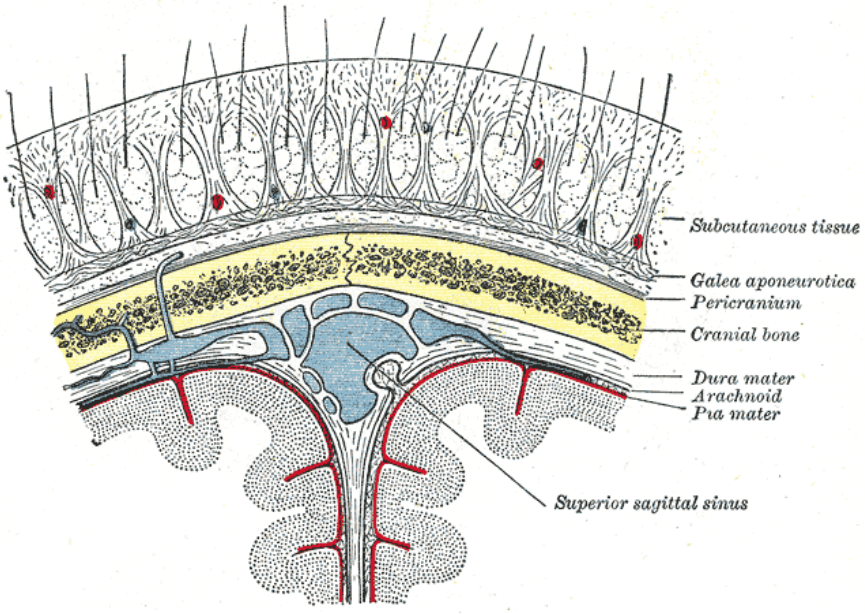

Figure 2-2: Diagram of the Meningeal Layer (Henry Gray, Wikimedia Commons)

The arachnoid mater and pia mater, together called leptomeninges, are connected through web-like arachnoid trabeculae. The acachniod mater contains fibroblasts and collagen and is secured to the dura by CSF pressure and bringing vessels. The pia mater is the thinnest of the meningeal layers and is highly vascularized by a network of small blood vessels. The pia intimately follows all the contours of the brain (Barshes 2005).

The three meningeal layers create three meningeal spaces, the extradural space, the interdural space, and the subarachnoid space. Because the dura is attached to the

cranial bones, the extradural space only exists in pathology when bleeding from ruptured dural vessels pushes the dura away from the cranium. Much like the extradural space, the interdural space does not exist as a natural gap and is only present in the event of subdural bleeding. Finally, the subarachnoid space lies between the arachnoid and pia layers, is on average 1 – 4 mm thick, and is filled with circulating CSF, arachnoid trabeculae, and bridging vessels (Moore 2014). The delicate, fluid rich spaces of the meninges make them highly vulnerable to damage via CSF cavitation.

2.2.3 Brain Regions and Functions

Within the brain, there are six main components, each with their own function (Table 2-4): the cerebellum, medulla oblongata, pons, midbrain, diencephalon, and cerebrum. The cerebrum consists of two hemispheres, each of which can be divided into four separate lobes named after the bones that overlie each region, frontal, parietal, temporal, and occipital (Figure 2-3).

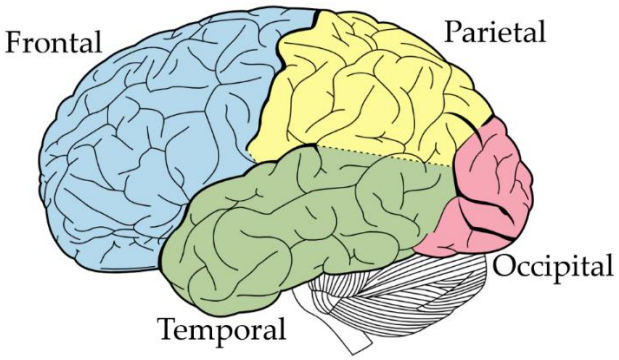

Figure 2-3: Illustration of Brain Lobes (Wikimedia Commons)

While these lobes are primarily divided using landmarks on the brain consistent across anatomical diversity, they do contain local areas of functional importance (Table 2-3). In fact, work in neuroscience continues to update and add to Brodmann's 52 divisions of the human cerebral cortex (Kandel 2013). While breaking these functional areas down in detail is beyond the scope of this work, it is imperative to recognize that localized injury to the brain may cause region specific symptomology. This means that the array of symptomology can provide insights into the regions of damage in the brain, and TBI needs to be considered and discussed as a nuanced localized injury, not just a holistic insult to the neurological system. This concept underlies the revolutionary investigations of Collins *et al.*; by understanding particular symptomology is the result of particular areas of damage, they were able to determine patient specific active treatment plans (Collins 2014). Applying this same conceptual framework and consideration to mechanisms and biomechanics of injury can lead to profound advancements in injury thresholds, injury prevention, and safety device design.

Table 2-3: Functions of the Cortex Lobes (Kandel 2013)

Cortex Lobe	Function
Frontal (including motor cortex)	Short-term memory, planning future actions, movement
Parietal (including somatic sensory cortex)	Somatic sensation, forming body image, relating body in extrapersonal space
Temporal (including deep structures)	Hearing, learning, memory, and emotion
Occipital	Vision

Table 2-4: Gross Brain Regions and Associated Function

Brain region	Function
Medulla Oblangata	Vital autonomic functions (digestion, breathing, heart rate control)
Pons	Conveys motion information from cerebrum to cerebellum
Cerebellum	Modulates force and range of movement, critical in learning of motor skills.
Midbrain	Controls sensory and motor functions including eye movement and coordination of visual and auditory reflexes
Diencephalon	Processes most information being conveyed by CNS to cerebrum and regulates autonomic, endocrine, and visceral functions
Cerebrum (Deep Structures)	Regulating motor performance, memory storage, and autonomic and endocrine responses of emotional states

2.3 Neck Musculature and Head Kinematics

Stronger neck musculature is widely hypothesized as an effective means to reducing the risk of sports related concussion, leading to neck muscle strengthening exercises being a suggested sports related concussion prevention strategy (Viano 2007, Broglio 2009, Collins 2014, Schmidt 2014, Jin 2017). This hypothesis is founded in the idea that neck muscle contraction increases head-to-neck coupling. This increased coupling leads to higher effective mass, especially for anticipated impacts with pre-tensed

musculature, thereby reducing head acceleration and sports related concussion risk (Schmidt 2014).

A number of studies have investigated this hypothesis (Reid 1981, Mansell 2005, Tierney 2005, Viano 2007, Simoneau 2008, Collins 2014, Eckner 2014, Jin 2017, Eckner 2018). Collins *et al*. used a hand held tension scale to obtain neck strength measurements of high school athletes who were monitored for concussion. The study found those who received a concussion had significantly weaker necks than those who did not (Collins 2014). A number of studies took a series of neck strength and anthropometric measurements, then subjected participants to low impulse loads while measuring head and neck kinematics (Reid 1981, Mansell 2005, Tierney 2005, Simoneau 2008, Eckner 2014, Eckner 2018). In each study except Mansell *et al.*, they determined increases in neck muscle force led to decreased head kinematics. Mathematical and computational modeling approaches have also been undertaken to examine the neck strength hypothesis (Viano 2007, Jin 2017). Viano *et al.* utilized a mathematical model and represented the neck as a linear spring with a stiffness determined by neck strength. Jin *et al.* used a finite element approach with the head and neck from the Global Human Body Modeling Consortium (GHBMC). Much like the human participant studies, the two modeling studies also found that neck muscle force influences head kinematics.

Contradicting evidence to this hypothesis is presented in epidemiological studies analyzing the impact of cervical musculature and anticipation on head kinematic response

in football and ice hockey populations. Mihalik *et al.* instrumented youth ice hockey players with the Head Impact Telemetry (HIT) system, and found no statistically significant evidence that impact anticipation affects linear acceleration, rotational acceleration, or Head Impact Telemetry severity profile (HITsp) (Mihalik 2010). For a follow-up study, Mihalik *et al.* looked specifically at the effect of neck strength on head impact biomechanics in youth ice hockey players and found athletes with stronger necks did not experience lower head accelerations (Mihalik 2011). Schmidt *et al.* investigated how cervical muscle characteristics influence head kinematics in a football population using the HIT system. After collecting data throughout an entire season, the study found neither increased neck muscle girth nor neck muscle strength provided a statistically significant decrease in head kinematics (Schmidt 2014). This contradiction in the available evidence and theoretical biomechanics sets the stage for additional work investigating the nuances that lead to the conflicting statements.

2.4 Cavitation

2.4.1 Theory

Cavitation describes the creation and activity of bubbles or 'cavities' within a liquid. The process of cavitation bubble formation, particularly in pure liquids, is best explained using a phase diagram (Figure 2-4). At room temperature and standard pressure water, or CSF, exists as a fluid (Point A, Figure 2-4). To produce a fluid bubble, present tensile forces must be large enough to either rupture the chemical bonds between

molecules, or expand existing nucleation sites in the fluid. Two paths can generate tensile strength that result in bubble formation. The first is by increasing the temperature at a constant pressure, commonly known as boiling (Point B, Figure 2-4). The second is by decreasing the pressure at a constant temperature, commonly known as cavitation (Point C, Figure 2-4). In biological systems, transient negative pressures are more common that rapid heat changes. This work focuses on cavitation in tissue, particularly CSF, because it is anticipated the dilatational tensile stresses from pressure transients are large enough to initiate bubble formation. While fundamental theory around cavitation often considers pure liquids for theoretical simplicity, it is important to note most engineering systems, including the human body, have dissolved gasses in equilibrium (especially nitrogen and argon gas fraction), proteins, and salts that serve as nucleation sites, substantially decreasing the tension required for bubble expansion (Brennen 2014).

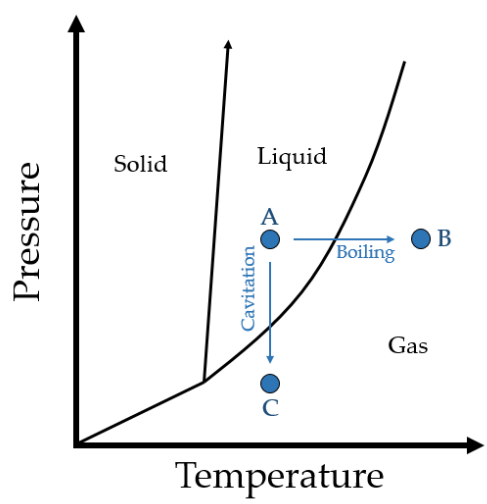

Figure 2-4: Example phase diagram illustrating cavitation and boiling

The mechanism of origin and gaseous contents of a cavitation bubble can dictate the behavior of its growth and collapse. Cavitation can be broken up into four categories based on how they are created (Young 1989). However the category pertinent to this dissertation is acoustic cavitation defined as pressure variations in liquid that reach cavitation thresholds (Young 1989).

Cavitation theory in TBI hypothesizes that pressure variations from impact and skull flexure generate cavitation formation, indicating acoustic cavitation is the primary mode of interest for this work. Regardless of the mechanism of initiation, the Rayleigh-Plesset (RP) equation gives a theoretical basis for the oscillation of an idealized spherical bubble in an incompressible fluid. The dynamics of bubble collapse were first theorized by Rayleigh in 1917 (Rayleigh 1917) and it was not until 1949 that Plesset solved for the addition of oscillation with a bubbles radius whose pressure varies with time (Plesset 1949). The RP equation can be derived using the first principles of mass and momentum conservation and is provided in brief below (Brennen 2014):

This simplified analysis starts with a bubble with radius $R(t)$ (where time is t), that exists in an infinite domain of liquid with temperature and pressure far from the bubble T_∞ and $P_\infty(t)$ respectively. T_∞ is constant with time because temperature fluctuations over the course of cavitation oscillation in the surrounding liquid are insignificant and internal heat sources are not considered. $P_\infty(t)$ is considered to be known and regulates the growth and collapse of the bubble. The surrounding liquid is considered

incompressible making liquid density ρ_L a constant. Liquid viscosity is considered constant and uniform. Finally, the bubble contents are considered homogenous and the bubble temperature $T_b(t)$ and pressure $p_b(t)$ are considered uniform.

$R(t)$ denotes the radius of the bubble, and the radial position in the fluid will be designated as r from the center of the bubble. The radial outward velocity of the bubble wall is designated as $u(r,t)$. The conservation of mass indicates the radial velocity must be proportional to the inverse square of the distance from the center of the bubble:

$$u(r,t) = \frac{F(t)}{r^2} \qquad \text{Equation 2.2}$$

Where $F(t)$ is some function of time. If we consider zero mass transport across the boundary of the bubble, it can be stated that $u(r,t) = \frac{dR}{dt}$ therefore:

$$F(t) = R^2 \frac{dR}{dt} \qquad \text{Equation 2.3}$$

Given a Newtonian liquid such as water or CSF, the Navier-Stokes equation for motion in spherical coordinates in the direction of r can be used:

$$-\frac{1}{\rho_L}\left(\frac{\delta p}{\delta r}\right) = \frac{\delta u}{\delta t} + u\frac{\delta u}{\delta r} - \nu_L\left[\frac{1}{r^2}\frac{\delta}{\delta r}\left(r^2\frac{\delta u}{\delta r}\right) - \frac{2u}{r^2}\right] \qquad \text{Equation 2.4}$$

Substituting u from Equation 2.2 yields:

$$-\frac{1}{\rho_L}\frac{\delta p}{\delta r} = \frac{1}{r^2}\frac{dF}{dt} - \frac{2F^2}{r^5} \qquad \text{Equation 2.5}$$

The viscous condition is eliminated, as the only viscous component is incorporated with the dynamic boundary condition. Equation 2.5 can then be integrated to give:

$$\frac{p - p_\infty}{\rho_L} = \frac{1}{r}\frac{dF}{dt} - \frac{1}{2}\frac{F^2}{r^4} \qquad \text{Equation 2.6}$$

Next the dynamic boundary condition of the bubble surface can be implemented. Let σ_{rr} be the normal stress in the liquid that directs outward radially from the center of the bubble. This makes the net force per unit area acting on this surface $(\sigma_{rr})_{r=R} + p_B - \frac{2S}{R}$ Where S is the surface tension of the bubble. For a fluid with constant density and viscosity, the radial stress is:

$$\sigma_{rr} = -p + 2\nu_L \frac{\delta u}{\delta r} \qquad \text{Equation 2.7}$$

Therefore the force per unit area on the bubble surface is:

$$p_b - (p)_{r=R} - \frac{4\nu_L}{R}\frac{dR}{dt} - \frac{2S}{R} \qquad \text{Equation 2.8}$$

Given the assumption of no mass transport across the boundary of the bubble, Equation 2.8 must be equal to zero. Combining Equation 2.3, Equation 2.6, and Equation 2.8 yields the generalized Rayleigh-Plesset equation.

$$\frac{P_b(t) - P_\infty(t)}{\rho_L} = R\frac{d^2R}{dt^2} + \frac{3}{2}\left(\frac{dR}{dt}\right)^2 + \frac{4\nu_L}{R}\frac{dR}{dt} + \frac{2S}{\rho_L R} \qquad \text{Equation 2.9}$$

$$\boldsymbol{P_B(t) = pressure\ inside\ bubble}$$
$$\boldsymbol{P_\infty(t) = liquid\ pressure\ infinitely\ far\ from\ the\ bubble}$$
$$\boldsymbol{\rho_L = liquid\ density}$$
$$\boldsymbol{R(t) = Bubble\ radius}$$
$$\boldsymbol{\nu_L = Kinematic\ viscosity\ of\ the\ liquid}$$
$$\boldsymbol{S = Bubble\ surface\ tension}$$

Given $P_B(t)$ is known and a variable $P_\infty(t)$ is applied to the system, the RP equation can be solved to determine bubble radius in time $R(t)$. In a biological system, specifically the CSF, cavitation is likely to occur in a boundary restricting space, the

meninges, to experience non-spherical collapse, and to encounter other complexities that violate the RP assumptions. While this makes it difficult to predict CSF cavitation bubble size using the RP equation, the RP equation still provides insight to bubble behavior as the driving pressure $P_\infty(t)$ increases. As this pressure increases the bubble oscillation becomes non-linear and the collapsing wall speed begins to approach the speed of sound of the fluid (Figure 2-5). Eventually this reaches a point where the nonlinearity at bubble collapse generates physical phenomenon that halts the bubbles cyclic nature, resulting in a single phase of growth and collapse. This represents the transition from stable cavitation to transient cavitation.

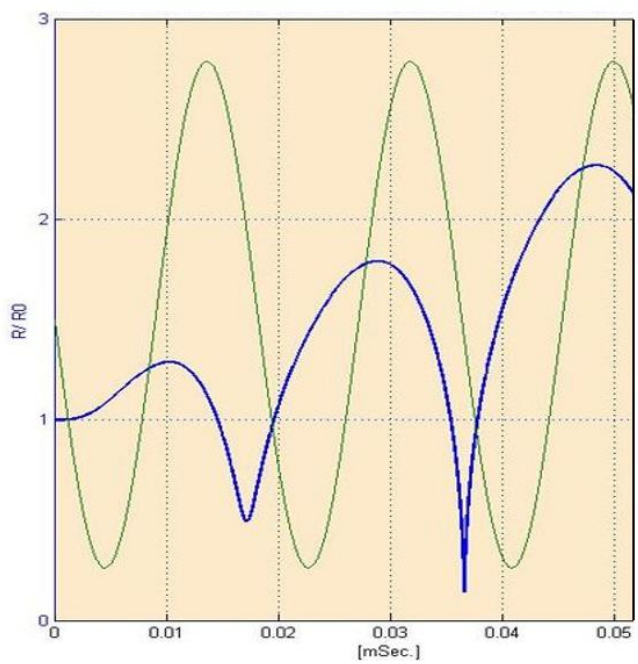

Figure 2-5: Cavitation bubble radius for low (green) and high (blue) driving pressure (Shmuel Ben-Ezra, Wikimedia Commons)

2.4.2 Mechanism of Injury

As outlined in the theoretical analysis above, cavitation appears in two modes, stable and transient. Stable cavitation bubbles non-linearly oscillate around an equilibrium size, and may continue to oscillate for many cycles depending on the driving frequency and pressure. Stable cavitation oscillations utilize a residual compressed gas from a seed bubble that cushions bubble implosion, and results and a relatively controlled event (Young 1989). While stable cavitation may have negative consequences for surrounding tissue due to surface oscillations and microstreaming, its controlled predictable nature makes it ideal for positive medical uses (Tang 2002, Sun 2015, Burgess 2018).

Unlike stable cavitation, transient cavitation occurs over one cycle; bubbles expand, generally creating an evacuated void, and then collapse violently, often creating a mass of smaller bubbles. This collapse generates high pressures and temperatures, resulting in local shockwaves and micro-jets (Figure 2-6). The phenomenon results in destruction such as erosion, emulsification, and molecular degradation (Young 1989). The destructive components from transient cavitation are so violent, they contribute to the degradation of ship propellers and other fast moving metallic components operating in a fluid (Knapp 1955). Given its propensity for damage, it is plausible that if cavitation were to occur within the CSF layer, these shockwaves and micro-jets will displace and damage surrounding tissue.

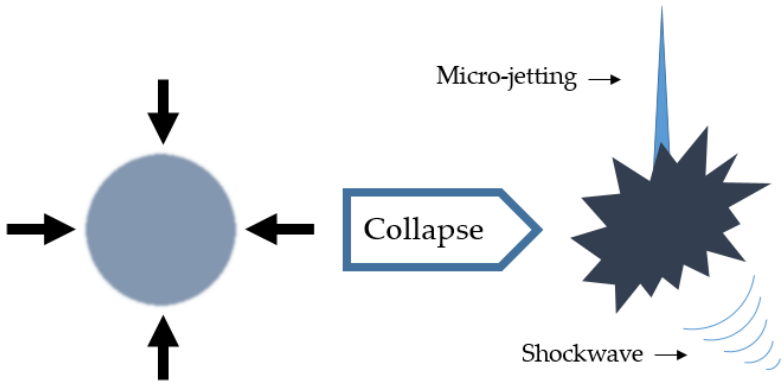

Figure 2-6: Illustration of damaging phenomena upon cavitation collapse

There are multiple mechanistic theories for the generation of negative pressures within the head that may result in acoustic transient cavitation. The first is that linear acceleration caused by a blunt impact creates a pressure gradient along the axis of impact leading to negative pressures on the impact contre-coup (Gross 1958). This theory however ignores the transient aspects and rotational components of a blunt impact, which may influence this pressure gradient (Lubock 1980). Another theory for contre-coup transient cavitation is flexion of the skull which generates a shear wave that travels around the head and creates a localized increase in volume resulting in a localized drop in pressure (Sheldon 1946). This theory has been further shown as a contributing factor to cavitation in blast as increasing the rigidity of a vessel reduced the incidence of cavitation (Yu 2019). Skull flexion also has been postulated as a mechanism for cavitation on the coup, where skull "snap back" after indentation creates negative pressures (Gross 1958).

2.4.3 Cavitation in Soft Tissues

Cavitation as a mechanism of injury has been thoroughly investigated in the field of shockwave lithotripsy. In this process, targeted compressive acoustic shockwaves are used to break down kidney stones so they can be more easily passed through the body. This technique takes advantage of the acoustic impedance mismatch between the kidney stone and surrounding tissue to impart forces that break up the stone. Additionally, this mismatch creates localized negative pressures that may generate transient cavitation bubbles. While the micro jets and additional shockwaves produced by the collapse of these cavitation bubbles aid in the destruction of the kidney stone, the chaotic event is also shown to cause microvascular rupture and kidney soft tissue damage (Carstensen 2000, Zhong 2001, Zhu 2002, Pishchalnikov 2003, Matlaga 2008, Li 2019). Additional work investigated cavitation damage if it occurs within a blood vessel, not just beside it. Again, the products of cavitation collapse in the vessel may cause vessel rupture (Chen 2010).

2.4.4 Cavitation in Head Surrogates

Human head surrogates have been used to investigate cavitation since the inception of study of the injury mechanism in the mid 1900's. Lubock and Goldsmith utilized two different head surrogates, a simple acrylic shell and a back-filled human calvarium, both filled with various CSF simulants (Lubock 1980). While they did observe cavitation during peak tensile stresses of approximately -1330 kPa, it is unclear how CSF permutations affected this threshold. There was no mention of gas pressures or possible

nucleation sites, which may explain why this value is so large. Cavitation was reported to occur in every acrylic cylinder model without further discussion. Additionally, the acrylic skull was thinner with a larger radius than human skulls, limiting the biofidelity of the impact dynamics.

Following the work of Lubbock and Goldsmith, Nusholtz conducted blunt impact cavitation tests using a simple head surrogate made of an aluminum tube and acrylic caps (Nusholtz 1995). The surrogate was instrumented with nine interrelated accelerometers and pressure transducers placed in holes tapped into the surrogate. Pressure acceleration traces were compared to those determined from a finite difference model of the surrogate to investigate effects of cavitation and fluid motion. Results determined that for both the simplified experimental and finite difference models, cavitation is likely to occur during 190 g impacts with violent cavitation collapse occurring at accelerations above 350 g (Nusholtz 1995). While there are biofidelic limitations of the models presented in this work, it is the first visualization of cavitation in a 'head-like' model.

Most recently, Van Orman conducted similar surrogate tests as Nusholtz but with a more complex head surrogate. Van Orman constructed a 3D printed head surrogate derived from MRI scans that had a brain phantom containing gyri and sulci immersed in model CSF (Van Orman 2020). Blunt force trauma with an impact energy of 23.7 J was applied to the head surrogate, and pressure oscillations consistent with cavitation were

observed near the contre-coup location on all impacts. This led to maximal tissue deformation occurring in the sulcal depths during cavitation (Van Orman 2020).

2.4.5 Cavitation in the Brain

Nusholtz *et al.* conducted the first studies investigating the influence of cavitation on the brain using repressurized human cadver heads as well as live rhesus monkeys. Pressure transducers were implanted into the skull on the coup and contre-coup to measure pressure time histories. While these tests did indicate blunt impacts produce a pressure gradient across the brain, they were unable to discern the presence of cavitation. Nusholtz *et al.* were unable to correlate the presence of cavitation to a particular injury (Nusholtz 1984).

Recently, research groups have investigated the influence of cavitation on brain tissue *ex-vivo*. Canchi *et al*. tested blast induced cavitation on a live rat hippocampal brain slice submerged in artificial CSF. A split Hopkinson bar generated a shock wave in the artificial CSF chamber containing the brain slice placed on top a small seed bubble. These tests were able to directly measure high tissue strains created by cavitation collapse and micro-jetting. Canchi *et al*. produced data supporting the probability that transient cavitation events could directly result in structural brain injury (Canchi 2017). Dougan *et al.* used needle induced cavitation (NIC) to generate cavitation within brain tissue to observe high strain rate deformation upon collapse. This work was able to identify an

injury pattern for tissue damaged by NIC and observed how varying viscoelastic properties in the brain influenced the mechanics of cavitation collapse (Dougan 2020).

Work recently conducted by Wrede uses a syringe apparatus to push air through capillary tubing to induce microbubbles (Wrede 2019). The work conducted two key experiments, the first induced microbubbles near soft polymers and used confocal microscopy and interferometry to determine visual damage of the soft polymer surface. The second study induced microbubbles in cultured astrocytes and observed distinct morphological and genetic changes in the cells following exposure to cavitation (Wrede 2019). Results of this work further indicate that if cavitation does occur within the cranial cavity, it has potential to both damage neurological tissue and disrupt the role of astrocytes in brain homeostasis.

Due to the increased prevalence of blast neurotrauma in military and civilian arenas, a number of studies examined the role cavitation might play in this mode of injury (Moore 2008, Goeller 2012, Panzer 2012, Salzar 2017). These studies contain both experimental and modeling components but, much like blunt impact cavitation studies, they do not arrive at a consistent observation. This is the result of experimental and modelling design and a variety of assumptions in the pressure threshold for cavitation formation (Moore 2008, Goeller 2012, Panzer 2012, Salzar 2017), a value that is not experimentally agreed upon (Herbert 2006, Takhounts 2008, Singh 2015, Salzar 2017).

2.4.6 Outstanding Issues in Cavitation Literature

The skull provides a barrier to many of the current imaging technologies, limiting the tools that can be used to observe cavitation within the skull. Previous work discussed had tools limited to high speed imaging using a clear surrogate, pressure transducers placed within a cadaveric skull, pressure thresholding in finite element models, and even acoustic detection (Lubock 1980, Nusholtz 1984, Nusholtz 1995, Nusholtz 1995, Nusholtz 1997, Panzer 2012, Salzar 2017, Li 2019). However, these present limitations that diminish effectiveness for observing cavitation formation. Studies using high speed optical imaging require the use of a translucent container. This limits the studies to artificial, often acrylic skulls which lack viscoelastic biofidelity and boundary conditions present in the live skull-CSF-meningeal interface. Studies that used pressure transducers were able to increase biofidelity through the use of cadaveric skulls and live monkey models, but these often consisted of a compromised cranial cavity. The skulls needed to be back filled through the foramen, and holes were drilled in the skull to implant pressure transducers. Furthermore, pressure transducers were only able to detect pressure changes in their immediate vicinity. Pressure thresholding in finite element models is subjected to all the general limitations in finite element models previously discussed, with the addition that their success hinges on the pressure threshold for cavitation formation within the CSF (Moore 2008, Goeller 2012, Panzer 2012, Salzar 2017), a value that has not been experimentally agreed upon (Herbert 2006, Takhounts 2008, Singh 2015, Salzar 2017).

2.5 Acoustic Emissions

2.5.1 Theory

A bubble that is set into either stable or transient motion by an acoustic source will generate spherical pressure waves making it a localized source of sound. These waves can be detected using microphone technology, and the behavior of the acoustic emission is strongly dependent on the cavitation type and driving intensity. Driving intensity is the primary determinant for acoustic emissions of stable cavitation bubbles. For low levels where bubble oscillation remains linear, the acoustic signal will only consist of the fundamental driving frequency. However, as the driving intensity increases and bubble oscillation turns non-linear, harmonics of the driving frequency appear on the acoustic spectrum. The second harmonic is the most prominent, and half-order harmonics with a low level of white noise begin to appear as well (Young 1989). Nevertheless, the acoustic emissions of stable cavitation oscillation are not relevant for two reasons: first, stable cavitation causes limited byproducts (shockwaves and micro-jetting) believed to contribute to tissue damage. Second, cavitation formation in blast is the result of similar mechanisms hypothesized for blunt impact. Previous work indicates only transient cavitation occurs under blast loading in surrogate and live animal models (Yu 2019).

The acoustic emission spectrum dramatically changes when cavitation transitions to the transient regime. Of note, there is a drastic increase in the intensity of subharmonics and white noise. While in theory, it is possible to predict the frequency content of an

acoustic emission from transient cavitation collapse (Young 1989, Brennen 2014), the phenomenon surrounding the chaotic event render this experimentally impractical. As previously discussed, a blunt impact to the head is a complicated interaction influenced by anatomical geometry, heterogeneous materials, and the impact itself. Because of this, the driving frequency is not only difficult to predict but will most likely be composed of different frequency components resulting in a range of harmonics (Young 1989). Furthermore, the collapse of a transient cavitation bubble produces shockwaves and microjetting. These will generate an essentially infinite series of harmonics for an indeterminate number of driving frequencies (Young 1989). The chaotic nature of transient cavitation collapse in theory will have particular discernable frequency components, but in practice will appear as a wideband acoustic response, refereed by the transmission medium, conditions, and measurement devices used.

The tissue properties of the skull affect acoustic emission detection. Viscoelastic damping during transmission across the dura, acoustic impedance across the skull, and acoustic attenuation in both the dura and the skull have been shown to drastically attenuate frequencies relevant to this study (McElhaney 1970, White 1978). Studies using acoustic emissions to detect cavitation in soft tissue rely on acoustic information in the 1-3 MHz range. This acoustic range presents a problem for detection through the skull, both the power of acoustic signal from transient cavitation collapse and transmissibility

through the skull decrease with increasing frequency ranges (McElhaney 1970, White 1978, Young 1989).

2.5.2 Wavelet Transform

Due to the acoustic impedance mismatch and the viscoelastic properties of the skull and surrounding tissues, high frequency (>250 kHz) acoustic waves can be attenuated 10-30 dB, making them difficult to differentiate from noise through the skull (Fry 1978, Eckersley 2020). Lower frequencies emitted by cavitation collapse, while able to pass through the skull with less damping, can be muddied by other events surrounding the impact. Because of this, the signal needs to be decomposed appropriately in both time and frequency space.

One form of decomposing an acoustic signal into time and frequency space simultaneously is through a windowed Fourier transform (WFT). The 'window' of a WFT influences the function's results as it imposes a scale or response interval to the analysis and is often selected using an arbitrary function. This scale also makes the method inaccurate and inefficient for time-frequency localization because of aliasing of high/low frequency components that fall outside of the window and repetitive analysis to determine the optimal 'window' (Torrence 1998). For analysis where there are a wide range of dominant frequencies that make determining a predetermined scale difficult, such as detection of acoustic emissions from cavitation collapse, wavelet analysis should be used, as it is scale independent (Torrence 1998).

The continuous wavelet transform (CWT) is a technique for analyzing acoustic data in time and frequency space simultaneously independent of scale. The CWT analysis used in this work follows the techniques and equations provided by Torrence and Compo described in brief here. A CWT can be used to analyze both a continuous or discrete time signal. Equation 2.10 describes the CWT convolution for continuous acoustic signals:

$$X_W(a,b) = \frac{1}{|a|^{\frac{1}{2}}} \int_{-\infty}^{\infty} x(t)\overline{\psi}\left(t - \frac{b}{a}\right) dt \qquad \text{Equation 2.10}$$

Where $x(t)$ is the acoustic signal continuous in time, $\overline{\psi}$ is the wavelet basis function, or 'mother wavelet', a is the scale ($a > 0$) of the mother wavelet, and b is the translational time value. By altering a the CWT is able to convolve 'daughter wavelets' that are a compression (higher frequency) or dilation (lower frequency) of the mother wavelet, extracting frequency content of the acoustic signal. Changing b translates the wavelet through the acoustic signal, providing the temporal component of the analysis. Equation 2.11 allows the same process with a discrete time signal:

$$W_n(s) = \sum_{n'=0}^{N-1} x_{n'} \psi^* \left[\frac{(n' - n)\delta t}{s}\right] \qquad \text{Equation 2.11}$$

$$* \; indicates\ complex\ conjugate$$

Both equations provide a result that constructs a two dimensional image of the acoustic signal displaying power of frequency components as they vary in time.

The CWT relies on a mother wavelet that must have zero mean and be localized in both time and frequency space (Torrence 1998). For the analysis in this work, the Morlet

wavelet (Figure 2-7) is used as the mother wavelet. The Morlet wavelet (Equation 2.12 and Equation 2.13) is a complex function with real and imaginary components; therefore, the convolution returns information on both amplitude and phase, which gives the CWT the optimal balance in time and frequency space resolution for localizing unknown frequency content in acoustic signals. Furthermore, the Morlet wavelet bears similar characteristics to an acoustic emission signal, increasing the overall power returned for each daughter wavelet. The Morlet wavelet in the time domain can be described as:

$$\psi_0(\eta) = \pi^{-\frac{1}{4}} e^{i\omega_0\eta} e^{-\frac{\eta^2}{2}} \qquad \text{Equation 2.12}$$

$$\boldsymbol{\eta}: \boldsymbol{nondimensional\ time\ parameter}$$
$$\boldsymbol{\omega_0}: \boldsymbol{nondimensional\ frequency\ for\ admissbility}$$

The Morlet wavelet in the frequency domain can be described as:

$$\widehat{\psi_0}(s\omega) = \pi^{-\frac{1}{4}} H(\omega) e^{-\frac{(s\omega-\omega_0)^2}{2}} \qquad \text{Equation 2.13}$$

$$\boldsymbol{H(\omega)}: \boldsymbol{Heaviside\ Step\ Function}$$

To prevent lower frequency content from dominating the wavelet plot and to directly compare to transformations of other signals, the wavelet function at each frequency scale needs to be normalized to a unit energy value (Torrence 1998).

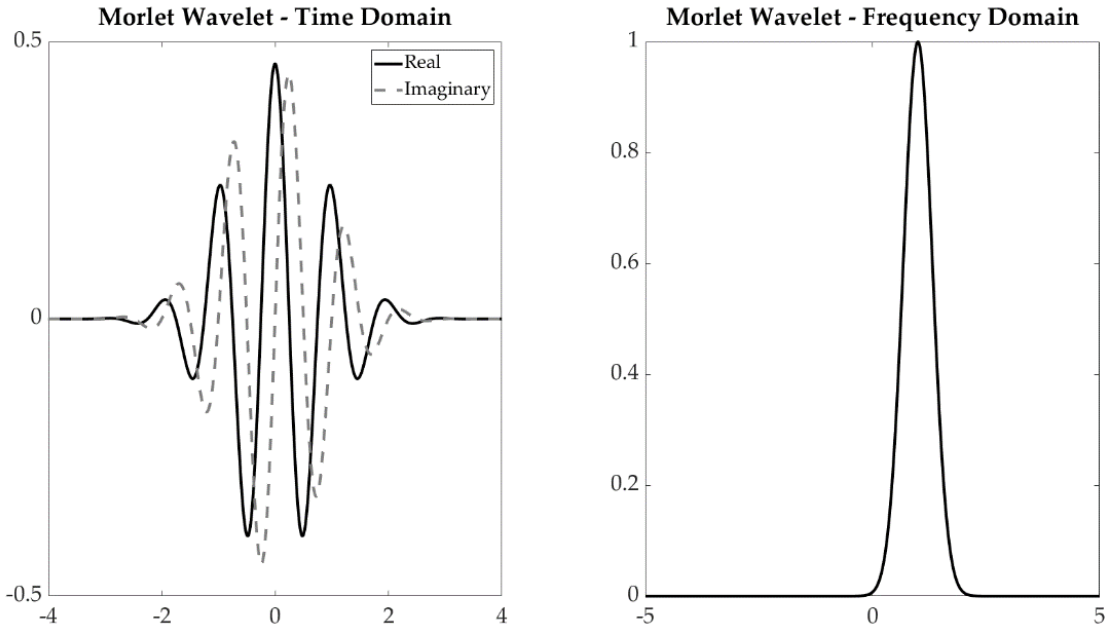

Figure 2-7: Representative plots of the Morlet wavelet in time and frequency domains

3. Role of Neck Musculature in Head Kinematics

To understand the role of cavitation in blunt TBI, it is imperative to have a foundational knowledge of impact biomechanics and the factors that influence head kinematics. However, there are competing hypothesis for fundamental components of head impact biomechanics. One of these is the role of neck musculature in head kinematics, particularly the strategy of increasing neck strength to prevent head injury. This study contributes to the literature through a finite element modeling study investigating the influence of neck musculature on head kinematics in both realistic and extreme neck muscle activation cases in a range of impact scenarios.

3.1 Objectives

The hypothesized method of action for head protection through neck musculature involves recruitment of torso mass through the neck during the impact, substantially decreasing the head acceleration. However, two lines of biomechanical evidence suggest that neck musculature has limited effect on short term blunt impact kinematics: low short-term inertial head-to-neck coupling, and low moment of cervical muscle resistance compared to the impact moment. Previous work emphasizes loose head/neck coupling in compressive impact loading due to a low neutral zone spine stiffness (Nightingale 1996). While pure spinal compression is not a common athletic loading scenario, Liu *et al.* finds that a 0.5 Nm moment results in 12 degrees of combined flexion and extension at the O-C1 joint (Liu 1982). Physiologically appropriate muscle response of humans works in

tandem with low structural stiffness to reduce overall coupling of the head and torso through the neck. Vasavada *et al.* determined maximum voluntary cervical muscle contraction force generates a moment of 30±5 Nm in near 50th percentile adult males (Vasavada 2001). For comparison, an impact involving a 40 g linear head acceleration using a head mass of 5 kg and a neck length of 0.175 m results in a moment of 315 Nm. For a 40 g blunt impact, increasing cervical muscle force two standard deviations above the mean provides only a 3% increase in resistance.

The apparent contradiction between theoretical biomechanics and certain experimental results reported in literature provides the primary motivation for this study. A second motivation stems from the relative difficulty of studying head and neck kinematics with injury risk in human participants and difficulty simulating human muscle response in cadaveric. In lieu of using human participants or cadavers, investigators often use a mechanical surrogate - either a Hybrid III (HIII) neck attached to a dummy head or a freely dropped dummy head form (free-head) - when conducting drop or impact tests (Viano 2007, Beckwith 2012). An important and substantial limitation of this approach is that the HIII neck is qualitatively stiffer than a human neck with musculature, especially in the unloaded/nominal position. This results in an unrealistic highly coupled head-to-neck complex when compared with humans, particularly in loading scenarios other than those similar to a frontal impact vehicle crash (Dibb 2006).

The goal of this study was twofold. First, investigate the effect of cervical muscle force on head kinematics following blunt impact in the time period at and immediately following the impact - denoted as "short term" (<50 ms). Second, determine the biofidelity of blunt impact head kinematics of a HIII neck and head surrogate, and a free-head surrogate when compared to a validated computational model of the human head and neck. The study examines three athletic scenarios: an impact from a high speed object such as a baseball in flight, an 80 g helmeted head impact, and a 40 g helmeted head impact. The latter are representative of helmeted sports scenarios. For this study, an anatomically and inertially accurate and validated 50th percentile human head-neck computational model was used to simulate the response of an adult human head and neck to blunt impacts. The model output provides detailed kinematic analysis of simulated on-field impacts; controlling for impact position, timing, and cervical muscle response (Dibb 2013, Dibb 2014). Six neck conditions were tested, and four metrics relevant to cavitation were used to assess the resulting kinematics of these impacts under varying neck conditions. There were two hypotheses evaluated in this study. First, increased mass and moment of resistance provided by increased cervical muscle force generating capacity will not alter short term (<50 ms) head kinematics enough to reduce cavitation risk for any impact scenario tested. Second, the testing condition of a free-head (no neck) will be more biofidelic for head impacts than a HIII dummy neck compared to a relaxed human neck condition.

3.2 Methods

Model simulation was performed with LS-DYNA (V810 double precision, Livermore Software Technology Corporation, Livermore CA) using two previously validated neck models. The first was the neck from the Duke University Head Neck Model (DUHNM) developed by the Duke Injury Biomechanics Laboratory consisting of an osteoligamentous cervical spine, and 23 active muscle pairs (Chancey 2007, Dibb 2013, Dibb 2014). The second model represents the HIII neck and was developed by the National Crash Analysis Center (NCAC) at The George Washington University and is distributed by LSTC (Mohan 2009). Both necks were positioned between finite element models of the HIII head and torso developed by NCAC and distributed by LSTC (Mohan 2009). All contacts and constraints present in the LSTC distributed HIII model remained intact for the HIII neck simulations.

Blunt impacts to the two head-neck models were simulated using three separate linear elastic, spherical impactors depending on the specific impact condition. Their properties are summarized in Table 3-1. Impactor 1 is modeled on major league baseball stiffness (Hendee 1998). Both Impactors 2 and 3 were designed to represent helmeted impacts of varying severity and were developed based on human cadaver head experimental drop data conducted in the Duke University Injury Biomechanics Lab. The cadaveric head was instrumented with a six degree of freedom sensor package mounted to the skull posterior to the foramen magnum and fitted with a Riddell Speed football

helmet. It was dropped twice from 60 cm impacting the front of the helmet to simulate a moderate impact. Simulated impacts using LS-DYNA were completed for Impactors 2 and 3 where the impactor struck an unconstrained HIII head (NCAC) with the impact velocity determined for the experimental head drops. The elasticities of the impactors were modulated within the computational modeling environment to achieve the desired resultant linear acceleration trace compared to the averaged experimental head drop data. Impactors 2 and 3 have similar peak acceleration, but Impactor 2 has a 5 ms shorter duration than a representative moderate helmeted impact, while Impactor 3 has a 10 ms longer duration than Impactor 2.

Table 3-1: Specifications of Head Impactors

Impactor	Mass (kg)	Diameter (mm)	Young's Modulus (MPa)
Impactor 1	0.192	73	55.4
Impactor 2	5.507	73	9.4
Impactor 3	5.507	150	1

Using the three impactors, four impact scenarios were created; the impactors and respective initial velocities used are summarized in Table 3-2. The first simulates a baseball impacting a bare head while the second and third simulate 80 g helmet to helmet collisions with shorter and longer durations respectively. The fourth scenario modeled a 40 g helmet to helmet impact. The values of 40 g and 80 g were selected to be within the ranges presented as mild and moderate impacts by Schmidt *et al*. (Schmidt 2014).

Table 3-2: Impactors and Initial Velocities for Impact Scenarios

Impact Scenarios	Impactor	Initial Velocity (m/s)	Energy (J)
Scenario 1	Impactor 1	30	58
Scenario 2	Impactor 2	5	69
Scenario 3	Impactor 3	8	176
Scenario 4	Impactor 2	3	25

For each impact scenario, six neck conditions were analyzed. The first two are relaxed and tensed musculature scenarios (Dibb 2013). In the relaxed condition, muscles were activated the minimum amount necessary to maintain head stability prior to impact (Dibb 2013). For the tensed condition, muscles were activated to the maximum amount possible while maintaining head stability prior to impact (Dibb 2013). The next two conditions model states of fully activating flexor muscles, and fully activating extensor muscles. These conditions represent bounds of muscle activation that are likely unachievable in a living human while being theoretically possible. The final two conditions model common experimental setups of a free-head and a HIII neck. In the free-head condition, impactors contact an unconstrained HIII head. In the HIII neck condition, the HIII model is placed in-between the head and torso instead of the DUHNM. The three neck types (DUHNM, HIII, and free-head) are illustrated in Figure 3-1.

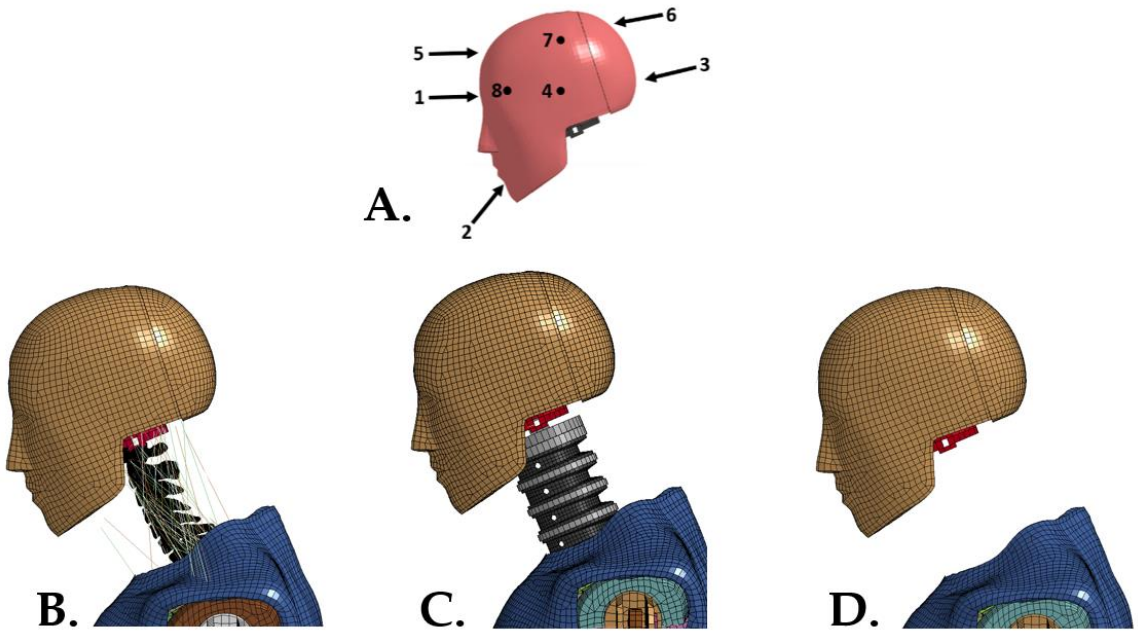

Figure 3-1: (a) Sagittal view of the impact locations tested. Impacts 1 – 4 are directed towards the center of gravity of the head. Impacts 1, 2, 3, 5, and 6 impact along the mid-sagittal plane while impacts 4, 7, and 8 impact perpendicular to the sagittal plane. (b) Sagittal view of the model that implements the Duke University Head Neck Model between a Hybrid III head and torso. (c) Sagittal view of the model that implements the Hybrid III neck between a Hybrid III head and torso. (d) Sagittal view of the free-head condition where the Hybrid III head remains unconstrained.

For each of the four impact scenarios and six neck conditions, eight different locations on the head were impacted as illustrated in Figure 3-1. Kinematic data was sampled every 0.05 milliseconds and simulations were run for 40 ms to ensure linear and angular accelerations reach their peaks and return to zero. The data were filtered at 1650 Hz using a 20th order Butterworth filter that provided a sharp cutoff frequency while remaining stable.

To compare the kinematic responses from each simulation, Peak Resultant Linear Acceleration, Peak Resultant Angular Acceleration, Head Injury Criterion (HIC), and Head Impact Power (HIP) were used. Peak resultant linear acceleration is a historically common metric to analyze head injury severity and describe linear acceleration exposure (Viano 2007, Broglio 2009, Mihalik 2010, Schmidt 2014). Brain strain has been shown to be caused by angular accelerations; to represent angular kinematics peak resultant angular acceleration was selected (Cullen 2016). HIC is a useful metric because it incorporates both impact duration and linear acceleration magnitude. HIP includes weighted linear and angular kinematics based on the geometry of the head (Newman 2000). To determine significance between the results of the different neck conditions, the range of values for all neck conditions in each impact scenario and location were compared to critical effect sizes for each injury metric. These were determined from literature and defined as the difference between mild and severe injury thresholds (Eiband 1959, Margulies 1992, Mertz 1996, Marjoux 2008).

3.3 Results

One hundred and ninety two simulations were completed spanning the experimental test conditions. Figure 3-2 plots kinematic results for the various neck activation conditions and impact locations for peak resultant linear acceleration and peak resultant angular acceleration separated by impact scenario. HIC and HIP are not

depicted because they follow similar patterns as the peak resultant linear acceleration results.

None of the maximum differences between the four neck activation conditions for a given impact scenario and location exceeded the critical effect size based on injury reference values. The extensor neck condition exhibited the lowest linear acceleration dominated metrics (peak resultant linear acceleration, HIC, and HIP) for 57% of impacts while the relaxed neck condition showed the highest linear acceleration dominated metrics for 80% of impacts (Figure 3-2). The relaxed neck condition showed lowest peak resultant angular acceleration values for 65% of impacts while the extensor neck condition showed highest peak resultant angular acceleration values for 56% of impacts. Impact location 2 shows a different trend compared to the global peak resultant angular acceleration results, as the relaxed neck condition shows the highest values while the tensed neck conditions produce lower values. The influence of impact location and scenario on linear and rotational injury metrics can be an order of magnitude larger than changes in muscle activation alone (Figure 3-2).

Impact location variations for peak resultant linear acceleration values (Figure 3-2) displayed no consistent pattern. For peak resultant angular acceleration, location 7 consistently produced the highest values while locations 1 and 3 consistently had the lowest values as confirmed by the averages of all impacts for a given location.

Neck activation conditions for peak resultant linear acceleration and peak resultant angular acceleration were plotted by impact scenario to determine the biofidelity of simulated experimental blunt impact head kinematics (Figure 3-3). The relaxed neck condition served as representative of a biofidelic 50th percentile male human head-neck response. As in Figure 3-2, HIC and HIP are not included because they trended similar to peak resultant linear acceleration. The HIII neck was 6±1% (mean±SE) lower than the relaxed condition for linear acceleration dominated metrics while the free-head condition were 12±2% higher. For peak resultant angular acceleration, the HIII neck was 12±4% higher than the relaxed neck condition while the free-head was 2±3% lower.

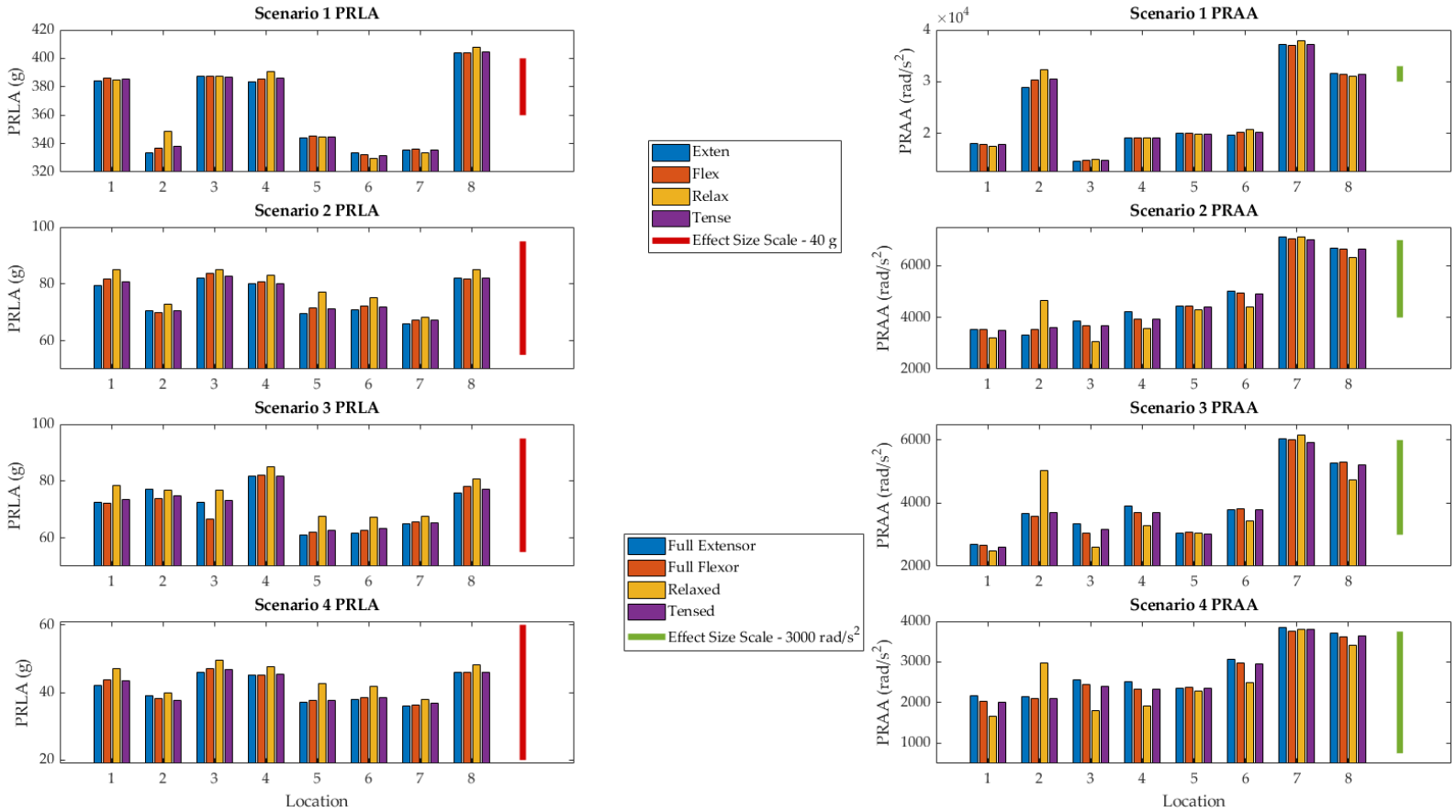

Figure 3-2: Peak resultant linear acceleration and peak resultant angular acceleration injury metrics for different neck activation states separated by location and impact scenario. Compared to the effect size color bar and differences in location and scenario, neck condition has little influence on metrics.

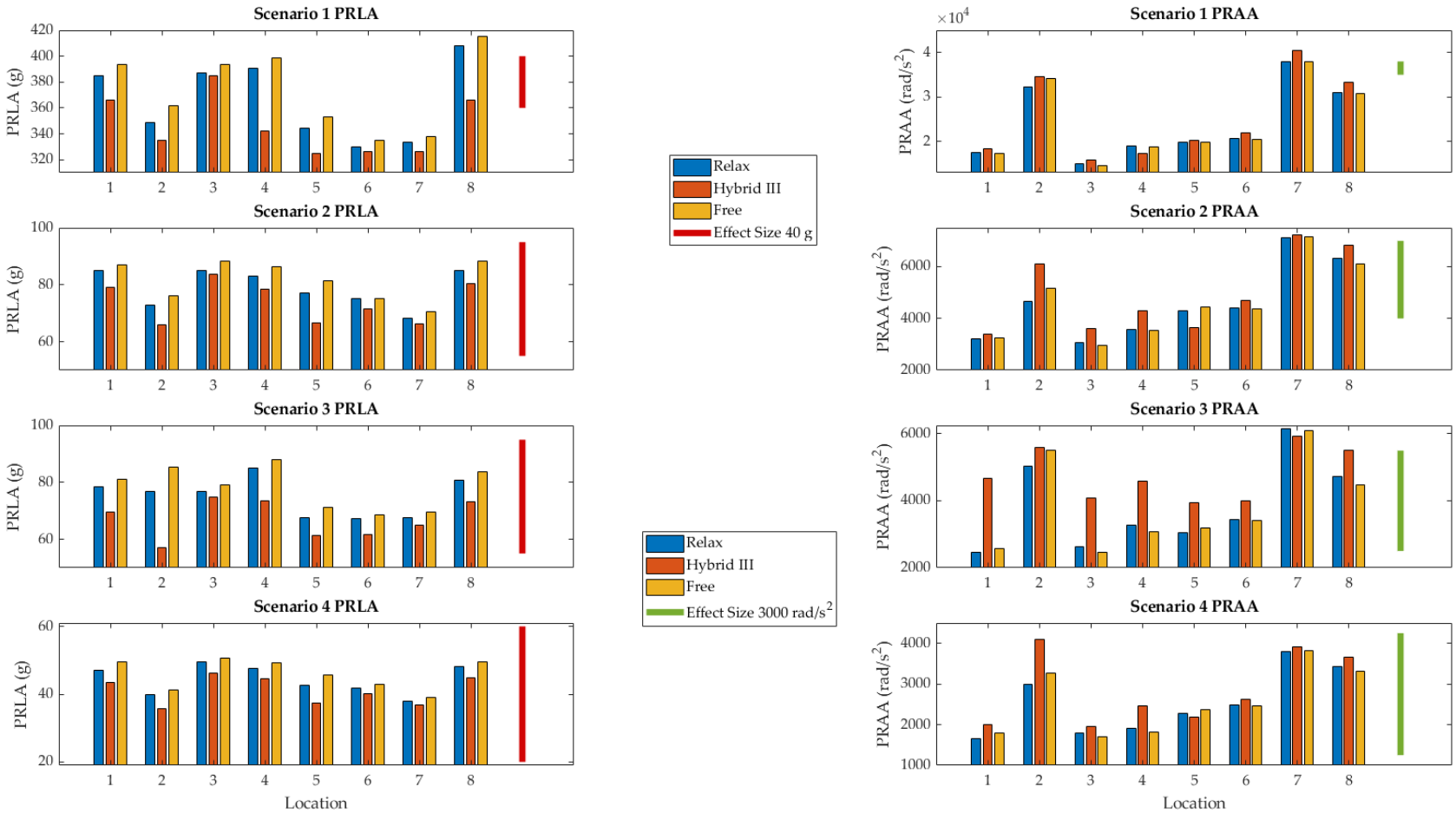

Figure 3-3: Peak resultant linear acceleration and peak resultant angular acceleration injury metrics for different neck experimental testing conditions separated by location and impact scenario. The influence of experimental neck condition on head kinematics depends on the metric used.

3.4 Discussion

No appreciable improvement in four common cavitation short term injury metrics were found due to increases in cervical muscle generated force. Impact distance from the head center of gravity and magnitude have a larger influence on short term head kinematics than increasing cervical muscle force. This is consistent with Schmidt *et al*. where stronger neck muscles in a college football population did not reduce head accelerations (Schmidt 2014).

Peak resultant angular acceleration, in contrast with linear acceleration metrics, shows tensed activation states result in higher values than relaxed activation states. This is due to small effective mass increase. Additional mass is recruited below the head-neck center of rotation, lowering the center of rotation relative to the initial free mass. Since a majority of impacts are located above the center of rotation, lowering the center of rotation increases the moment arm of the impacts, increasing peak resultant angular acceleration values. This is supported by the relaxed muscle condition having consistently higher peak resultant angular acceleration values than the tensed muscle conditions at location 2, the one location below the center of rotation. This result shows cervical musculature influences head kinematics differently depending on the metric analyzed. Therefore, based on the current understanding and injury metrics for cavitation, no consistent effect can be seen by changing neck muscle force.

These results contradict previous literature because a number of limitations prevent the prior studies from accurately capturing the poor head-to-neck coupling in humans (Reid 1981, Tierney 2005, Viano 2007, Simoneau 2008, Collins 2014, Eckner 2014, Jin 2017, Eckner 2018). Collins *et al.* only examined whether an athlete received an injury (Collins 2014). Confounding variables such as anthropometric size by position, previous head injury, or personality traits, may also lead to injury. Several studies used human participants who, in a laboratory setting, can only be exposed to non-injurious events with low peak accelerations and long durations (Reid 1981, Mansell 2005, Tierney 2005, Simoneau 2008, Eckner 2014, Eckner 2018). These long duration events maximize head/neck coupling and provide a poor surrogate for on field blunt impacts. Also, these studies examine changes in velocity and neck stiffness over large head excursions and durations. Because of this, these studies fail to capture the influence of neck musculature over the short distance and duration where TBI is believed to occur (Marjoux 2008). Finally, Viano *et al.*, and Jin *et al.* utilized a linear spring mathematical model and GHBMC model that oversimplified cervical spine biomechanics and muscle activation schemes (Viano 2007, Jin 2017). Due to the complex vertebral body and musculature interactions, the cervical spine does not act as a linear spring, and the muscle activation scheme presented in Jin *et al.* would result in overly tense muscles and an unstable head positioning (Jin 2017).

The flexor and extensor full activation states are two extremes. They are unrealistic representations of an impact event, as they would generate a counterproductive head position prior to the impact. However, testing these activation schemes illustrates in even the extreme scenarios, cervical muscle activation does not improve short-term injury metrics.

Results from the second portion of this study indicate performance of common experimental neck conditions compared to a relaxed neck condition depend on the injury metric used. For linear acceleration injury metrics, HIII neck values were lower than the relaxed neck condition values while free-head values were higher than the relaxed neck condition values. This is expected because a stiff HIII neck provides more linear resistance than a free-head with no neck (Dibb 2006). For peak resultant angular acceleration, the free-head condition values were lower than the relaxed condition while the HIII values were higher. This may be because the neck provides a tether, translating linear kinetic energy to rotational kinetic energy. With peak resultant angular acceleration, free-head values are closer to relaxed condition values, supporting the hypothesis. The results suggest selecting the experimental neck condition depending on the metric of interest. However, for all neck conditions and injury metrics, except peak resultant angular acceleration with free-head, there is significant deviation from a relaxed neck condition that must be considered when reporting values.

This study has some limitations. First, impactors were modeled with linear elastic material for a nonlinear elastic scenario. However, we hypothesize nonlinear impactors would provide comparable results because of small impactor deformation. Also, DUHNM validation has only been conducted in the mid-sagittal plane. However, because this study compares results across the same model, conclusions should not change. Due to a lack of statistical variation in the modeling environment, only an effect size comparison could be conducted. Finally, while impactors 2 and 3 successfully mimicked the experimental head drop data, those experiments have limitations compared to on-field impacts. The drop test impact surface was a rubber covered rigid plate as opposed to a helmeted head, shortening impact duration. Accelerometers for the experimental drop tests were positioned near the center of gravity while model accelerations were determined at the head's exact center of gravity.

3.5 Conclusions

Current results using a validated biofidelic head-neck model suggest increased cervical muscle force does not influence short term (<50 ms) head kinematics in four athletically relevant scenarios. Without a strong influence on head kinematics, neck muscle strengthening cannot strongly influence response to potentially injurious impacts, countering assertions that strengthening the cervical musculature can lower an athlete's cavitation risk. Increasing cervical muscle strength and activation may have different effects depending on the metric used to quantify injury risk, but ultimately impact

location and impact magnitude influence short-term head kinematics more than the force generating capacity of the cervical musculature. Finally, biofidelic limitations of both Hybrid III and free head experimental conditions must be recognized when reporting results. Indeed, the use of the Hybrid III dummy is not recommended to assess the effect of musculature on human injurious impacts owing to the non-biofidelic strong coupling of the HIII neck to the torso.

Since this work was published in 2018, further contributions have been made to the injury biomechanics literature about the role of neck musculature in head kinematics (Bruneau 2019, Reynier 2020). Bruneau determined changes in muscle activation do not influence the maximum principle brain strain from a blunt impact using a finite element head and neck model (Bruneau 2019). Using volunteer low level impact data, Reynier *et al.* found activated cervical musculature can influence head kinematics, but mention it is unknown how these results translate to higher cavitation inducing blunt impacts (Reynier 2020). This literature provides additional insight to the limited role cervical muscle activation plays in cavitation prevention.

4. Development of an Acoustic Biomarker for Blunt Impact CSF Cavitation

4.1 Objectives

The primary investigation of this dissertation requires detection of cavitation within the cranial cavity of a pig model. Traditional imaging methods are unable to detect intracranial CSF cavitation in-vivo primarily due to the opaque barrier the skull provides (Bennett 2009, Hamhaber 2010, Johnson 2013, Espindola 2017). The collapse of a transient cavitation bubble is a violent phenomenon that can produce damaging shockwaves, microjets, and other cavitation events. Because of this, cavitation collapse emits a wideband acoustic signature (Ilyichev 1989, Young 1989). It is hypothesized that the presence of this signature can be detected through the skull, and by localizing the signal in both time and frequency space, the acoustic emission can be used as a cavitation biomarker differentiable from the noise of blunt impact. To investigate this, controlled laser induced cavitation tests were used to assess the presence of wideband acoustic output upon cavitation collapse. In concert, a clear surrogate head model was used to visualize response to blunt impact cavitation and assess whether acoustic emissions upon collapse can be differentiated both in frequency and time from blunt impact noise.

4.2 Methods

The methodology of this study was divided into two test series. First, a water tank laser-induced cavitation study to confirm the wideband acoustic emission of transient cavitation collapse without the confounding noise of a blunt impact. Second, a clear

acrylic head surrogate impact test was used to visualize blunt impact cavitation and show acoustic emissions upon collapse can be differentiated from blunt impact noise. Acoustic data for all tests were collected using a PicoScope 5444B (Pico Technologies, UK) at 31 MHz sample frequency, band pass filtered from 20,000 to 1,000,000 Hz using an 8 pole phaseless Butterworth filter (preliminary work determined signal outside of this band is indistinguishable from noise), and analyzed in Matlab R2020A (MathWorks, US). Wavelet transforms were conducted using a Morlet wavelet, shown in Figure 2-7. This wavelet was selected for two principle reasons: its generic similarity to an acoustic emission trace based on rapid onset and approximately exponential falloff, and its consistent resolution in the time and frequency space. Tests utilizing acoustic analysis underwent a similar process outlined in Torrence 1998 (Torrence 1998). To prevent lower frequency information from dominating the wavelet plot (Torrence 1998) each frequency band is normalized by its maximum value so that the peak signal in all wavelet plots is 1. The noise in the acoustic signal prior to impact is approximately Weibull (Figure 4-1), but was characterized with a mean and standard deviation, true signal is considered to be five standard deviations above the mean noise. Wavelet plots presented below only display this threshold signal.

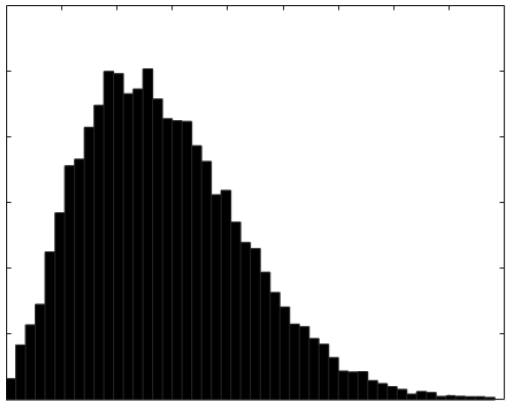

Figure 4-1: Distribution of the acoustic noise prior to blunt impact.

4.2.1 Laser Induced Cavitation Tests

A series of controlled laser-induced cavitation bubble tests were conducted to determine the acoustic signature of bubble collapse without the confounding noise of a blunt impact. This technique eliminates the influence of remnant wall nucleation sites in containers on cavitation. An open-air glass tank (Figure 4-2) was filled with de-ionised water. Water was used instead of a more complex surrogate because the dynamics and acoustic response of cavitation is dominated by the bulk modulus of the medium containing the cavitation bubble. Laser pulses (532 nm up to 20 mJ of power) were focused to a consistent location in the glass tank at levels known to generate cavitation bubbles (Li 2019). The power of the laser was modulated to vary bubble size between 1.5 mm and 2.8 mm, selected as realistic sizes for meningeal bubble formation (Barshes 2005). Acoustic data of initiation and collapse were captured using two types of sensor. High-frequency information (100–500 kHz bandpass filter) was collected at 18 MHz using three Physical acoustic (NJ, USA) S9225 sensors (300–1800 kHz flat frequency response) mounted to the

exterior of the tank using cyanoacrylate glue. Low frequency information (1–100 kHz bandpass filter) was collected at 18 MHz using a Reson TC 4013 (Slangerup, Denmark) hydrophone (1–180 kHz flat frequency response) submerged in the water within the tank (Figure 4-2). High-speed video was collected at 150,000 frames per second (Phantom v711, Vision Research, NJ, USA). To determine cavitation bubble diameter, a needle of known width was positioned in the high-speed frame. Based on trigger timing, the high-speed video of bubble formation and collapse was matched in time with acoustic traces and wavelet transforms of the signal.

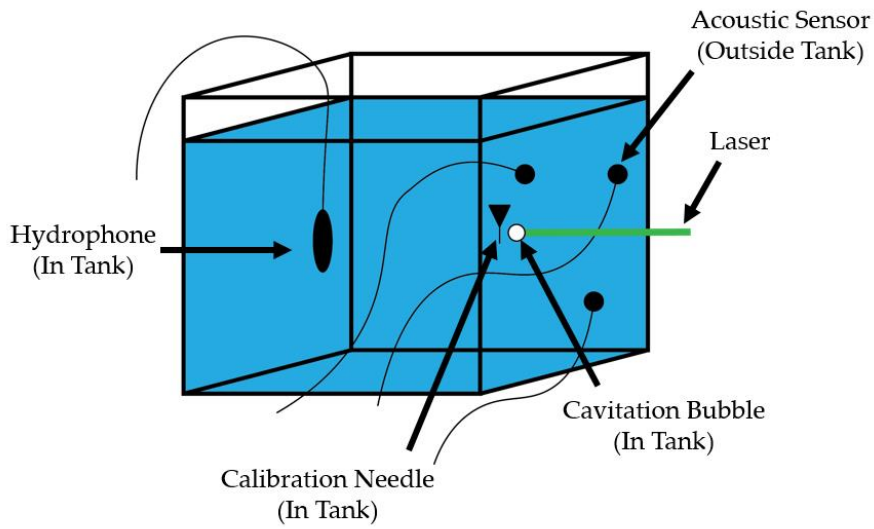

Figure 4-2: Drawing of water tank setup for laser-induced cavitation tests.

4.2.2 Blunt Impacting Device

A pneumatic impactor was constructed to produce repeatable blunt impacts for testing both an acrylic surrogate and porcine cadavers. This consisted of three components, as shown in Figure 4-3. The first was the impactor, a 5 kg aluminium mass

selected to resemble the mean human mass of an impacting head in a head-to-head collision. It was fixed to a linear track that enabled a single degree of motion along the direction of impact (Figure 4-3). The mass was attached to the track bearings using hose clamps and could be easily removed to change the overall mass of the impactor. Connected to the mass was a removable impacting puck: a rubber disk that could be exchanged to alter the impact stiffness. For these tests, a 2.5 cm thick, 70A shore neoprene rubber impacting pucks were used. The second component was a pneumatic piston with an 11.5 cm bore diameter and 45.75 cm stroke length. The piston was modified by drilling holes in the rod exit endcap to reduce the exiting air-flow restriction during the piston stroke and ensure maximum velocity. The linear track was longer than the piston stroke length, allowing the piston and impactor to decouple prior to the impact zone. This ensures impacts are dominated by the momentum interaction and not the driving piston. Last was a 113.5-litre, 200 psi rated charging tank that was regulated and large enough to provide a consistent pressure to the air piston. The tank was connected to the piston by a 2 in NPT pipe through a manual ball valve that enabled a rapid transfer of air from the charging tank to the piston. The impactor system was capable of driving the impactor mass at speeds up to 8 m/s, high enough to simulate severe blunt impacts depending on the impact stiffness (Lessley 2018).

(A) (B)

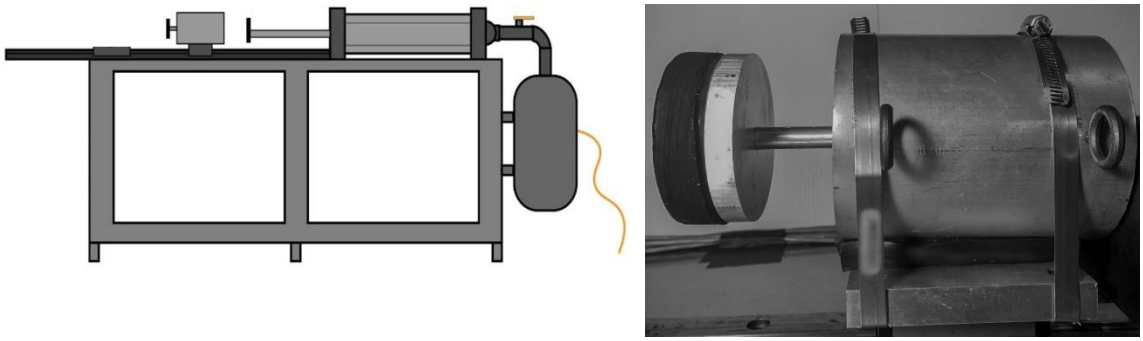

Figure 4-3: (A) Illustration of overall blunt impactor. (B) Picture of impactor used for blunt tests.

4.2.3 Acrylic Head Surrogate

Positive and negative controls for the acoustic emissions of cavitation formation were provided using a clear acrylic head form. The shell of the head form was an acrylic cylinder 14.6 cm in diameter, 14.6 cm tall, with a 0.63 cm wall thickness to resemble the approximate dimensions, thickness and volume of the human head (Figure 4-4) (Adeloye 1975, Young 1993). Acrylic was used because it closely resembles the stiffness of cortical bone, has a comparable compressive and shear speed of sound to cortical bone, and can be imaged through using a high-speed camera to capture cavitation formation (Table 4-1). Distilled water was used to fill the surrogate. It was degassed to remove bubbles, then allowed to equilibrate to CSF gas partial pressures (Yu 2019). Water was used instead of CSF because their bulk moduli (property that dictates cavitation dynamics) are similar.

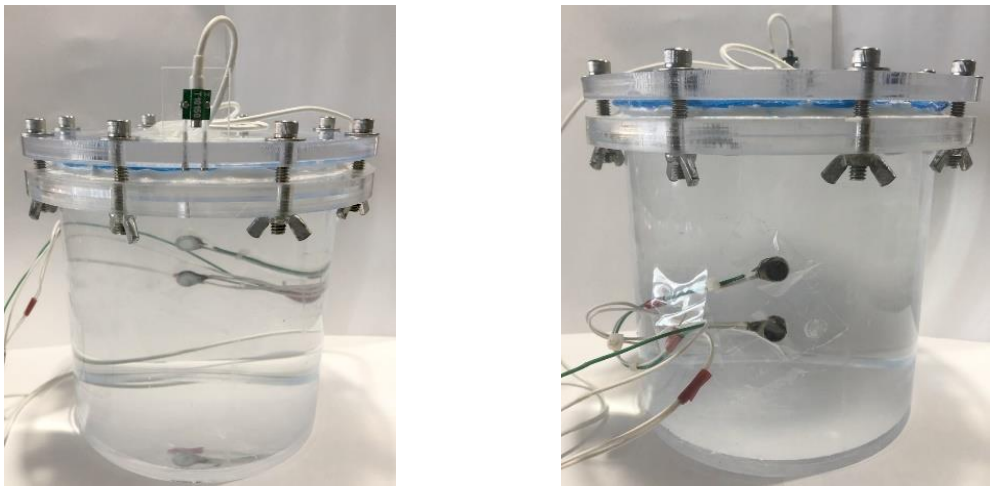

Figure 4-4: Coup (Left) and contre-coup (Right) of full sized surrogate. Accelerometer mounted on the coup and acoustic sensors mounted on contre-coup.

Table 4-1: Material Properties of Acrylic and Skull

Material	Modulus of Elasticity (GPa)	Compressive Speed of Sound (m/s)	Shear Speed of Sound (m/s)
Acrylic	**2.76–3.30**	**2746**	**1392**
	(MatWeb 2019)	(Christman 1972)	(Christman 1972)
Bone	**~5**	**1500 ± 140**	**2820 ± 40**
	(McElhaney 1970)	(White 2006)	(White 2006)

The acrylic cylinder was instrumented with two Physical Acoustics (NJ, USA) S9220 acoustic sensors (flat frequency response of 100–900 kHz) on the contre-coup using cyanoacrylate glue (Figure 4-4). One Endevco (NC, USA) 7264 linear accelerometer was rigidly secured to the lid of the surrogate, sampled at 200 kHz, and low pass filtered at 1650 Hz (NHTSA 2011) to determine the impact acceleration of the surrogate (Figure 4-4). High-speed video (Phantom v711, Vision Research, NJ, USA) was collected at two focal lengths, a wide angle at 14000 fps to image the overall impact event, and a macro angle of the contre-coup wall at 22000 fps to image the formation of cavitation bubbles.

The surrogate was struck by the pneumatic impactor at varying velocities (2.3–3.7 m/s), determined using high-speed video. Positive control was considered a test where cavitation was confirmed using high-speed footage. Negative control was considered a lower magnitude test where cavitation was not present in the high-speed footage. The high-speed video, linear acceleration, and acoustic data were aligned to the trigger signal to determine the positive and negative control cavitation acoustic emissions during a surrogate blunt impact.

4.3 Results

4.3.1 Laser Induced Cavitation Tests

Figure 4-5 depicts the beginning, middle and end video frames of a laser-induced cavitation event. The data show, at both formation and collapse, that the cavitation bubble emits a wideband frequency response with the most power between 64 and 256 Hz. The wavelet transform of the hydrophone acoustic signal for the same bubble collapse in Figure 4-5 is presented in Figure 4-6. This wavelet detects lower frequency information (32 – 64 kHz) upon cavitation collapse, but higher frequency content (> 64 Hz) is indiscernible at the point of collapse. Bubble size varied from 1.5 mm to 2.8 mm in diameter. The small variation in bubble diameter achieved by altering the power influenced the strength of the acoustic signal but did not qualitatively alter frequency content. Figure 4-7 shows the negative control of the laser firing but no cavitation formation. The wavelet transforms indicate little evidence of acoustic response beyond

noise at any frequency.

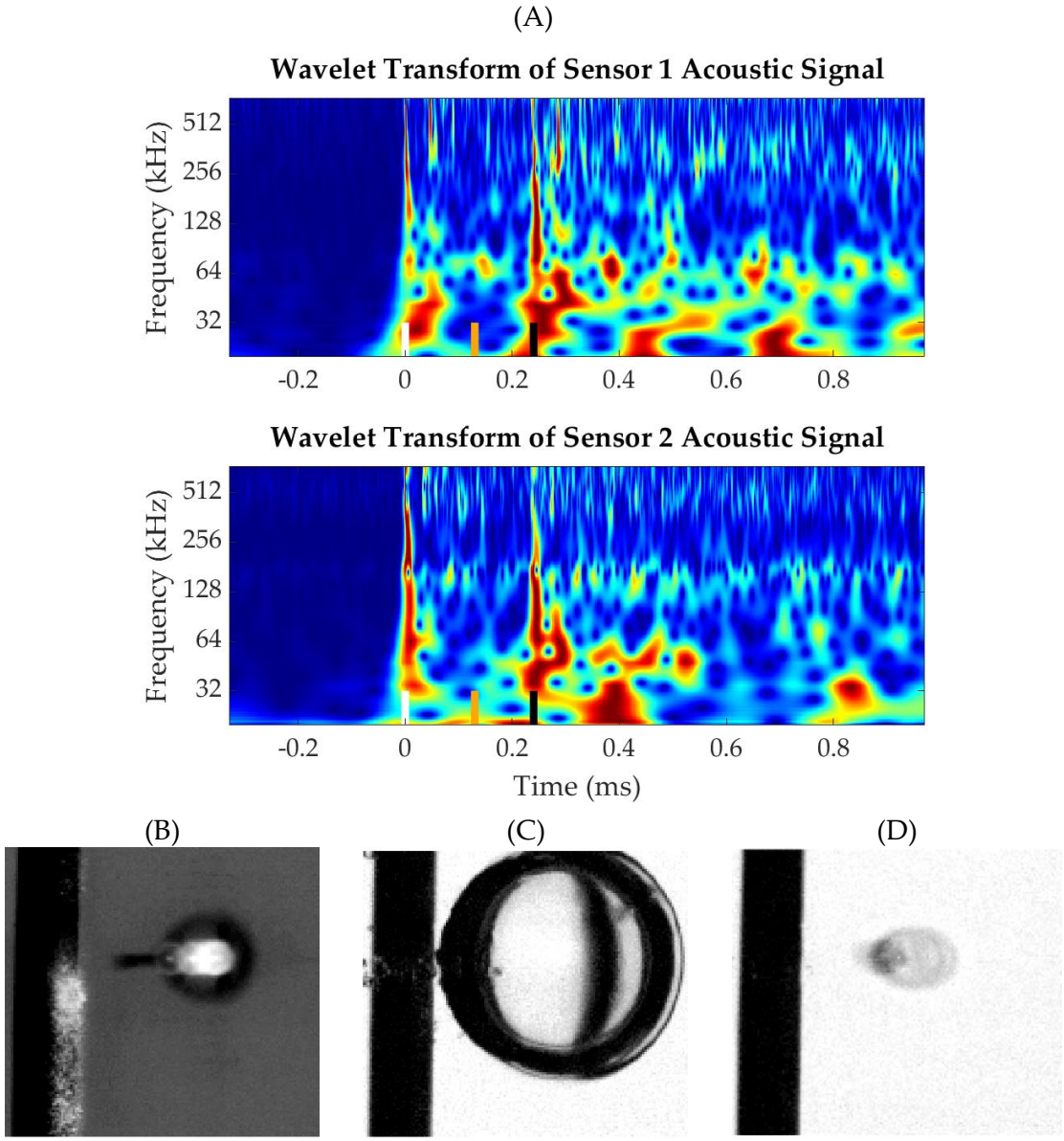

Figure 4-5: Laser induced positive cavitation (A) Wavelet plots of laser induced cavitation formation (B) Cavitation formation (white line in wavelet), (C) peak bubble size, 2.81 mm (orange line in wavelet), (D) Cavitation collapse (black line in wavelet). Strong wideband acoustic emission present at bubble collapse.

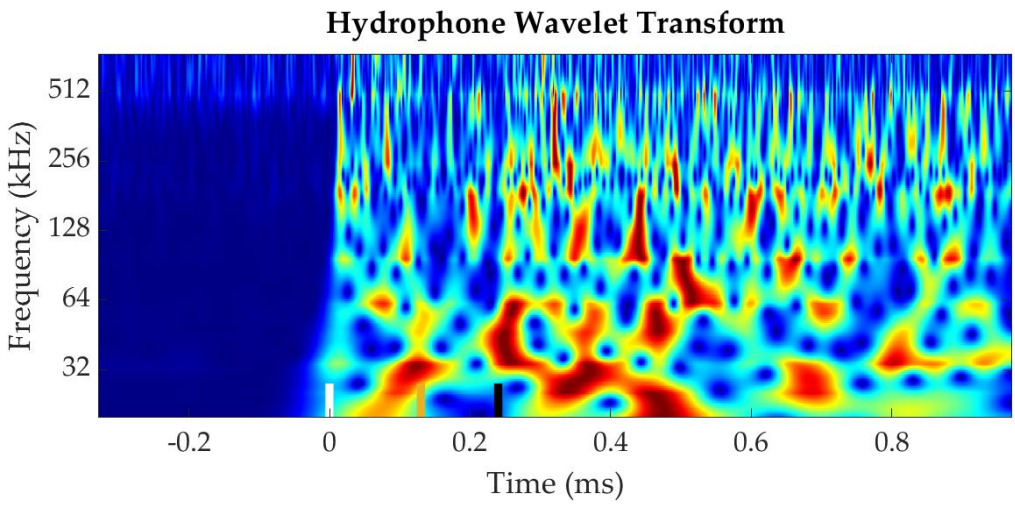

Figure 4-6: Wavelet transform of hydrophone signal from laser induced cavitation formation (white line) and collapse (black line).

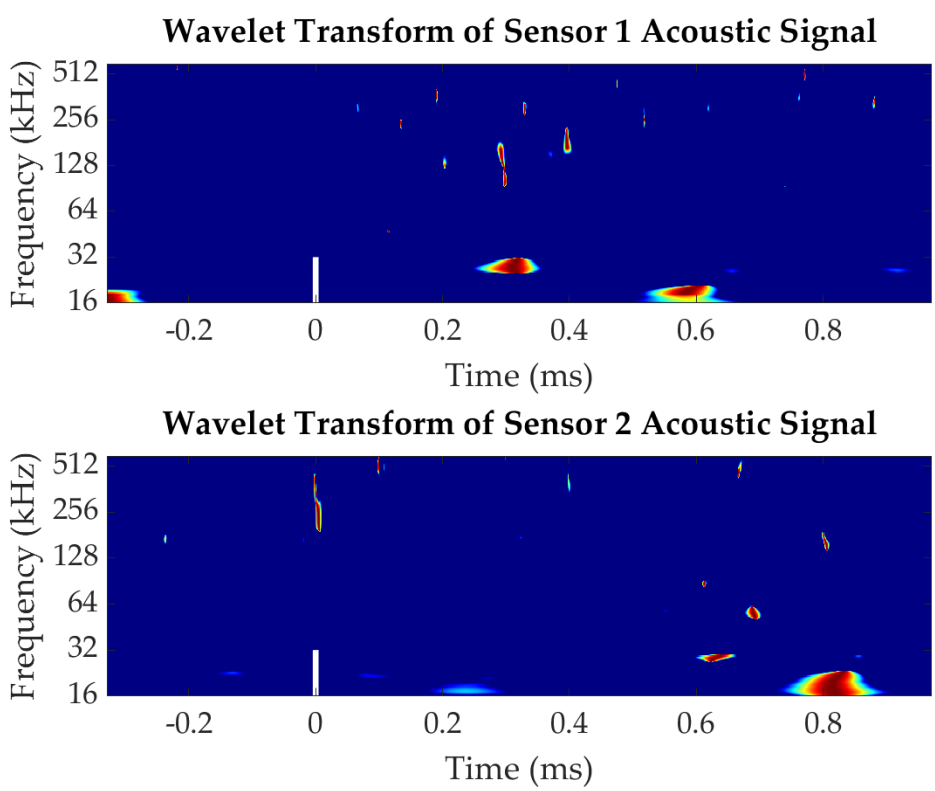

Figure 4-7: Negative control of laser induced cavitation. Laser fired into tank (time 0) and no bubble is formed.

4.3.2 Acrylic Head Surrogate

Three tests highlighted results from blunt impact tests on the surrogate: a large cavitation bubble formation (~17 mm), a medium cavitation bubble formation (~4 mm), and no cavitation formation. Figure 4-8, Figure 4-9, and Figure 4-10 display the wavelet transforms for each case respectively. Peak linear accelerations for each test were 273 g, 185 g, and 160 g, for the large bubble, medium bubble, and no bubble tests respectively. On each plot, from time synched high speed video, the grey line on the time axis indicates impact initiation while the white line indicates cavitation formation and the black line is the first cavitation collapse. The large bubble collapse occurred approximately 2.9 ms following impact while the medium bubble collapse occurred approximately 2.1 ms following impact. For the negative control test, low strength acoustic information is present at the time of impact, but 2 – 3 ms following impact, no broadband frequency data is present. The difference in broadband signal strength between the large and small bubble is 23.4 dB.

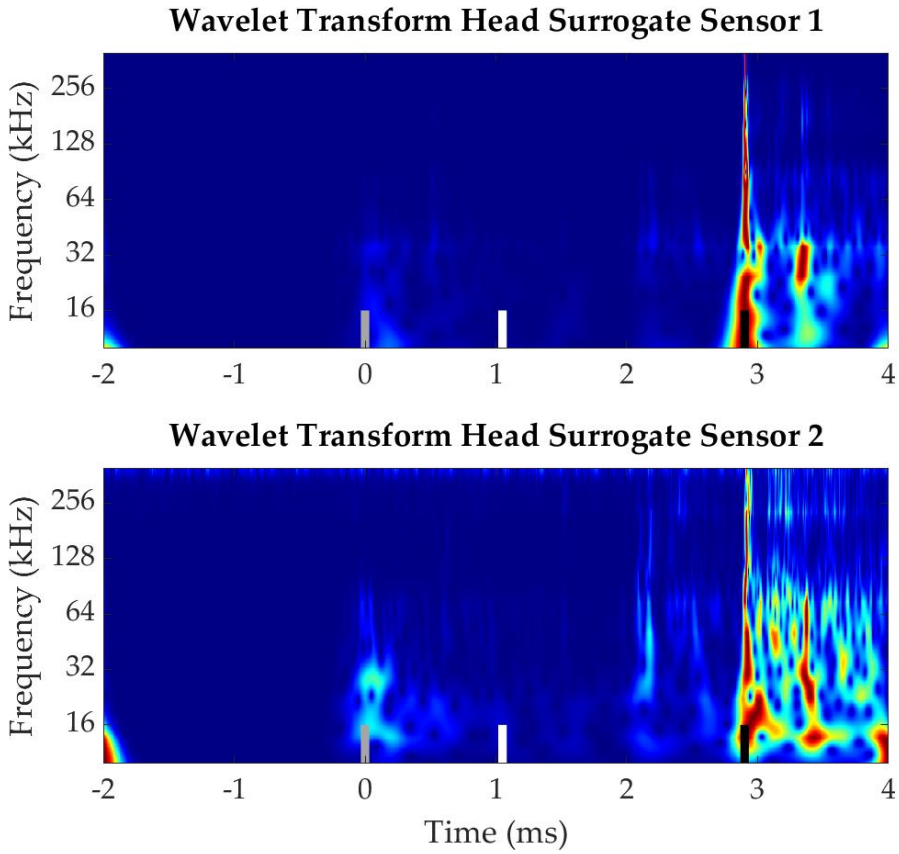

A

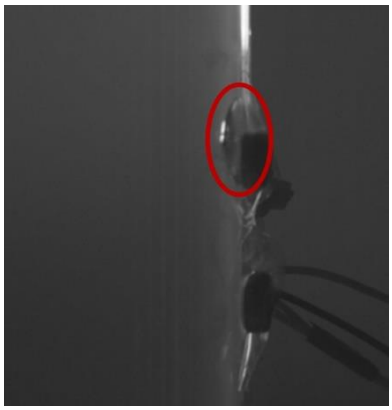

B

Figure 4-8: Blunt impact positive cavitation large bubble (A) Cavitation bubble (~17 mm) wavelet transform. 273 g peak acceleration, grey line indicates impact, white line indicates initiation of bubble formation, and black line indicates bubble collapse approximately 2.9 ms following impact. (B) Still frame of peak cavitation bubble size.

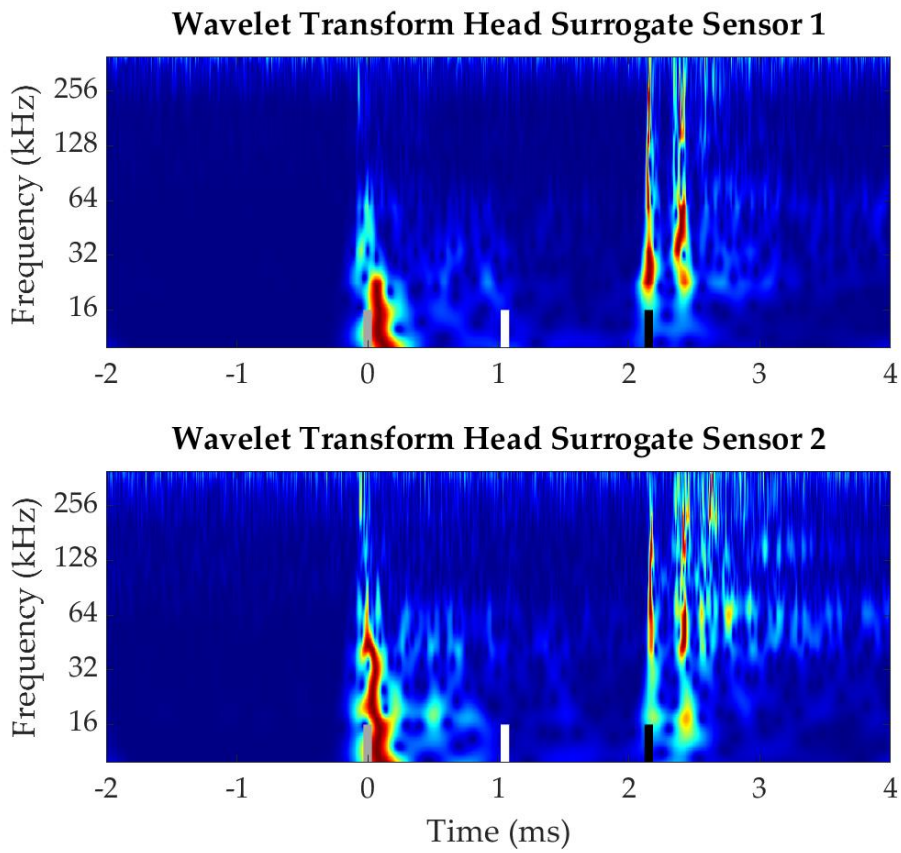

A

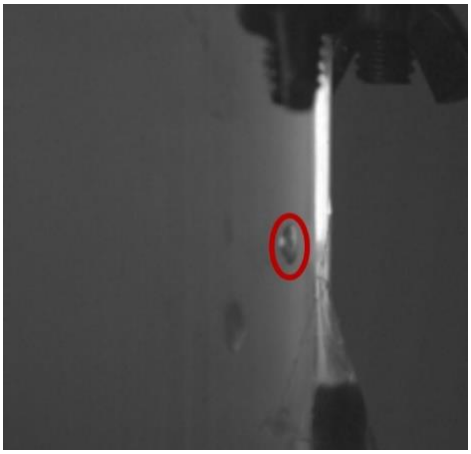

B

Figure 4-9: Blunt impact positive cavitation mini bubble (A) Cavitation bubble (~4 mm) wavelet transform. 185 g peak acceleration, grey line indicates impact, white line indicates initiation of bubble formation, and black line indicates bubble collapse approximately 2.1 ms following impact. (B) Still frame peak cavitation bubble size.

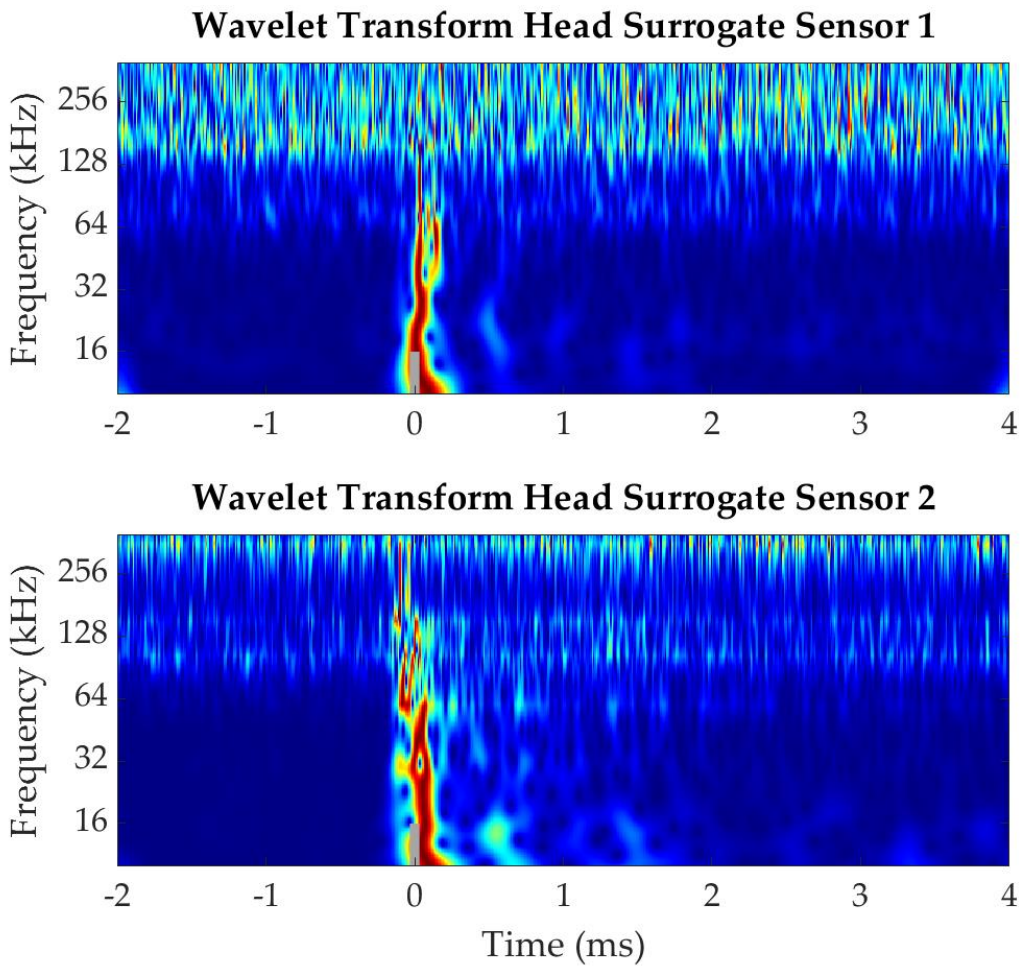

Figure 4-10: Wavelet transform of blunt impact negative control test where no cavitation bubble is seen. Impact at time 0 with low magnitude broadband response, but no acoustic response seen 1 – 3 ms following impact.

4.4 Discussion

The goal of this study was to provide a methodology to detect the collapse of acoustic cavitation and test the hypothesis that wideband acoustic emissions from cavitation collapse are distinguishable from the noise surrounding a blunt impact event. Acoustic emissions have been used in literature to detect cavitation collapse in a variety of soft tissues by observing 1 – 3 MHz frequency content. These frequency ranges are

higher than any expected content from a blunt impact. However, preliminary work indicates cavitation collapse does not emit acoustic emissions at these frequencies with enough power to transmit across the skull (Eckersley 2020). This work is an important foundational base layer to the blunt impact cavitation detection methodology, because it illustrates that the broadband emissions at frequency levels capable of penetrating the skull can be differentiated from acoustic signals associated with blunt impact.

Both the larger (~17 mm) and smaller (~4 mm) bubbles emitted acoustic signatures with similar broadband frequency content. The two signals only differed in their power and timing from the moment of impact and bubble initiation. A larger bubble resulted in an increased power and longer duration between time of impact and collapse indicating this time difference can be used to approximate bubble size in systems opaque to high speed imaging techniques.

In the laser induced cavitation tests, wideband frequency content is seen at both the initiation and collapse of cavitation bubbles, while in the blunt impact tests wideband frequency is only seen upon collapse. This is due to the nature of initiation for each of the cavitation types. The laser induced tests are a form of optic cavitation while the blunt impact tests cause an acoustic hydrodynamic cavitation. While there is variation in the bubble initiation acoustic response, the acoustic signatures of destructive collapse for both tests are expected to be similar because their shared property as transient cavitation events dominates the collapse response regardless of initiation type.

A number of limitations are present within this study. While impact velocities were representative of common injury scenarios (Lessley 2018), the high stiffness of the interaction is representative of unprotected impacts to the head. Future work will aim to develop an understanding around the plausibility of cavitation formation in a variety of impact scenarios. Furthermore, the surrogate lacked biofidelity in particular areas. The interior contents did not have any resemblance to brain, just matched properties of the CSF. This will be an added complexity in the future, but the inclusion of a gelatin brain is only expected to affect the growth and size of the cavitation bubbles, not the acoustic response or ability to differentiate the collapse from a blunt impact. Finally, the acrylic material has limitations as a surrogate for the skull since acoustic emissions in biological tissue will experience additional viscoelastic damping during transmission across the dura and additional acoustic impedance/internal reflections from the heterogeneity of a diploic skull. These differences are expected to dampen and disperse the overall broadband acoustic emission with a more profound effect on the higher frequency content (McElhaney 1970, White 2006).

4.5 Conclusion

This work provides a methodology using the wavelet transform to detect and differentiate the broadband acoustic emission of transient cavitation collapse during a blunt impact. Broadband acoustic signal can be used as a biomarker to detect the incidence of cavitation through the skull as it consists of frequencies that are low enough to

potentially pass through the skull but high enough to differentiate from blunt impact noise. This lays the necessary foundation for a vital tool to conduct CSF cavitation research in-vivo.

5. The Role of Container Compliance in Cavitation

The biological systems dictating transient cavitation from blunt impact TBI (CSF, Brain, and Dura) are contained in stiff yet compliant structures (skull). It is imperative to determine the role container compliance plays in transient cavitation to understand cavitation in biological systems.

5.1 Objectives

There are two theories on how the compliance of the material containing a cavitating fluid may alter dynamic fluid pressures and affect blunt impact cavitation. First, a compliant membrane in the system, such as the foramen magnum, not localized to the coup or contre-coup regions, will allow the system to contract and expand in response to pressure, limiting the magnitude of dynamic pressure fluctuations. This effect can be seen by modeling two rigid fluid filled cylinders, one with a membrane and one without. If an acceleration is applied to the rigid body, the negative pressures created by fluid inertia are lower in the model with the compliant membrane (Figure 5-1). While this may make it more difficult to reach cavitation thresholds, once cavitation does occur, it is hypothesized the presence of a compliant membrane will result in larger cavitation bubbles and a more violent collapse. Since water and CSF are nearly incompressible, a compliant membrane is required for bubbled to expand and increase the system volume.

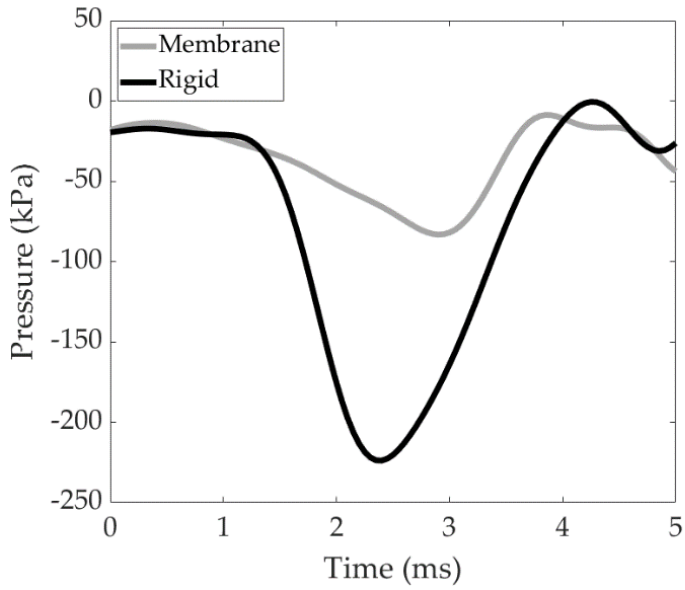

Figure 5-1: Comparison of contre-coup pressures in a rigid vessel with and without a membrane during an inertial acceleration.

The second theory in how material compliance can influence cavitation is through localized volume changes in the bulk fluid created by shear waves propagating in the container wall. Blunt impact generates a shear wave through the fluid container wall that can result in localized strains on the contre-coup side. It is hypothesized these shear wave strains generate transient localized increases (and decreases) in volume that result in localized decrease (and increase) in pressure. In combination with the pressure gradient created by fluid inertia during acceleration of the system, this localized decrease in pressure can increase the likelihood that the transient cavitation threshold is reached. The goal of this investigation was to determine the role these two theories have in transient blunt impact cavitation formation by testing the presented hypothesis using an experimental acrylic surrogate and a numerical finite element model.

5.2 Methods

5.2.1 Acrylic Pig Head Surrogate Experimental Testing

To investigate the role of compliance in blunt impact cavitation experimentally, a pig head sized acrylic surrogate was developed that mimicked previous soft tissue cavitation testing (Eckersley 2020), and was robust enough to withstand significant repetitive impacts. Acrylic was chosen for its similar material properties to cortical bone (Table 4-1) and translucent color for high-speed imaging. The pig head surrogate was an acrylic cylinder 8.89 cm tall, 7.62 cm inner diameter, and 0.63 cm wall thickness. The dimensions were chosen to resemble the intracranial cavity of a four-month-old pig determined by microCT scans. The surrogate was filled with distilled water, degassed to remove bubbles, then allowed to equilibrate to CSF gas partial pressures (Yu 2019). The pig head surrogate can be seen in Figure 5-2.

The acrylic pig surrogate was instrumented with two Physical Acoustics (NJ, USA) Nano-30 acoustic sensors (flat frequency response of 150–750 kHz) on the contre-coup side using cyanoacrylate glue (Figure 5-2). Rigidly connected to the surrogate top was a six degree of freedom sensor package with three orthogonal Endevco (NC, USA) 7264 linear accelerometers and three orthogonal DTS (CA, USA) 8K angular rate sensors (Figure 5-2). Kinematic values were sampled at 200 kHz; linear accelerations were filtered at 1000 Hz in accordance with CFC600 while angular rates were filtered at 300 Hz in

accordance with CFC180 (NHTSA 2011). High-speed video (Phantom v711, Vision Research, NJ, USA) was collected of the contre-coup wall at 14,000 fps to image cavitation.

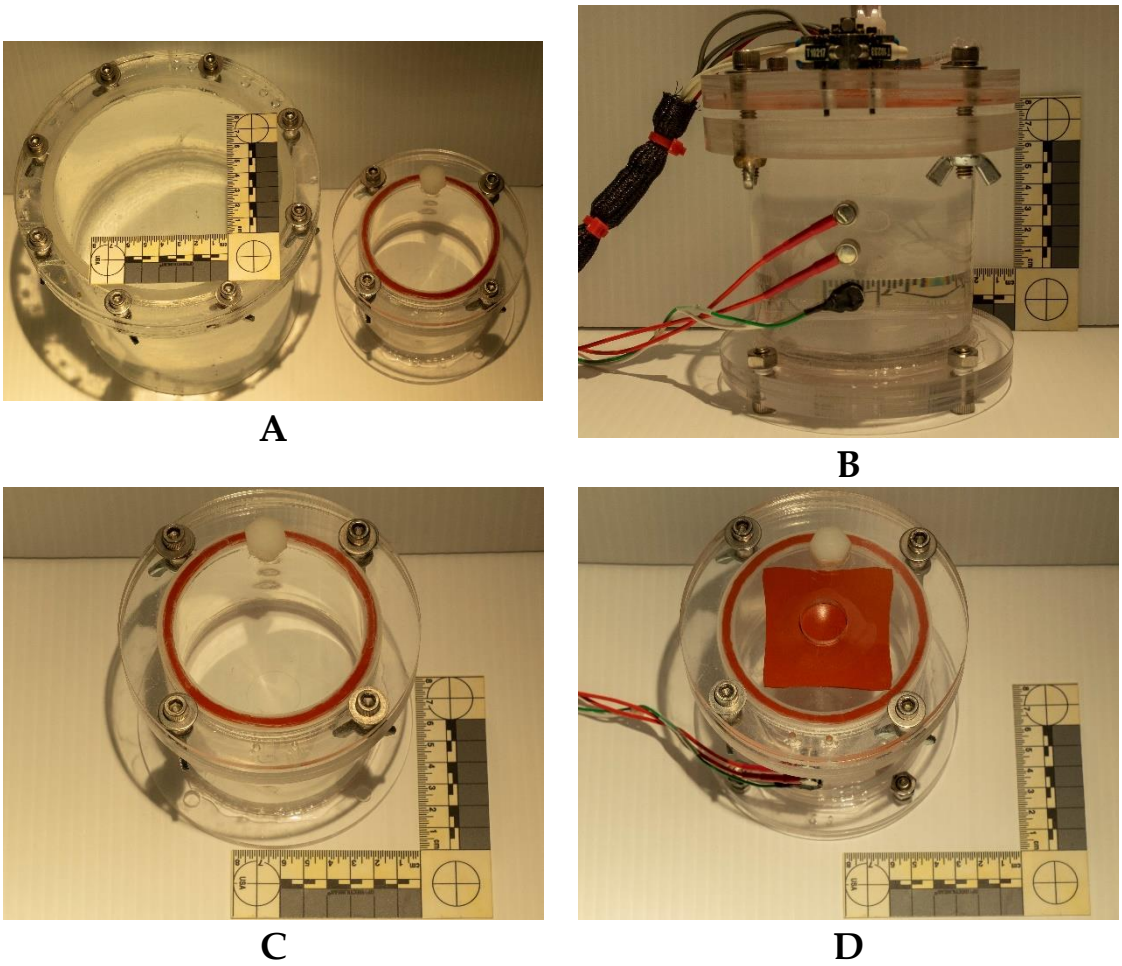

Figure 5-2: Images of the pig head surrogate. A: Comparison of pig head to full sized head surrogate, B: Instrumented pig head surrogate, C: Pig head surrogate with solid acrylic lid, D: Pig head surrogate with compliant membrane.

Two test series were conducted; one using a solid acrylic lid, and another using a lid with 20 mm diameter hole covered with a 0.32 cm thick 40A shore silicon membrane to simulate the foramen magnum (Figure 5-2). A pneumatic impactor previously designed and tested for cavitation study (Eckersley 2020) was used to strike the surrogate with a 5

kg, 70A shore neoprene impacting puck at varying velocities (2 – 6 m/s). Sixty-five tests were conducted between the two cylinders, 33 for the solid acrylic lid and 32 for the foramen lid. For the foramen lid, low-level impact tests were conducted after the highest-level impact tests to ensure system integrity throughout testing. Cavitation was detected using high-speed video and a previously developed acoustic biomarker (Eckersley 2020).

Acoustic data for all tests were collected using a PicoScope 5444B (Pico Technologies, UK) at 31 MHz, band pass filtered from 20,000 to 1,000,000 Hz using an 8 pole phaseless Butterworth filer (preliminary work determined signal outside of this band is indistinguishable from noise), and analyzed in Matlab R2020A (MathWorks, US). Wavelet transforms were conducted using a Morlet wavelet, pictured in Figure 2-7, for two principle reasons: its generic similarity to an acoustic emission trace based on rapid onset and approximately exponential falloff, and its consistent resolution in the time and frequency space. All tests utilizing acoustic analysis underwent a similar process outlined in Torrence 1998 (Torrence 1998). To prevent lower frequency information from dominating the wavelet plot (Torrence 1998) each frequency band is normalized by its maximum value so that the peak signal in all wavelet plots is 1. The noise in the acoustic signal prior to impact is approximately Weibull (Figure 4-1), but was characterized with a mean and standard deviation, true signal is considered to be five standard deviations above the mean noise. Wavelet plots presented only display this true signal.

Kinematic data were translated to the center of gravity (CG) of the surrogate head in MATLAB using rigid body kinematics. The translated kinematic data were used to calculate peak resultant linear acceleration, peak resultant angular acceleration, head injury criterion (HIC) (Equation 5.1) (Mertz 1996) and head impact power (HIP) (Equation 5.2) (Newman 2000). Peak resultant linear acceleration provides an easily calculable metric that summarizes linear acceleration exposure (Viano 2007, Broglio 2009, Mihalik 2010, Schmidt 2014). Angular accelerations transmitted to the brain through the skull produce brain strain that potentially causes mTBI; to represent angular kinematics peak resultant angular acceleration was selected (Cullen 2016). HIC was developed and validated to predict skull fracture, an injury reliant on (skull) container compliance (Newman 1980, NHTSA 2011). It is differentiated from peak resultant linear acceleration because it incorporates both impact duration and linear acceleration magnitude. HIP incorporates both linear and angular acceleration and velocity, weighting terms by the mass and rotational inertia of the impacted object (Equation 5.2) (Newman 2000). Using cavitation presence as the binary response variable, a Weibull distribution survival analysis was used to generate cavitation risk curves for each of the head injury metrics in Minitab (PA, USA). For the survival analysis, negative cavitation tests were considered right censored while positive cavitation tests were considered interval censored between the calculated metric and the lowest known value prior to cavitation initiation. This lowest

know value was determined by timing cavitation formation through high-speed video analysis and calculating the metrics at that point.

$$HIC = \left\{ \left[\frac{1}{t_2 - t_1} \int_{t_1}^{t_2} A_{res}(t) dt \right]^{2.5} \right\}_{MAX} \quad \text{Equation 5.1}$$

$$HIP = 1.1\left(A_x V_x + A_y V_y + A_z V_z\right) + 0.017(\omega_x \alpha_x + \omega_y \alpha_y + \omega_z \alpha_z) \quad \text{Equation 5.2}$$

5.2.2 Numerical Finite Element Modeling of Experimental Tests

While global kinematic values are easily obtained from experimental tests, cavitation is driven by transient pressure changes. If container material compliance resulting in localized strains influences local pressure variations, then the pressure response may differ for given global kinematics depending on the compliance of the interaction. A numerical finite element model was built to calculate transient pressures and broadly manipulate container compliance. Finite element models were solved using LS-DYNA (R901 double precision, Livermore Software Technology Corporation, Livermore CA) and were built and analyzed using LS-PrePost (Livermore Software Technology Corporation, Livermore CA) and MATLAB (MathWorks, US).

The model used eight node solid hexahedron elements and was made of five cylindrical components: the cylinder, membrane, fluid, rubber impactor puck, and massive impactor cylinder (Figure 5-3). The model is representative of one of the high impact, foramen lid experimental tests. The acrylic cylinder, compliant membrane, and rubber puck were all modeled using an elastic material model (Table 5-1). The fluid was

modeled with the same material properties as previous CSF cavitation computational modeling studies (Panzer 2012); a null material card that calculates dilatational stresses using a Mie-Grüneisen equation of state, calculates viscous deviatoric stress using dynamic viscosity, and does not calculate other deviatoric stresses (Table 5-2). This material card does not have a yield strength and behaves in a fluid like manner under small strains. The impactor mass was modeled as a rigid component with a mass of 5 kg. Both the impactor mass and rubber puck were given an initial velocity of 4.6 m/s in all tests, the impactor speed from experimental testing determined through high-speed video. Kinematic and pressure values were reported at 200 kHz. Accelerations were low pass filtered at 1000 Hz in accordance with CFC600, while pressures were filtered at 20 kHz. Pressures reported are an average of the pressure over four elements located on the contre-coup side (Figure 5-3). This is the location of cavitation formation in the experimental tests and lowest pressures during the numerical simulations. Averaging the pressure over four elements ensures that any characteristics observed in the pressure traces are not due to a numerical artifact.

To observe the influence of system compliance on localized contre-coup pressure values, the material properties of the cylinder finite element model were manipulated to five different configurations (Table 5-3). An acrylic cylinder with a silicon membrane represented the foramen lid tests, an acrylic cylinder with an acrylic membrane represented the solid acrylic lid tests, and a completely rigid cylinder represented a

system without compliance. Two cylinders with a stiffness one order of magnitude higher and one order of magnitude lower than acrylic represented comparisons of varying container compliance for the solid acrylic lid tests that could not be tested experimentally. The pressure averaged over the same four elements was compared for all the models to illustrate the influence of wall compliance on local pressure. Cross correlation analysis was used to compare pressure traces and determine likeness.

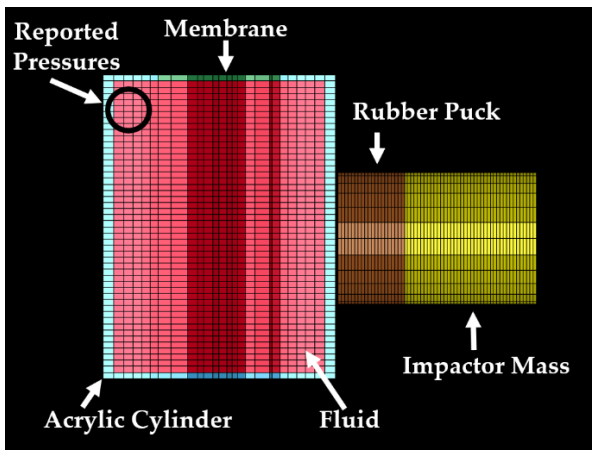

Figure 5-3: Labeled diagram of the numerical finite element model.

Table 5-1: Material properties for elastic materials

Part	Density ($\frac{kg}{m^3}$)	Elastic Modulus (MPa)	Poisson's Ratio
Acrylic Cylinder	1300	3000	0.37
Membrane	2000	1.35	0.49
Rubber Puck	1230	8	0.49

Table 5-2: Fluid material properties and Mie-Grüneisen constants

ρ: ($\frac{kg}{m^3}$)	μ: ($Pa \cdot s$)	c: ($\frac{m}{s}$)	S_1	γ_0
1000	.00089	1484	1.979	0.11

Table 5-3: Alternative compliance cases and material properties

Case	Cylinder Material	Cylinder Elastic Modulus (MPa)	Membrane Material	Membrane Elastic Modulus (MPa)
1	Elastic	3000	Elastic	1.35
2	Elastic	3000	Elastic	3000
3	Rigid	NA	Rigid	NA
4	Elastic	300	Elastic	300
5	Elastic	30000	Elastic	30000

5.3 Results

5.3.1 Acrylic Pig Head Surrogate Experimental Results

Cavitation in the smaller pig head surrogate, confirmed by high speed video, displayed the same acoustic biomarker as the full sized head surrogate (Figure 5-4). Mean time from impact to cavitation collapse was 2.4 ms (SD = 0.2) for the compliant lid surrogate and 2.5 ms (SD = 0.4) for the solid lid surrogate. The difference between the two was not statistically significant ($p > 0.05$). Bubble size varied greatly, but as reported in previous work (Eckersley 2020), smaller bubble size was correlated with lower signal power in the wavelet transform upon collapse. All cavitation formation could be identified using high-speed video for the foramen lid surrogate; five of the nine cavitation bubbles for the solid lid surrogate were too small to identify on high speed footage and were only identified through the wavelet transform identification.

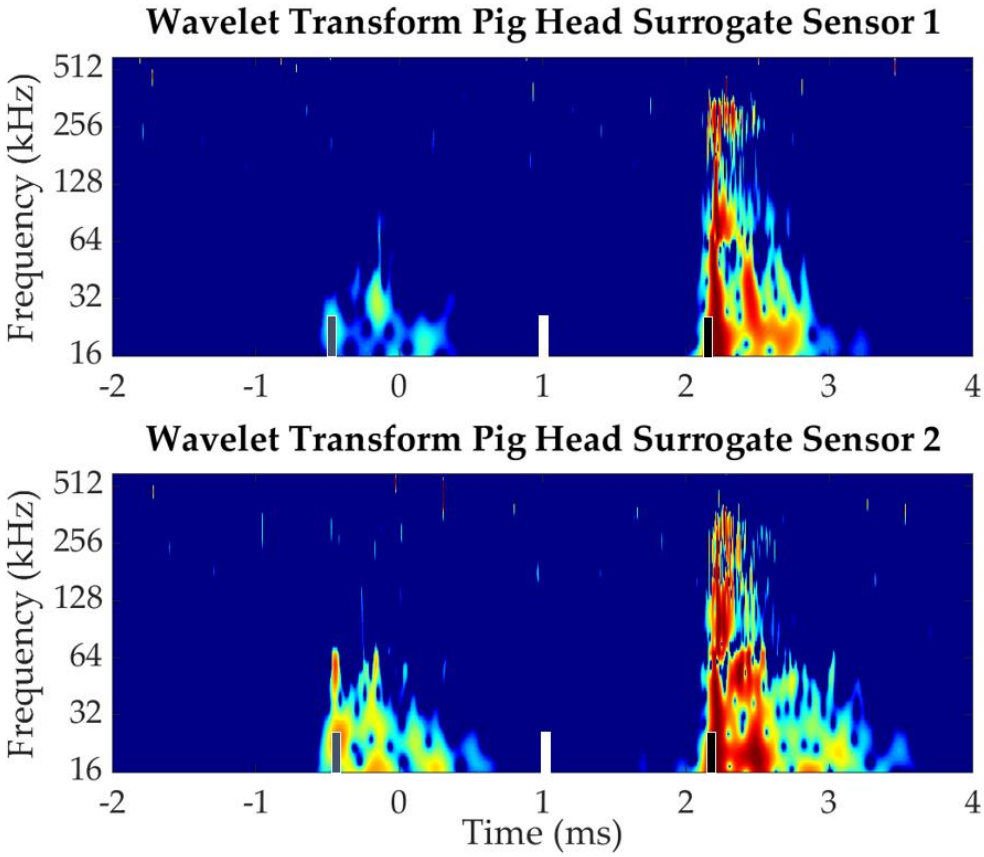

A

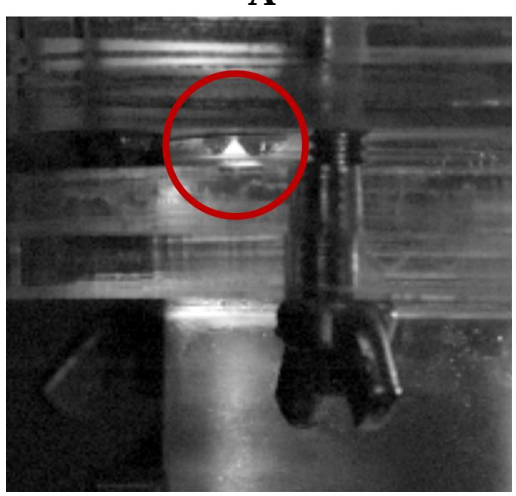

B

Figure 5-4: A: Representative wavelet transform of cavitation collapse in pig head surrogate shows previously determined biomarker. Grey line indicates impact, white line indicates initiation of bubble formation, and black line indicates bubble collapse B: High-speed video of bubble formation and timing of collapse.

Of the 32 foramen tests, 14 resulted in cavitation, while only nine of the 33 solid acrylic lid tests resulted in cavitation. Figure 5-5, Figure 5-6, Figure 5-7, and Figure 5-8 display the foramen and solid cavitation risk curves for the four calculated kinematic metrics. Of the four metrics, HIC is the best predictor of cavitation (Anderson-Darling (AD) scores of 2.1 and 3.2 for foramen and solid respectively), followed by peak linear acceleration (AD scores of 4.9 and 19.4 for foramen and solid respectively). The two metrics accounting for angular motion were both poor predictors of cavitation risk (AD scores of 25.5 and 71.1 for foramen and solid peak angular acceleration respectively, and AD scores of 56.4 and 25.8 for foramen and solid HIP respectively). HIP was the only metric where the 95% confidence intervals did not overlap at 50% cavitation risk.

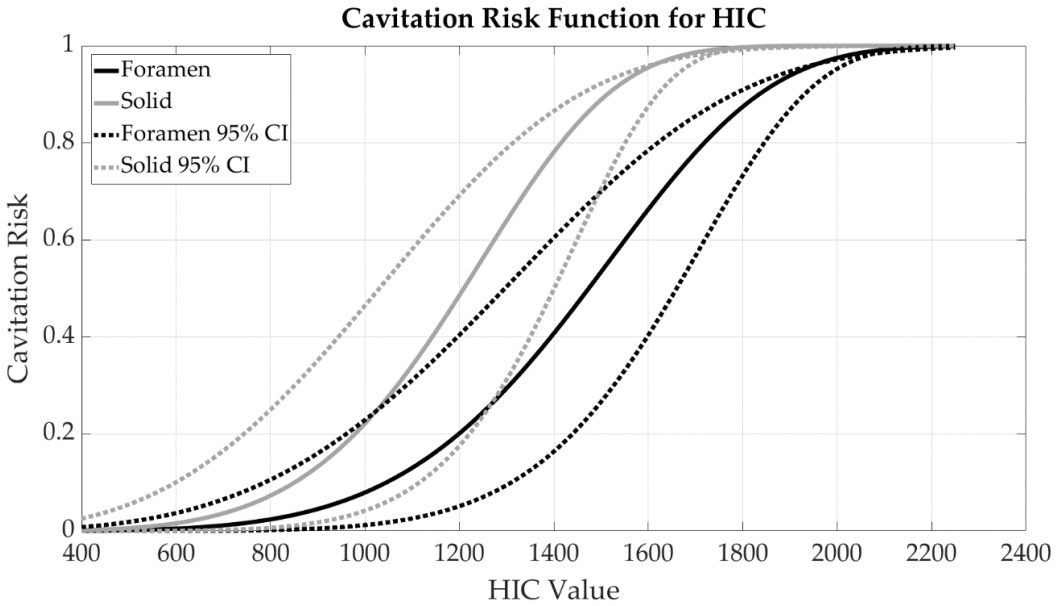

Figure 5-5: HIC cavitation risk plots of the foramen (black, AD score = 2.1) and solid (grey, AD score = 3.2) pig head acrylic surrogates.

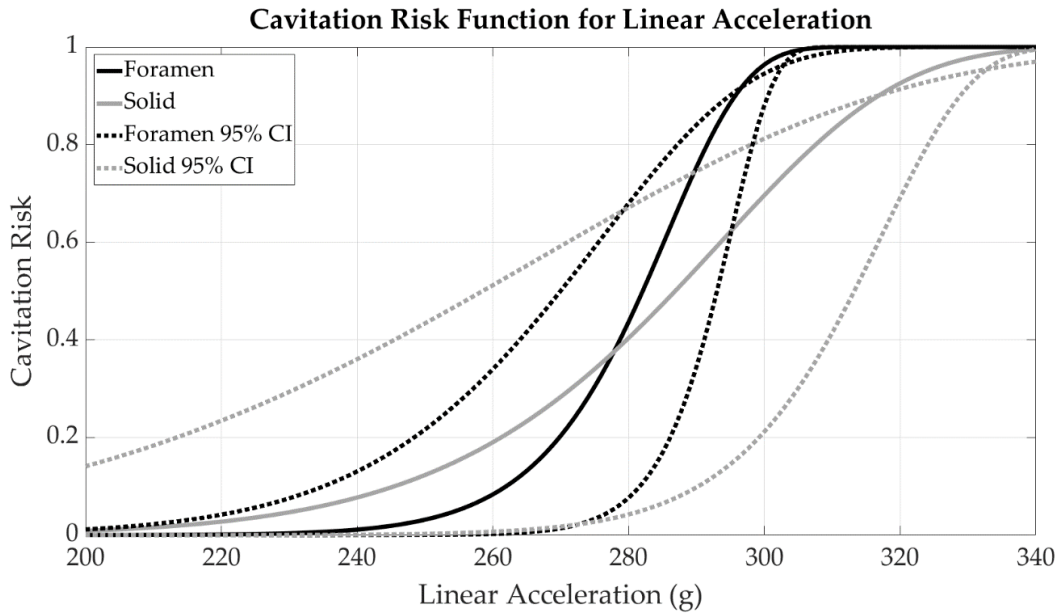

Figure 5-6: Peak resultant linear acceleration cavitation risk plots of the foramen (black, AD score = 4.9) and solid (grey, AD score = 19.4) pig head acrylic surrogates.

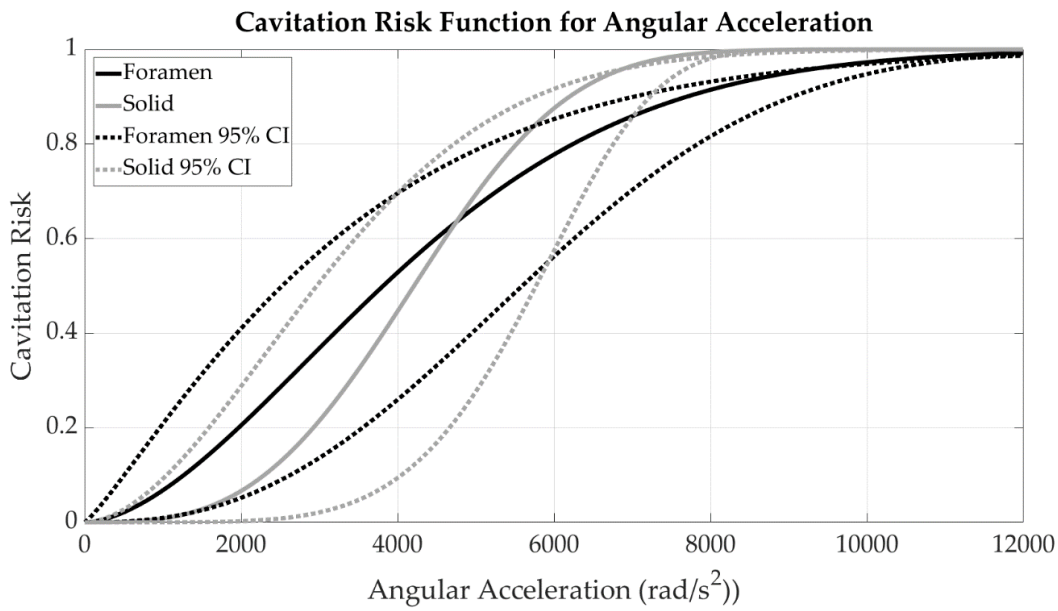

Figure 5-7: Peak resultant angular acceleration cavitation risk plots of the foramen (black, AD score = 25.5) and solid (grey, AD = 71.1) pig head acrylic surrogates.

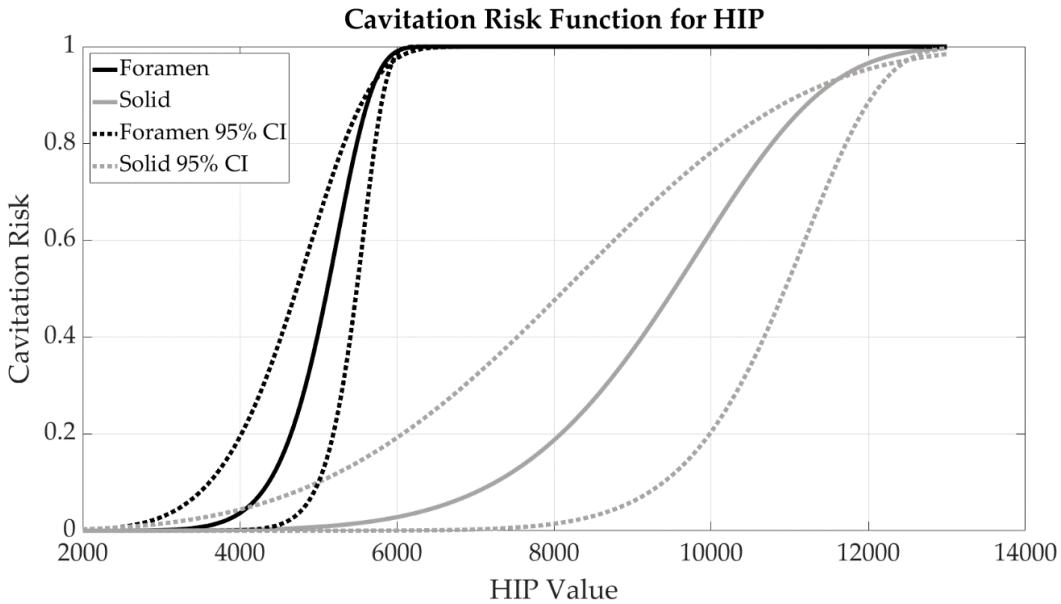

Figure 5-8: HIP cavitation risk plots of the foramen (black, AD score = 56.4) and solid (grey, AD score = 25.8) pig head acrylic surrogates.

5.3.2 Numerical Finite Element Modeling Results

Comparison of the resultant linear acceleration traces between the finite element model and the experimental test used for comparison show peaks of 352 g and 353 g for the finite element model and experiment respectively, and a difference in duration of less than a millisecond (Figure 5-9). Pressure traces comparing the foramen lid model and solid lid model with the rigid wall model show a pressure drop of approximately 150 kPa in the compliant models relative to the rigid model 1.4 ms following impact. The behavior in pressure time history varies little between the foramen model and the solid lid model.

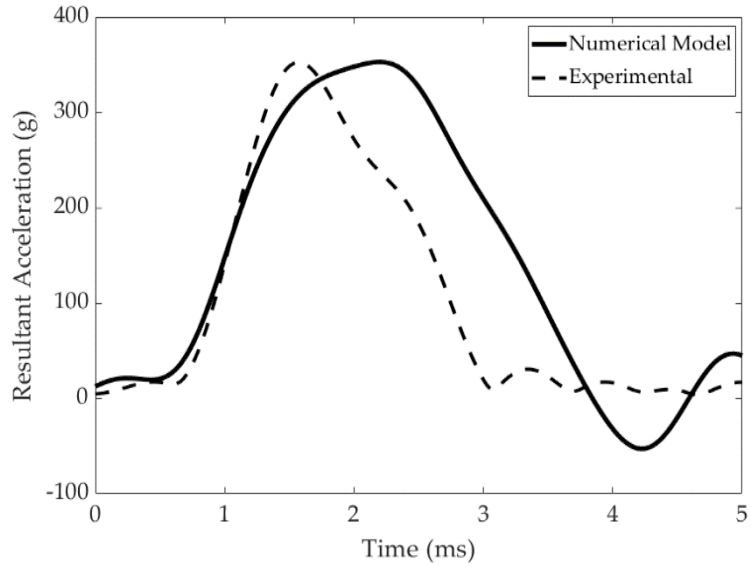

Figure 5-9: Comparison of the resultant linear accelerations the numerical model and the experiment it replicated. Comparable acceleration profiles provide a point of validation for the finite element model.

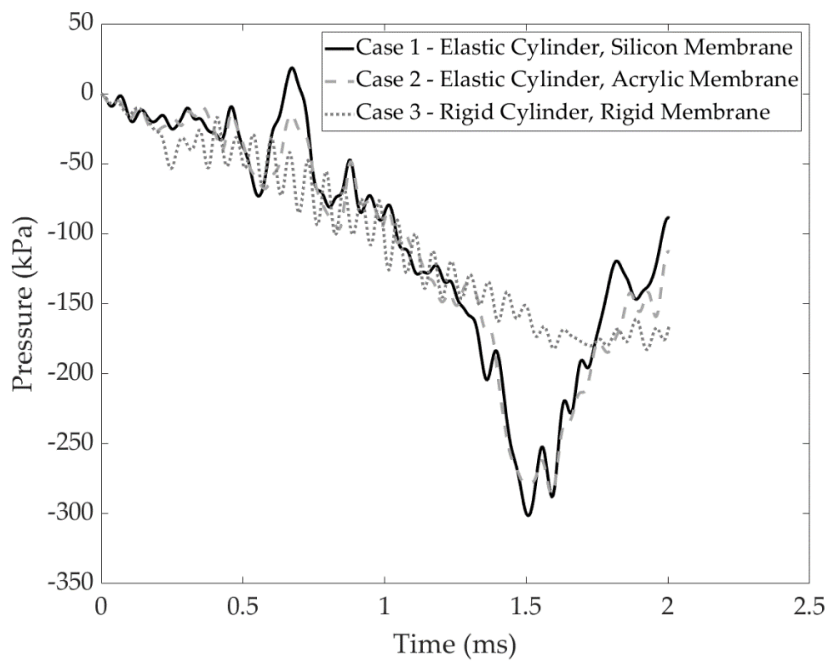

Figure 5-10: Pressure comparison of the average of four elements on the contre-coup between elastic cylinders with either a compliant silicon membrane or a solid acrylic membrane and a rigid cylinder. Plot shows the elastic cylinders experience a significant pressure drop on the contre-coup not seen in the rigid cylinder.

Changing the elastic modulus of the acrylic cylinder by an order of magnitude alters the frequency of wall strain on the contre-coup. Increasing the stiffness increases the frequency while decreasing the stiffness decreases the frequency (Figure 5-11). When pressure traces are plotted against the strain of the adjacent wall, fluctuations in pressure mirror changes in strain. Cross correlation analysis of the pressure traces against the strain show a single peak in the correlation coefficient around zero lag, indicating the traces are strongly correlated (Figure 5-12, Figure 5-13, and Figure 5-14).

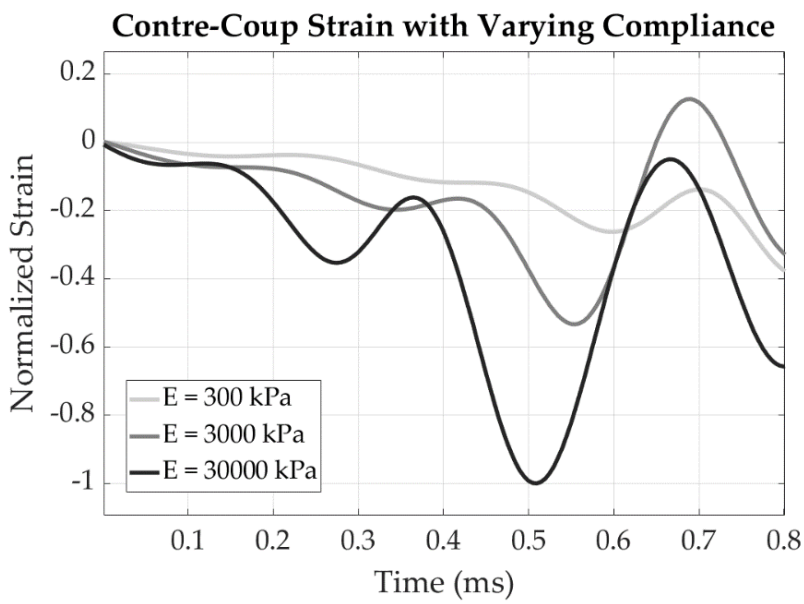

Figure 5-11: Increasing container stiffness increases contre-coup strain frequency

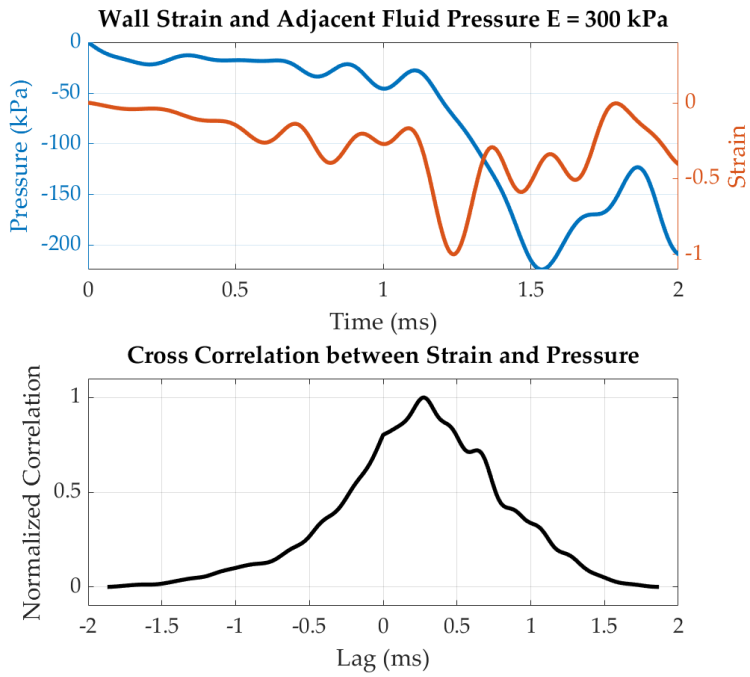

Figure 5-12: Comparison of contre-coup wall strain and adjacent pressure for model with a container stiffness of 300 kPa , one order of magnitude less than acrylic.

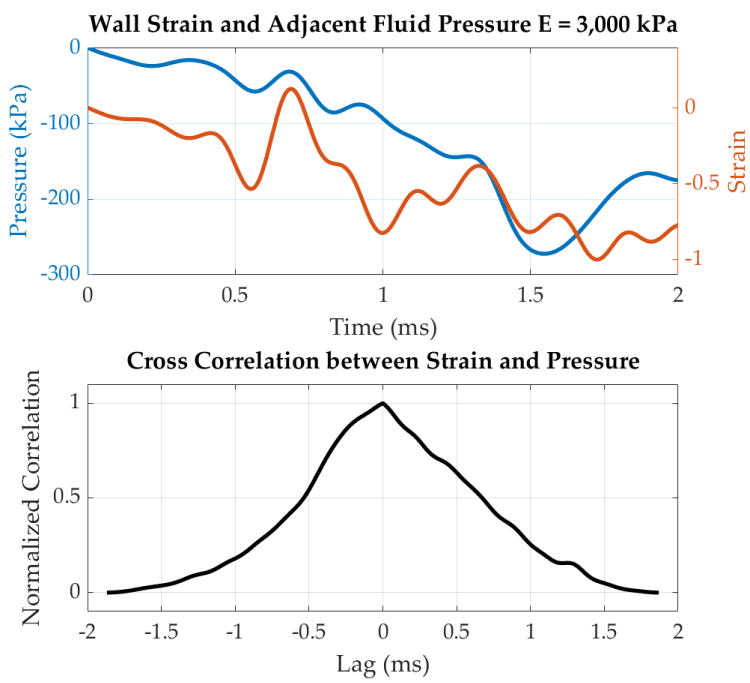

Figure 5-13: Comparison of contre-coup wall strain and adjacent pressure for acrylic model, container stiffness of 3,000 kPa . Cross correlation indicates similarity.

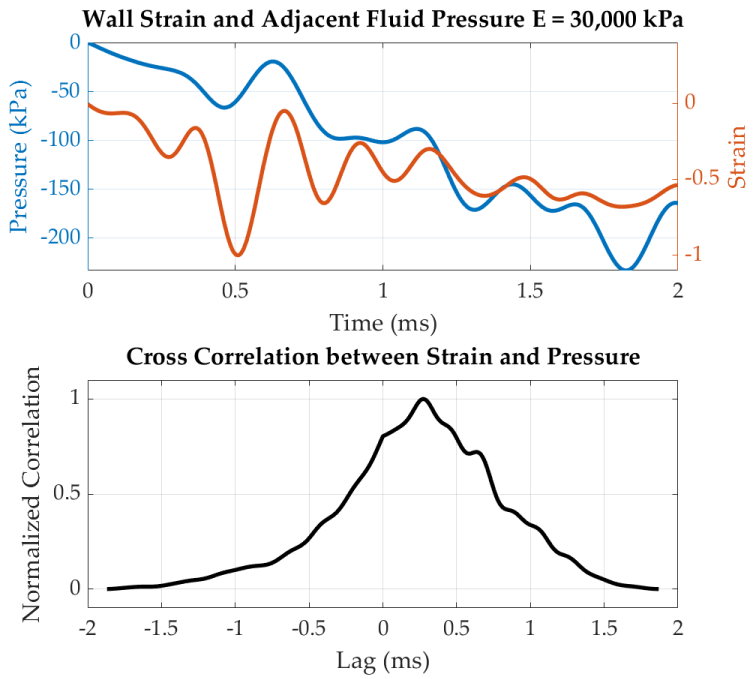

Figure 5-14: Comparison of contre-coup wall strain and adjacent pressure for container stiffness of 30,000 kPa , an order of magnitude higher than acrylic.

5.4 Discussion

The goal of this investigation was to assess the source of transient acoustic cavitation formation. The data supported the hypothesis that container wall shear waves generated transient localized increases in volume that resulted in localized decreases in pressure, influencing cavitation. The compliance of the system, or the compressive and shear modulus, influenced the localized contre-coup strain of the finite element surrogate (Figure 5-11). Increasing the compressive and shear stiffness increased the frequency of strain variation while decreasing the stiffness decreased the frequency of strain variation. The cross correlation analysis of contre-coup wall strain and the pressure variations of adjacent fluid elements show the contre-coup pressure is dictated by localized contre-

coup wall strains (Figure 5-12, Figure 5-13, and Figure 5-14). The effect localized wall strain has on these pressure variations compared to inertial acceleration is illustrated in Figure 5-10. The pressure of the compliant acrylic cylinders drops 150 kPa relative to the rigid cylinder for the same impact indicating this 150 kPa pressure drop is a result of local wall strain. The correlation between the drop in pressure from local wall strain and cavitation is observed in the bubble timing from the experimental case this model replicates. Cavitation initiation in the experiment occurs approximately 1.45 ms following impact, the same time the pressure trace approaches its minimum (Figure 5-15). This shows that wall compliance of the container being impacted has a direct influence on the formation of cavitation bubbles.

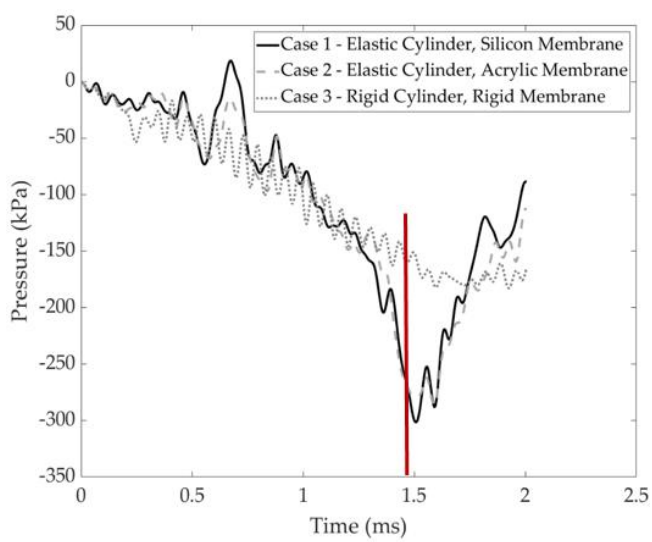

Figure 5-15: Negative drop in pressure corresponds with experimental bubble incidence (Red Line).

The finite element model was validated for accuracy by comparing the resultant linear accelerations of the model to those from the experiment used to dictate the initial

velocity of the impactor. Nearly identical peak accelerations and comparable durations confirmed the model was an accurate representation of the overall dynamic experimental conditions.

Confirmation of the acoustic biomarker, developed in a larger head surrogate, upon cavitation collapse in the pig sized surrogate indicates cavitation can be detected in smaller systems (Eckersley 2020). Changing the size of the surrogate system did not alter the frequency response or timing of the signal with cavitation collapse. This result allows the biomarker to be confidently deployed for smaller animal experimental models with potential caveats for more compliant brain/skull systems such as those in rodents.

The cavitation risk plots produced by the survival analysis of the experimental data indicate the presence of a compliant membrane did not influence the threshold of cavitation measured by peak resultant linear acceleration, peak resultant angular acceleration, or HIC. The risk plots did indicate that the presence of a compliant membrane lowers the HIP values that produce cavitation formation. However, the high Anderson Darling coefficients for HIP (56.4 and 25.8) indicated it was a poor predictor of cavitation formation. This limited the conclusions that can be drawn from the HIP cavitation risk curves. These results contradicted the hypothesis that the presence of a membrane required higher kinematics to reach a negative cavitation threshold. This contradiction can be attributed to the fact that the system compliance in these experiments

was dominated by the compliance of the acrylic cylinder, not the silicon membrane. Since this property was equal for both head surrogates, there is little difference in compliance.

The pressure traces from the numerical finite element models comparing the acrylic cylinders with and without a compliant membrane illustrated container wall properties dominate the system compliance, not the silicon membrane (Figure 5-10). The two pressure traces of the acrylic cylinder with and without a membrane are similar in appearance, and Figure 5-16 shows the cross correlation plot between them. The plot coming to a sharp peak at zero lag indicates the traces are highly correlated.

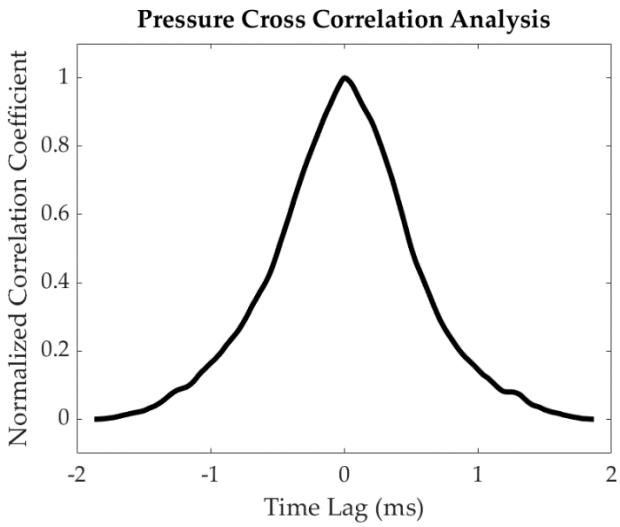

Figure 5-16: Cross correlation analysis comparing contre-coup pressure traces of same level impact of the finite element model with and without silicon membrane.

HIC was determined to be the strongest predictor of cavitation formation. HIC accounts for the duration of acceleration, and was created and validated to predict skull fracture in blunt impact trauma, an injury with a mechanism rooted in skull compliance (Newman 1980, NHTSA 2011). Based on the influence of system compliance on cavitation,

it is logical that HIC is the best predictor for cavitation formation. While HIC tangentially accounts for skull compliance, none of the other traditional head injury metrics (peak resultant linear acceleration, peak resultant angular acceleration, HIP, or Gadd Severity Index) or new model based injury metrics (Brain Injury Criterion, Maximum Principle Strain, Cumulative Strain Damage Metric, and Diffuse Axonal Multi-Axis General Evaluation) consider skull compliance. When developing future injury metrics, it is important to consider the role of skull compliance in cavitation and TBI to develop more accurate injury predictors.

The influence of system compliance on cavitation formation translates to some profound implications for CSF cavitation within the skull. The foramen magnum and other holes in the skull where soft tissues enter do not have a significant influence on the cavitation response of the system. When designing surrogates or other experimental models, it is more important to match the stiffness and overall geometry of the model to the biological system than anatomical details such as the foramen magnum. Because stiffness of the calvarium changes so much with age, scaling for cavitation by age, particularly pediatrics, requires more complexity that current biomechanics scaling laws.

While the presence of a foramen did not influence transient cavitation initiation, this work supported the hypothesis that a foramen resulted in larger bubble size. Since cavitation fluid is nearly incompressible, the presence of an elastic membrane allows for rapid volume expansion and enables the bubble to grow. This is important because the

skull has features (such as the foramen magnum) that will also allow for this expansion. Intracranial cavitation will not be limited by changes in volume, but instead interfaces such as the dura and parenchyma. This means transient cavitation will have close relation to these structures that may result in damage.

This investigation has a number of limitations. The first is the biofidelity of the experimental setup and finite element model. While the stiffness, size, and fluid properties were similar to those in tissue, geometric complexity, soft tissue properties, and anatomical complexity differ greatly. While the distilled water had partial gas pressures comparable to CSF, it did not contain any of the salts, proteins, or other large biological molecules that may act as nucleation sites for cavitation. This limitation, however, is conservative, reducing the potential for cavitation in the model compared to the *in-vivo* state. While the acrylic surrogates have similar stiffness and density to human skull, their viscoelastic properties vary. Due to its fluid content, the skull will dampen the shear wave created by blunt impact, limiting its influence on cavitation compared to acrylic. While consistent, the temperatures for testing were lower than body temperature which alters cavitation thresholds. This work was controlled to provide insight to the mechanisms and behavior of CSF cavitation. However, it is beyond the scope of conclusions to apply the risk thresholds, injury metrics, or pressure values to soft tissue CSF cavitation.

5.5 Conclusions

This work used experimental acrylic head surrogates and a numerical finite element model to investigate the role container compliance has on transient acoustic cavitation formation. It was determined that the presence of an elastic membrane, or foramen, does not influence cavitation formation but does affect cavitation bubble size. This is because instead, the compliance of the container wall is a primary driver of cavitation formation and overshadows influence from a foramen or membrane. These results provide novel insight to the mechanisms of transient intracranial CSF cavitation formation from blunt impact. Conclusions provided in this work will be fundamental in the understanding the role of transient cavitation in blunt impact mTBI.

6. Blunt Induced Cavitation in a Pig Model

6.1 Objectives

Previous work on CSF cavitation has found that cavitation can occur in non-biological surrogates (Lubock 1980, Nusholtz 1995, Van Orman 2020), but attempts to detect intracranial CSF cavitation in soft tissue have been limited to contre-coup pressure traces in backfilled human cadaver head and live rhesus monkeys (Nusholtz 1984). These tests were unable to discern the incidence of cavitation, and required compromising the cranial cavity to implant pressure transducers. Cavitation has been shown to have implications for neurological and vascular damage given its potential occurrence within the brain (Canchi 2017, Wrede 2019, Dougan 2020). However, to advance the understanding of cavitation in blunt TBI, cavitation must be detected within the soft tissue of a biofidelic model.

The recent development of an acoustic biomarker capable of detecting transient cavitation collapse without compromising the skull presents the opportunity to observe cavitation in the cranial cavity of a fresh non-frozen pig cadaver model. It is hypothesized that cavitation will occur within an uncompromised pig head at impact levels relevant for human blunt impact injury *in-vivo*, and the acoustic biomarker developed and validated in an acrylic surrogate model can be detected through biological tissue. This hypothesis is tested through repetitive impacts of a fresh non-frozen pig cadaver model. The following work advances the scientific field by detecting blunt impact within the cranial cavity and

provides foundational work for investigating the clinical implications of cavitation in blunt impact neurotrauma.

6.2 Methods

6.2.1 Repetitive Impacts for Cavitation Detection

Fresh, non-frozen, full-body pig cadavers were tested 3–5 hours post mortem to investigate cavitation formation without compromising the cranial cavity. The pig was instrumented with two Physical Acoustic S9220 acoustic sensors (flat frequency response of 100–900 kHz) and a six degree-of-freedom (6DOF) kinematics package (three Endevco 7264 linear accelerometer, three DTS angular rate sensors). Skin on each side of the head was cut using a cautery tool to expose both the left and right temporal fossa of the pig. One acoustic sensor was then fixed to each of the temporal fossa using cyanoacrylate glue (Figure 6-1). The cautery tool was also used to expose a square window on the nasal bone of the pig where the 6DOF kinematics package was rigidly fixed with bone screws (Figure 6-1). This sensor setup left the frontal bone unobstructed, providing the collision site for the impact. The cadaveric pig head was exposed to impacts of increasing severity from a 5 kg pneumatic impactor outlined in previous cavitation studies (Eckersley 2020). Prior to each test, the impact site of the frontal bone was lined up with the impacting mass, and high-speed footage confirmed uniform impact sites for each tests (Figure 6-1). Sixty-four total impacts were conducted between two pigs with impact velocities ranging from 1.5 to 5 m/s. For each test series, initial low-level impacts were gradually increased to the

highest levels, and then down again. This ensured the acoustic response was the same at the beginning and end of the test series, and highest-level impacts did not compromise the system.

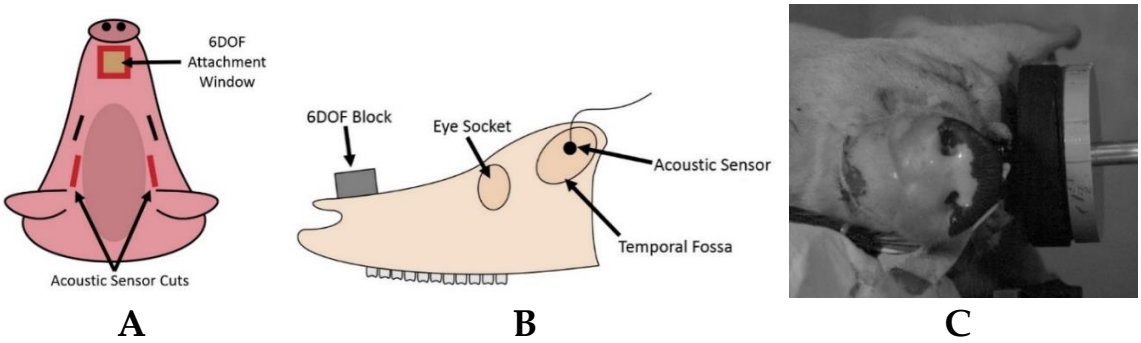

Figure 6-1: A) Illustration of surgical cut sites on cadaver pig head. B) Sensor mounting points on cadaver skull. C) Impact location of cadaver head in all tests.

Acoustic data for all tests were collected using a PicoScope 5444B (Pico Technologies, UK) at 31 MHz, band pass filtered from 20,000 to 1,000,000 Hz (Eckersley 2020), and analyzed in Matlab R2020A (MathWorks, US). Wavelet transforms were conducted using a Morlet wavelet, pictured in Figure 2-7. Wavelet analysis was conducted using a process previously determined for intracranial cavitation detection (Eckersley 2020). Kinematic data was collected at 200 kHz; linear accelerations were filtered at 1000 Hz in accordance with CFC600 while angular rates were filtered at 300 Hz in accordance with CFC180 (NHTSA 2011). Using rigid body transformations, kinematics were translated from the snout to the CG of the head. Peak resultant linear acceleration, peak resultant angular acceleration, head injury criterion (HIC) (Equation 5.1) (Mertz 1996) and head impact power (HIP) (Equation 5.2) (Newman 2000) were then calculated using the translated kinematics. For each of the head injury metrics, survival analysis using a

Weibull distribution was used to construct cavitation risk curves in Minitab (PA, USA). Incidence of cavitation was the binary response variable, and head injury metrics were the explanatory variables. Negative cavitation tests were considered right censored data points while positive cavitation tests were considered interval censored between the calculated peak values and lower values before cavitation initiation. Because cavitation cannot be directly imaged through the head, and transient acoustic cavitation can only be heard upon collapse, timing of cavitation formation was determined based on a prior test series that used an acrylic surrogate to image blunt impact cavitation formation and collapse. These tests found that on average, cavitation formation begins at 60% of the time it takes from impact to bubble collapse. Time of impact was found using kinematic traces while time of collapse was determined using acoustic wavelet transforms. The difference in time between these two values was multiplied by 0.6 then added to the impact time to determine the time of bubble initiation in the pig cadaver tests.

Following the full-body cadaveric pig tests, the head was removed, and a microCT scan was performed to check for any structural failures from the tests. Then, the head was prepped for a series of negative control tests using the same instrumentation from the full body cadaver tests. The brain and all cranial contents were removed through the foramen magnum, leaving only air in the cranial cavity thus making CSF cavitation impossible and leaving only skull/flesh structural response. The empty cranial cavity was then impacted using the pneumatic ram at velocities ranging from 3 – 4.5 m/s to determine the acoustic

response of the structural head components alone. Next, the cranial cavity was filled with a solid polyurethane resin to prevent any acoustic response from skull flexure at impact. Again, the polyurethane filled cadaver head was impacted using the pneumatic ram (3 – 4.5 m/s) and the acoustic response of the rigid system was recorded. Kinematic and acoustic data collection and analysis methodology presented in the full-body pig cadaver tests was repeated for the negative control tests.

The acoustic biomarker used in this study was developed in an acrylic surrogate model (Eckersley 2020). Because there is variation in the acoustic damping between skull tissue and acrylic, a transmission test at 40 kHz was conducted to ensure the acoustic biomarker could still be detected in the head. Similar to the control tests, a fresh cadaveric pig head was removed from the body and the cranial contents were removed from the foramen magnum. Acoustic sensors were positioned at the same locations on the head as the impact studies and the skull was back filled with water. A 40 kHz speaker was then placed inside the skull at full power and the acoustic signal was recorded on the outside of the skull. The same test was then performed for an acrylic surrogate skull, it was filled with water and the speaker was placed inside while acoustic information was recorded from sensors glued to the outside of the walls. In each test careful consideration was taken to ensure similar locations of the speaker relative to the sensor. A wavelet transform visualized the frequency information for the acoustic signals, ensuring a majority of the power was around 40 kHz. The signals received a band pass filter from 30 – 50 kHz. The

peak power was found in this frequency band for each of the two sensors on the cadaver and the surrogate. The values from each sensor were then averaged and the averages between the cadaver and surrogate were compared to determine the damping difference in dB between skull tissue and acrylic.

6.2.2 Perfused Pig Cadaver to Investigate Clinical Implications of Cavitation

Since multiple impacts were conducted on the same specimen to develop risk curves for cavitation bubble formation, neither necropsy nor histology could be used to determine the clinical implications of cavitation on the brain and its vasculature. To observe the influence of a single impact on the brain and cerebral vasculature, this test series deployed a single impact on fresh non frozen pig cadavers that allowed for comparison between intracranial tissue that was and was not exposed to cavitation.

Two pig cadavers were used in this test series. Just prior to euthanasia, the specimens were injected with a 40,000 IU bolus of heparin to prevent clotting within the cerebral vasculature. Immediately post-mortem, the external jugular vein and carotid artery were located through the ventral side of the neck (Figure 6-2). A cannula was inserted into each vessel and flow to the caudal portion of the body was blocked by clamping a hemostat caudal of the cannulas as well as on the internal jugular veins and contralateral external jugular and carotid artery. The brain was then perfused with 0.9% saline until liquid ran clear. Following perfusion, the pig cadaver was instrumented as described in the repetitive impact tests with two acoustic sensors (Physical Acoustics

Nano-30, flat frequency response 150 – 750 kHz) located on the left and right temporal fossa and a six DOF sensor package (Endevco 7264 Linear Accelerometer and DTS Angular Rate Sensor) fixed to the snout (Figure 6-1).

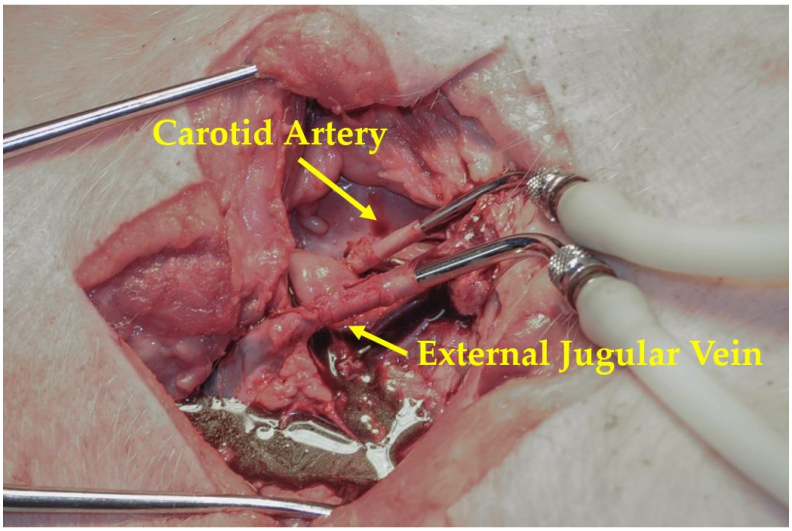

Figure 6-2: Cannulation of carotid artery and external jugular vein.

After the cadaver was instrumented, perfusion continued to ensure the vasculature was pressurized and a single impact was delivered to the frontal bone (Figure 6-1). Immediately after impact, the specimen was perfused with a 200 mL solution of 0.25% Evans blue and 3.5% albumen in 0.9% saline to indicate breaches in the blood brain barrier indicating vascular damage. The brain and vasculature were then fixed with a neutral buffered 10% formalin solution perfusion for 25 minutes. The calvarium was then removed to expose the brain, which was dissected out for analysis.

Following complete fixation of the brain, the external cortex was examined for any locations of diffuse Evans blue dye that would indicate blood brain barrier disruption.

The brain was then sliced into 5 mm thick coronal sections and examined for any interior diffuse blue discoloration. The acoustic and kinematic data were analyzed in accordance with the methodology described for the repetitive impact tests.

6.3 Results

6.3.1 Repetitive Impacts for Cavitation Detection

Cavitation was detected in both full body cadaver test series as indicated by a previously determined acoustic biomarker (Eckersley 2020). Figure 6-3 and Figure 6-4 show example wavelet traces that are positive and negative for cavitation in the full body pig cadaver respectively. Mean time from impact to cavitation collapse (± SD) of the cadaveric pig tests was 1.1 (±0.3) ms.

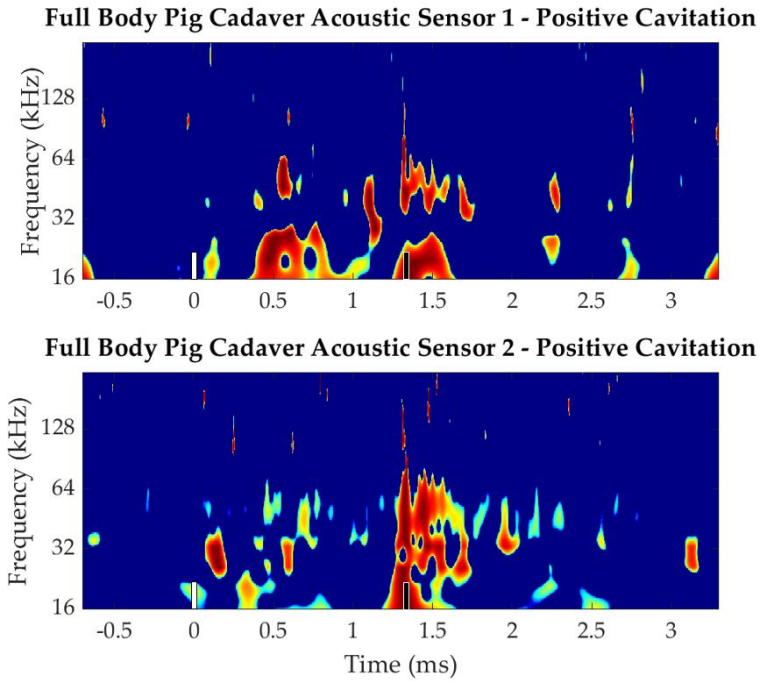

Figure 6-3: Example wavelet transform of positive cavitation in cadaveric pig, 242 g peak linear acceleration, collapse occurs 1.35 ms following impact. White bar along time axis indicates impact and black bar indicates cavitation collapse.

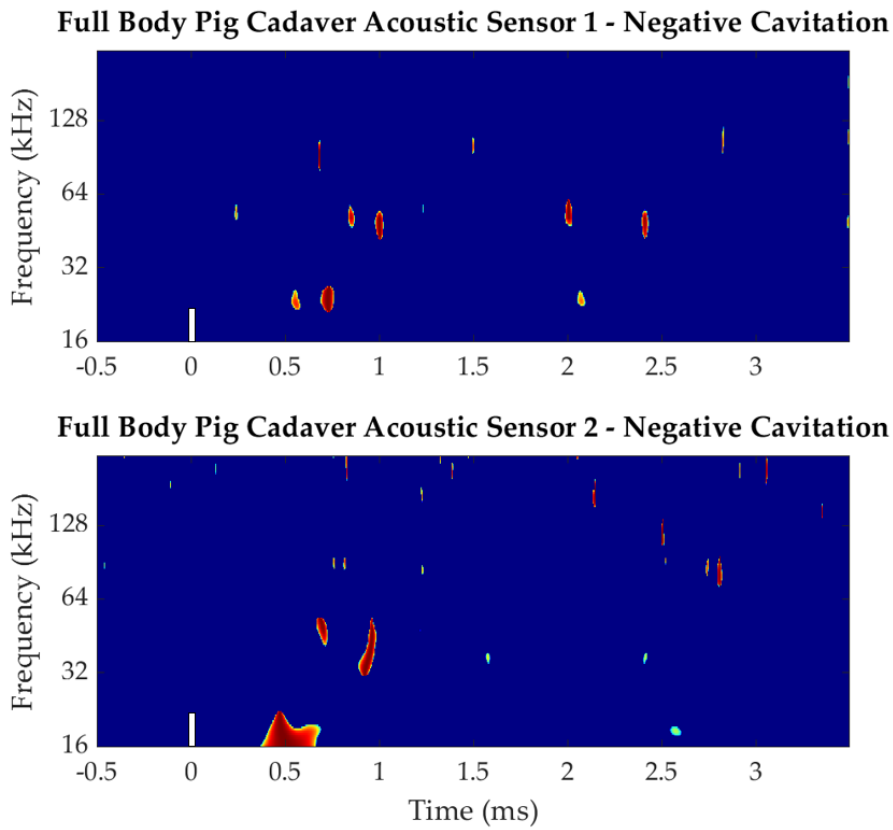

Figure 6-4: Example wavelet transform of negative cavitation from full body pig cadaver tests , peak linear acceleration 156 g, impact occurs at time = 0 (white line).

Figure 6-5 and Figure 6-6 show the wavelet transforms of the negative control, air filled and rigid polyurethane filled cranium tests. Peak linear accelerations were 237 g and 229 g respectively, and neither displayed the wideband acoustic biomarker within 3 ms of impact. Analysis of the microCT scans following testing did not indicate the presence of skeletal compromise meaning that acoustic responses are not the result of skull fracture. The results of the 40 kHz transmission test show 18.4 dB of damping by the cadaver head compared to the clear acrylic surrogate.

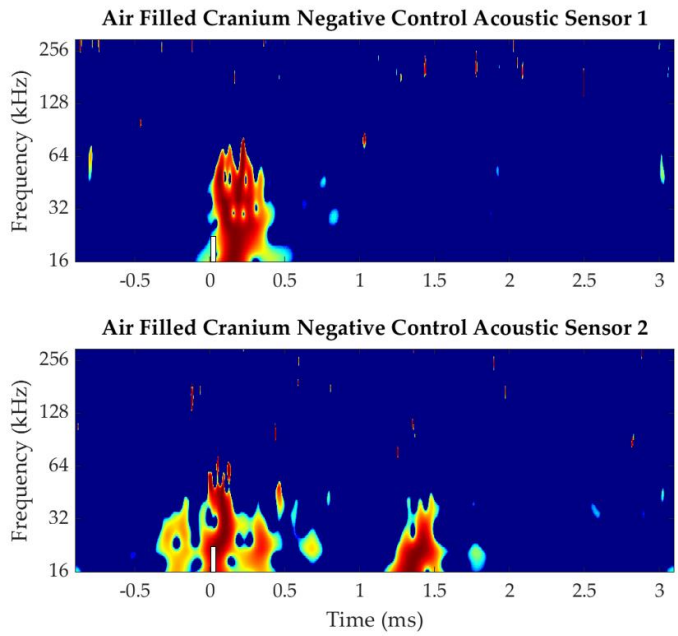

Figure 6-5: Wavelet transform of acoustic signal in an air filled cranium negative control test indicating structural acoustic response of blunt impact shows time/frequency response that is not characteristic of cavitation. Impact at time = 0, peak linear acceleration = 237 g.

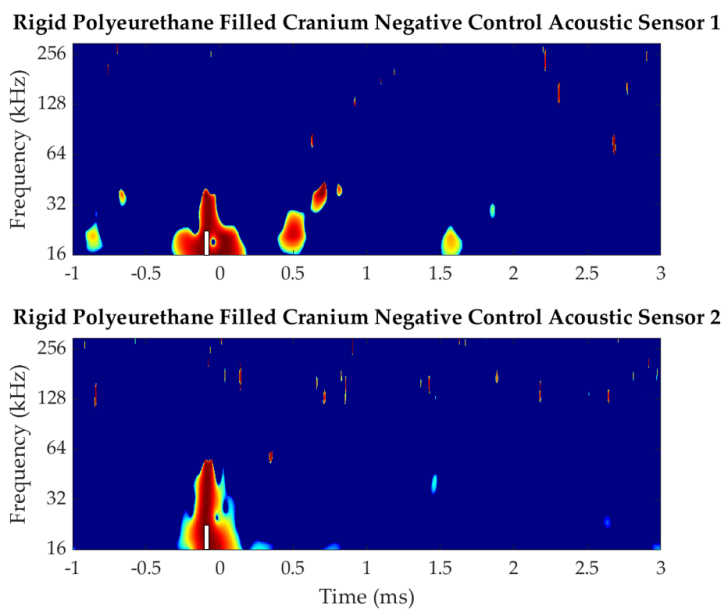

Figure 6-6: Wavelet transform of the acoustic signal in a rigid polyurethane filled cranium negative control test shows time/frequency response that is not characteristic of cavitation. Impact at time = -0.1 indicated by white marker, peak linear acceleration = 229 g.

The acoustic biomarker for transient cavitation collapse was detected in 34 of the 64 cadaver pig impact tests. Figure 6-7, Figure 6-8, Figure 6-9, and Figure 6-10 show the cavitation risk curves for the four calculated head injury metrics. HIC was the strongest predictor of cavitation formation with an Anderson-Darling (AD) score of 0.86 followed by angular acceleration with an AD score of 0.98. Linear acceleration was the third best predictor with an AD score of 1.01 and HIP was the worst predictor with an AD score of 3.84. Table 6-1 lists the 25%, 50%, and 75% risk of cavitation (95% CI) of each injury metric.

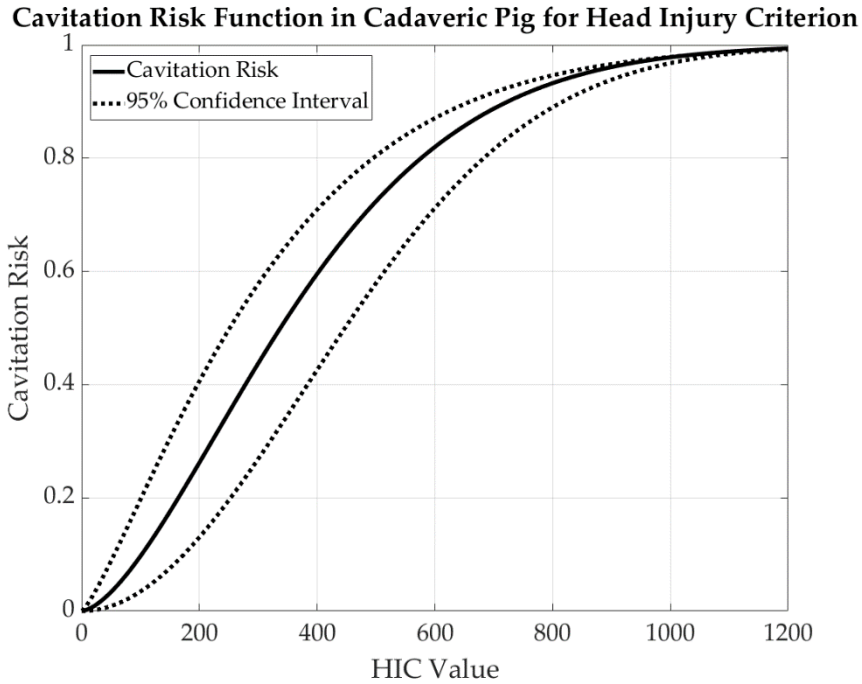

Figure 6-7: Cavitation risk plot of HIC for cadaveric pig repetitive impact test. 50% risk (95% CI) = 338 (264-432), Anderson-Darling score of 0.86.

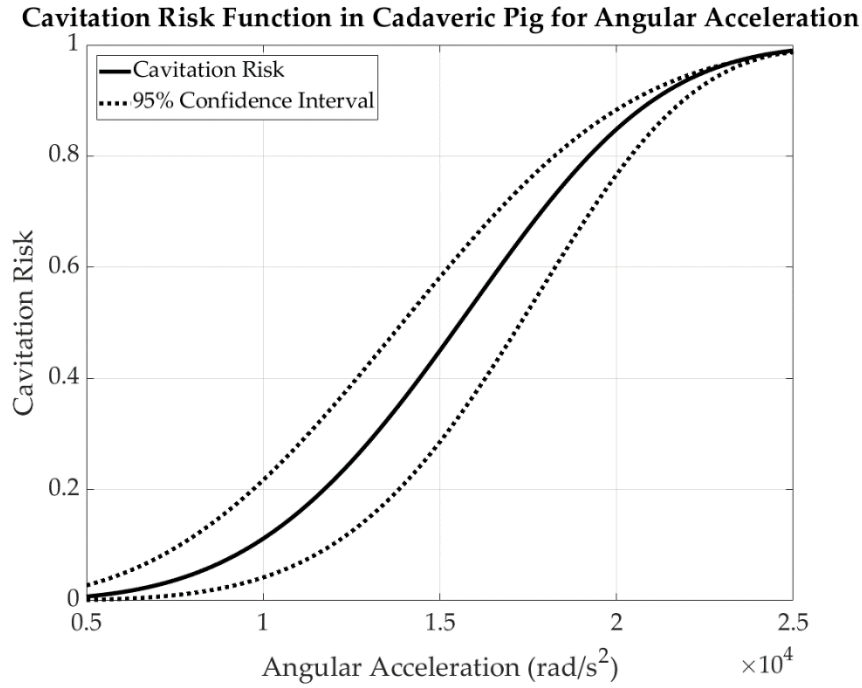

Figure 6-8: Cavitation risk plot of angular accel. for cadaveric pig repetitive impact test. 50% risk (95% CI) = 15567 (14220-17043), Anderson-Darling score of 0.98.

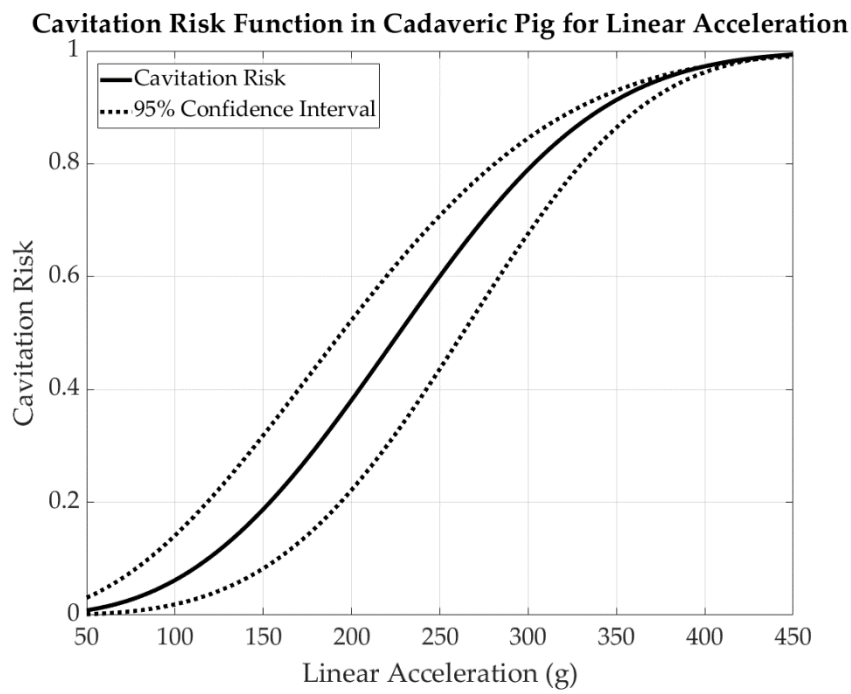

Figure 6-9: Cavitation risk plot of linear accel. for cadaveric pig repetitive impact test. 50% risk (95% CI) = 227 (199-259), Anderson-Darling score of 1.01.

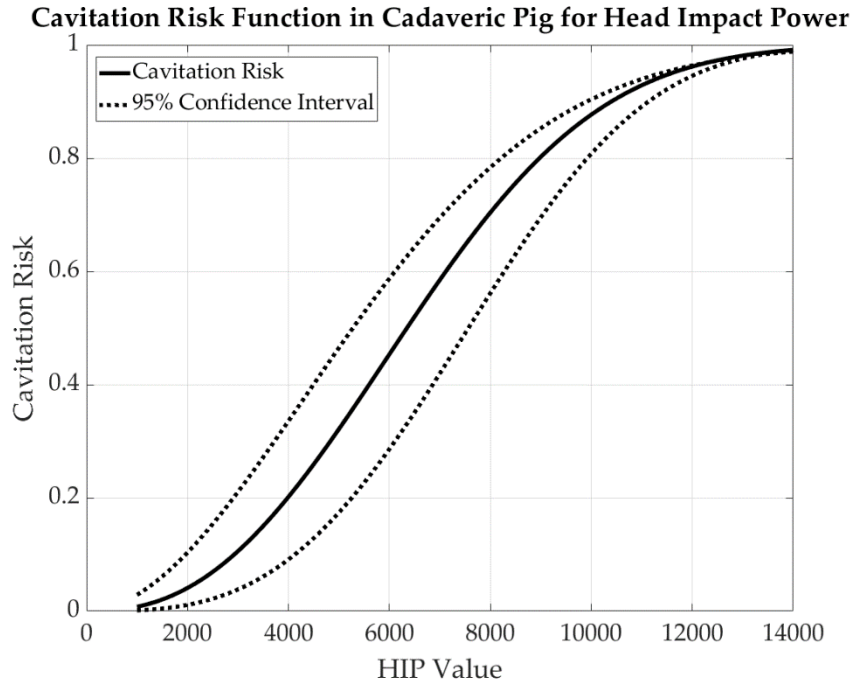

Figure 6-10: Cavitation risk plot of HIP for cadaveric pig repetitive impact test. 50% risk (95% CI) = 6347 (5461-7376), Anderson-Darling score of 3.84.

Table 6-1: Quartile Risks of Cavitation of Four Injury Metrics

Injury Metric	25% Risk (95% CI)	50% Risk (95% CI)	75% Risk (95% CI)
HIC	193 (140 – 266)	338 (264 – 432)	524 (252 – 435)
Angular Accel. (rad/s^2)	12493 (11074 – 14093)	15567 (14220 – 17043)	18516 (17008 – 20159)
Linear Accel. (m/s^2)	128 (141 – 200)	227 (199 – 259)	288 (256 – 323)
HIP	4421 (3630 – 5385)	6347 (5461 – 7376)	8439 (7306 – 9748)

6.3.2 Perfused Pig Cadaver to Investigate Clinical Implications of Cavitation

Figure 6-11 shows the wavelet transform from one of the perfused pig blunt impact tests and displays the acoustic biomarker developed for cavitation. This indicates cavitation can be induced in a model simulating pressurized vasculature. The injury

metrics that resulted in positive cavitation were: peak resultant linear acceleration – 286 g, HIC – 896, peak resultant angular acceleration – 16433 rad/s^2, and HIP – 5978.

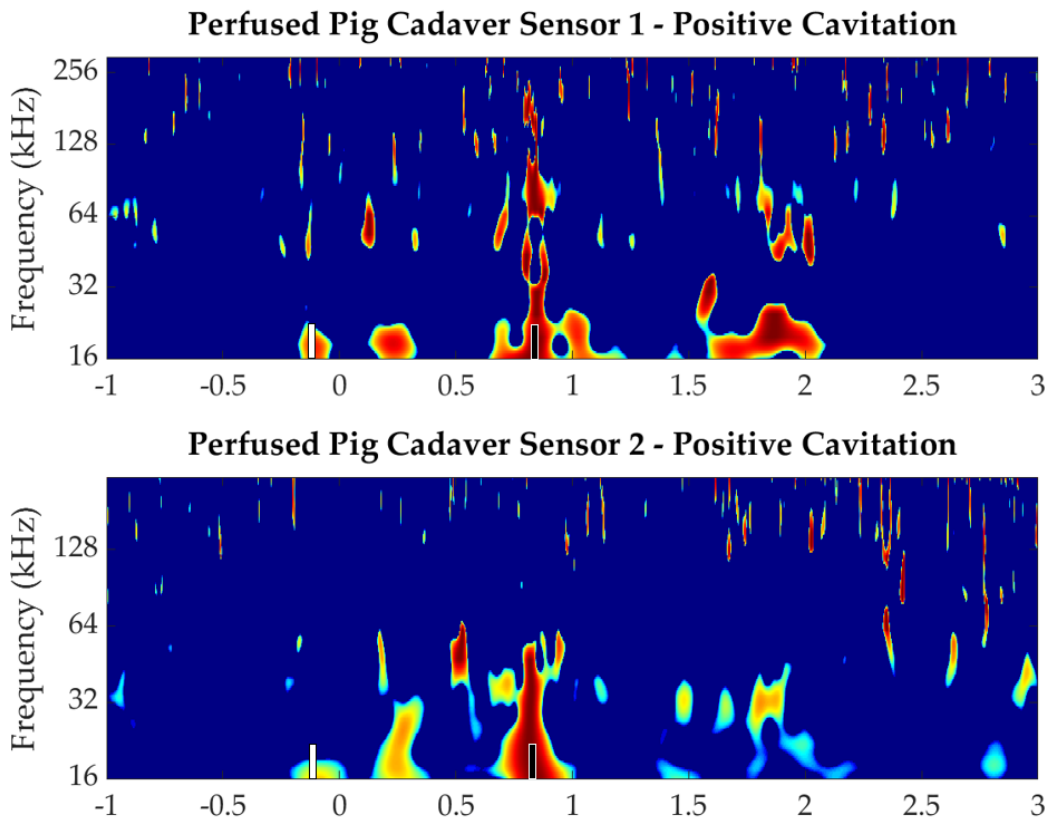

Figure 6-11: Wavelet transform of perfused pig head impact test showing acoustic biomarker positive for cavitation collapse. White mark indicates time of impact, black mark indicates time of collapse.

Figure 6-12 displays the wavelet transform from one of the perfused pig blunt impact tests that does not indicate the acoustic biomarker for cavitation collapse. The injury metric values for this impact were: peak resultant linear acceleration – 227 g, HIC – 613, peak resultant angular acceleration – 12125 rad/s^2, and HIP – 3898.

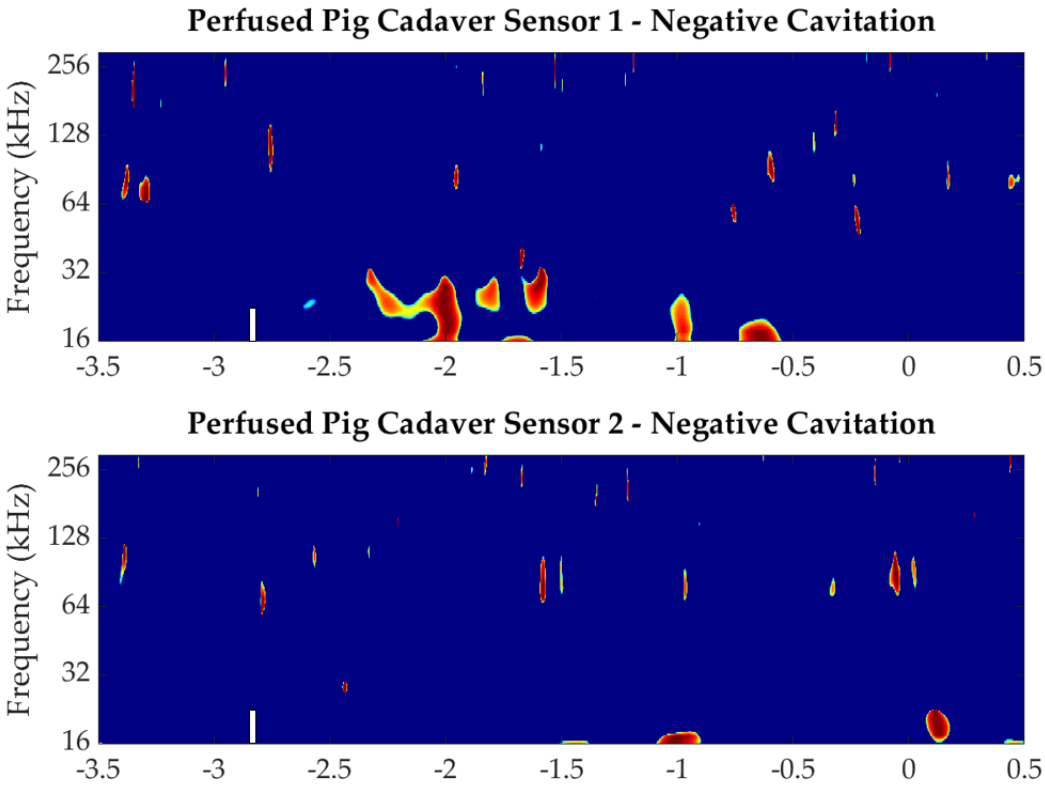

Figure 6-12: Wavelet transform of perfused pig head impact test that does not show acoustic biomarker of cavitation collapse. White mark indicates time of impact.

The full fixed brain of the positive cavitation impact described above is shown in Figure 6-13. Images of the whole brain show blue vasculature indicating successful perfusion of the saline and Evans blue solution. Close up images of the coup parenchyma indicate potential breaches in the blood brain barrier (Figure 6-14), images of the brain slices from both the positive and negative cavitation tests, do not show evidence of bleeding anywhere else in the brain (Figure 6-15).

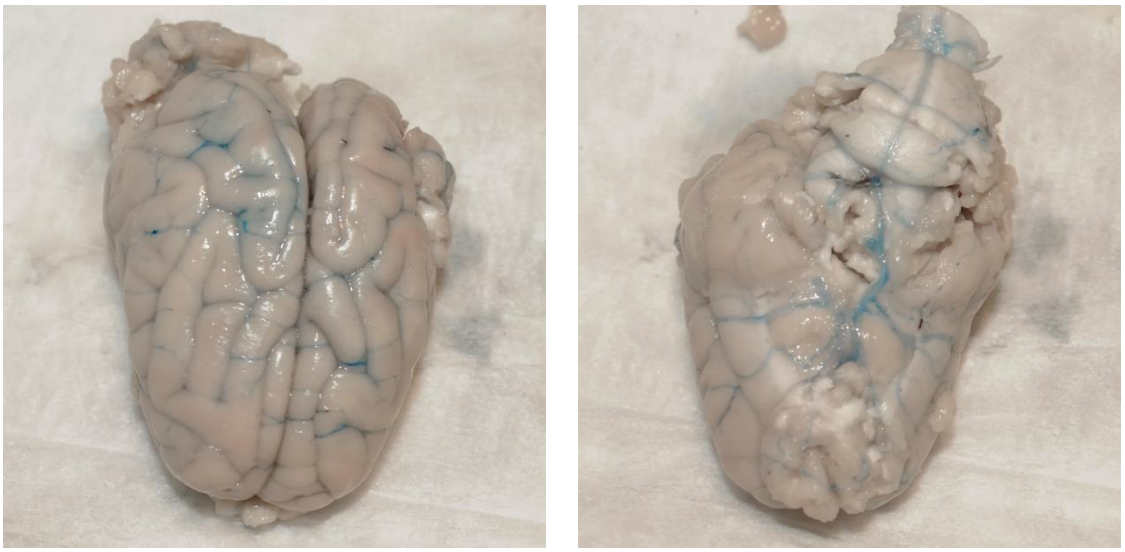

Figure 6-13: Superior (Left) and inferior (Right) images of the fixed pig cadaver brain following perfusion of Evans blue.

Figure 6-14: Close up images of the parenchyma on the impact coup for the positive (Left) and negative (Right) cavitation tests. Diffuse coloration indicative of breach in blood brain barrier.

Figure 6-15: Images of 5 mm brain slices for positive cavitation (Left) and negative cavitation (Right) tests. Achieved better perfusion in the positive cavitation tests as indicated by less blood.

6.4 Discussion

The principle goal of this study was to use the acoustic biomarker developed in Chapter 4 to inform the hypothesis that intracranial cavitation occurs in blunt impact scenarios and can be detected *in situ* of an uncompromised, full body pig cadaver skull. The acoustic biomarker was detected in high-level blunt impacts of the pig cadaver indicate that cavitation occurs in a biological tissue model and the biomarker can be detected through fresh cadaveric skull. A second goal of this work was to investigate

clinical implications of blunt impact cavitation. While direct clinical implications cannot be drawn from these tests due to limited sample size, single impact full body, perfused, pig cadaver tests provide a foundational methodology for observing clinical implications of cavitation through histological outcome.

In the blunt impact full body cadaver tests, numerous potential confounding events could be sources of the high frequency emissions observed. The first is noise in the acoustic sensor or a detachment from the skull. This is not the source of the emissions because in these tests, to be an indication of cavitation formation, the acoustic biomarker needed to be synchronized in time. If the emissions were a result of a sensor complication, the signal would be present on only one sensor and not the other. The second potential complication could be high frequency content from skull fracture or other bony fracture. However, cortical bone fracture has been shown to give acoustic emissions of much higher frequency (200–400 kHz) (Shridharani 2016) than what are seen in the acoustic emissions from these tests, indicating that this is not the source of these emissions. Furthermore, post-test microCT scans of the head do not show the presence of skull fracture. The emissions could also be from the lower jaw of the pig colliding with the upper jaw upon impact. This was prevented as a confounding variable by clinching the mouth shut with foam between the jaws. The final source of acoustic emissions could be from some flexure mode of the skull causing vibrations detected by the acoustic sensor. This was eliminated as a confounding source through the negative control test, which did not show the

acoustic emissions related to cavitation formation.

Based on the cavitation risk curves, HIC was the best predictor of cavitation out of the four calculated head injury metrics. This mirrors previous work investigating the role of container compliance in cavitation formation in Chapter 5. HIC was developed and validated to predict risk of skull fracture, an injury reliant on skull compliance. HIC being the best predictor of cavitation in this test series indicates container compliance is relevant for cavitation formation in ex-vivo surrogates and soft tissue. The 50% risk of cavitation value for HIC was 338. Unscaled, this value is below the 1% threshold of skull fracture in humans (Mertz 1996), indicating that it is plausible for transient cavitation to occur during blunt head impacts that are not catastrophic (Figure 6-16). Since the pig is slightly smaller than the average male, mass scaling will lower this value even further below the 1% skull fracture threshold. However, as discussed in Chapter 5, the traditional biomechanics scaling laws may not apply to incidence of cavitation because they do not account for variations in skull compliance.

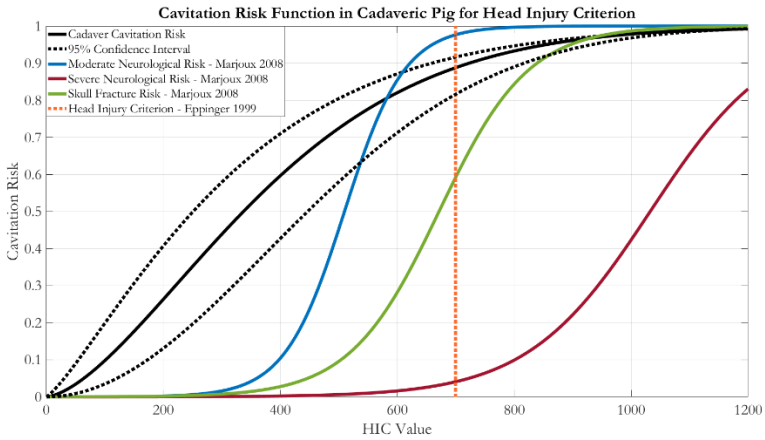

Figure 6-16: Cadaver HIC curve against previous head injury criteria.

Showing cavitation occurs under realistic blunt impact conditions indicates that many of the advanced metrics developed for traumatic brain injury do not capture the entire injury etiology. Current advancements in TBI rely heavily on finite element models to determine peak brain strain based on kinematic inputs. However, these models do not account for cavitation, and will not capture localized deformations due to transient cavitation collapse. In addition to vast biological variance, this may explain why currently, no conclusive and comprehensive TBI injury criterion has been developed.

Since it is difficult to observe high rate phenomenon such as cavitation through the skull, appropriately constructed finite element (FE) models and numerical analysis are valuable tools for cavitation analysis. FE models, in general, are ineffective without an accurate value for the CSF cavitation threshold pressure. Numerous studies have aimed to tackle this problem through various experimental methods, determining answers from -100 kPa to -20 MPa (Herbert 2006, Takhounts 2008, Singh 2015, Salzar 2017). This variation is primarily due to the effect of nucleation sites, both in the amount of dissolved gasses in the fluid and imperfections on the surface of the containment vessel. It is difficult to control and ensure the biofidelity of these variables. Because of this, the incidence of cavitation in these modeling studies is often unreliable. This study used a novel method of cavitation detection, which did not rely on controlling these variables, and ensured the cranial cavity was not compromised prior to testing, providing reliable evidence for the incidence of intracranial CSF cavitation.

Previous work on soft tissue cavitation in areas of the body other than the head use ultrasound frequencies (1-3 MHz) to detect the incidence of cavitation (Coleman 1996, Pishchalnikov 2003, Li 2019). As shown in this study, acoustic damping across the skull can be nearly 18.5 dB for 40 kHz frequency in comparison to non-biological acrylic. Literature reports 1 – 3 MHz frequencies can be dampened by up to 30 dB across the skull (Fry 1978). Signal power emitted in the 1 – 3 MHz frequency range will be limited by bubble size in the CSF space. Acoustic damping from the skull combine with the low signal power make it difficult to differentiate high frequency signals from noise across the skull. For one of the positive cavitation repetitive impacts, the skull was also instrumented with a high frequency acoustic sensor (300 – 1800 kHz flat frequency) filtered from 500 – 2000 kHz. Figure 6-17 compares the wavelet transform of the signal from this sensor to that of the one used for cavitation detection. This illustrates cavitation collapse is detected by sensors of low frequency content, but signal from higher frequency sensors is indiscernible from noise.

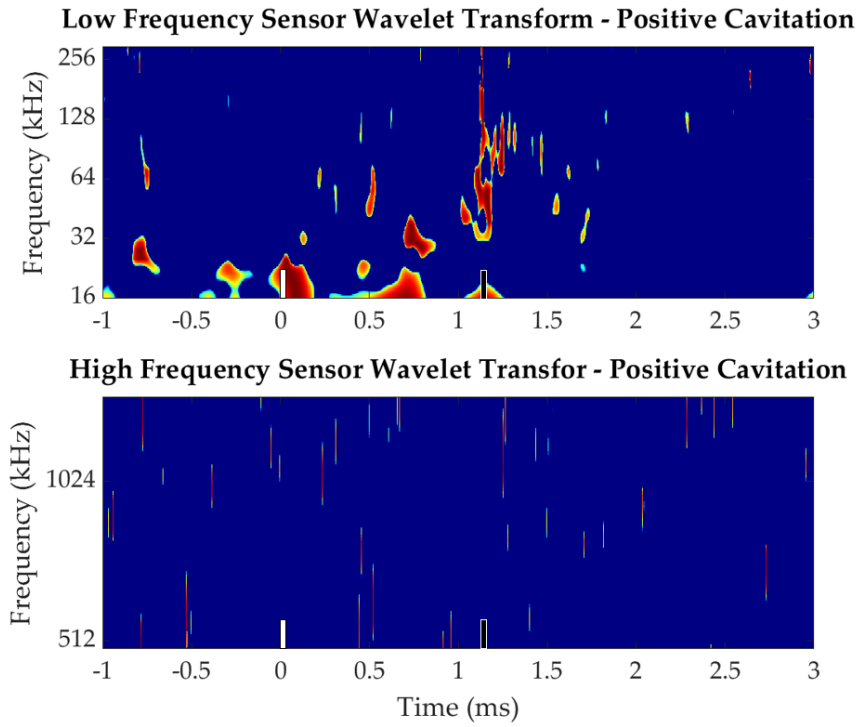

Figure 6-17: Comparison of wavelet transforms between high and low frequency sensors from positive cavitation pig cadaver blunt impact test showing cavitation collapse (black mark) is not detected in high frequency sensor due to acoustic damping of the skull.

Comparing the cavitation risk curves of the full body pig cadavers to the membrane acrylic surrogate cavitation risk curves developed in Chapter 5 show the 50% risk of cavitation of the pig cadavers is statistically significantly lower for HIC and higher for Angular Acceleration and HIP (the 95% confidence intervals do not overlap). It is expected that angular acceleration and HIP would be different between the two because they are such poor predictors of cavitation in the surrogate tests. In addition, since the angular acceleration inputs are higher in the pig tests due to increased geometric complexity, HIP will follow as being higher because the two are correlated. However, the increased angular accelerations will create increased linear accelerations at locations

translated away from the CG. This explains why the HIC value required for cavitation is lower in the pig model even though the compliance in the two systems is similar; a lower CG linear acceleration is required to still reach the cavitation threshold in the CSF layer.

Because of the limited sample size, the primary goal of the perfused pig tests was to serve as a sub-study that lays the foundation for continued investigation of the clinical implications of cavitation. This work displays three important results. First, the successful perfusion of the Evans blue dye throughout the entire cerebral vasculature. This indicates that the vasculature was successfully drained of blood during the saline perfusion and Evans blue will locally, regionally, and globally perfuse the vasculature to indicate damage. Next, breaches in the blood brain barrier may be indicated by diffuse coloration of the Evans blue in neurological tissue, as both impacts indicate blood brain barrier disruption on the coup (Figure 6-14). Finally, cavitation is still observed with the biofidelic experimental addition of a pressurized vasculature. This provides additional evidence that transient cavitation may occur in a soft tissue cranial model under blunt impact loading and this methodology can be successfully deployed to study the clinical implications of blunt impact transient cavitation. While this work is unable to draw direct clinical implications of cavitation, previous work indicates cavitation collapse can damage neurological and vascular soft tissue (Canchi 2017). This provides further motivation that the clinical implications of cavitation should be investigated using this methodology.

A number of limitations are present within this study. First, the blunt impacts were not controlled to simulate a particular blunt impact event. The goal of this study was to show the plausibility of cavitation formation during a blunt impact event, but not in any event in particular (such as a helmeted collision or head hitting A-post in car accident). Second, while the impact tests were conducted using a fresh cadaver (~3–5 hr post-mortem), the brain tissue may have begun to deteriorate and the CSF layer may have been altered compared to a live animal. However, lower level controls following high impacts in the repeated tests and brain dissection following the perfusion tests indicate deterioration did not occur. Third, because container compliance plays such a large role, a scaling metric between the pigs and humans would need to consider skull stiffness, geometry, and size. Since these values are different between humans and the pig model, it is difficult to translate cavitation detection to humans using a scaling principal. Fourth, the conclusions on clinical implications of cavitation from the perfused head tests are limited by the sample size collected. Future work will continue the investigation to provide additional insight to the clinical applications of cavitation.

6.5 Conclusions

This work used the acoustic biomarker developed in Chapter 4 to investigate blunt impact cavitation in a fresh, non-frozen, full body pig cadaver model. This is the first investigation of blunt impact CSF cavitation in an uncompromised soft tissue model. The data show that intracranial soft tissue cavitation occurs at impact levels below those

expected for catastrophic injury such as open skull fracture, DAI, or massive hemorrhaging. Results of this work also imply the wideband acoustic signature of cavitation collapse can most easily be detected in the range of 20 – 250 kHz due to acoustic attenuation of high frequency content by the skull. This study is the first that uses a fresh, non-frozen uncompromised pig head model to show blunt impact CSF cavitation may occur under physiological impact loads. The evidence provides strong motivation that future work should be conducted to further understand the clinical TBI implications of blunt impact cavitation. The final portion of this work provides a methodology that can serve as a framework for study of clinical TBI implications of blunt impact cavitation.

7. Clinical Implications of Cavitation in the Human Population

7.1 Objectives

Because blunt impact transient cavitation is theorized to occur in the CSF space, clinical implications focus on contusions of the external cortex and rupture of bridging vessels spanning the subdural and subarachnoid space. Intracranial contusions and ruptured bridging vessels can result in life threatening bleeding (Gennarelli 1971, Gennarelli 1982), increased ICP levels, and are readily detected on non-invasive CT or MRI scans. Owing to straight forward noninvasive identification and important clinical implications, numerous literature sources have investigated the mechanism of these intracranial injuries in both experimental models and retrospective epidemiology.

Current theory suggests three mechanisms for intracranial damage: skull intrusion under the impact site, cavitation, and shearing from angular acceleration. Each mechanism will provide a particular hypothesized injury pattern. Tissue damage from skull intrusion will manifest as coup injuries directly under the impact site. Cavitation formation is consistently observed on the impact contre-coup in surrogate tests where the inertial pressure gradient and wall compliance create localized negative pressure (Nusholtz 1995, Eckersley 2020, Van Orman 2020). Therefore, cavitation induced injuries will also manifest on the impact contre-coup site. Based on the work of Gennarelli *et al.* and Ommaya *et al.*, vessel shearing from angular acceleration will manifest itself at

locations of peak tissue strain. (Gennarelli 1971, Ommaya 1971, Gennarelli 1972, Gennarelli 1982). These locations are dependent on geometry and acceleration direction.

While conducting live animal testing is beyond the scope of this work, it is hypothesized reanalysis of seminal live subhuman primate testing from the 1960s-1980s with novel tools and insight from this dissertation will provide new evidence to the mechanisms of intracranial bleeding (in the context of the experimental dynamic, potentially injurious, exposures). Additionally, it is hypothesized retrospective analysis of human intracranial bleeding cases will provide evidence that the trends of subhuman primate testing will translate to clinical implications for cavitation in humans.

7.2 Methods

7.2.1 Methodology of Live Animal Tests in Literature Investigating Intracranial Bleeding

A series of seminal papers conducted from 1960-1980 utilized live subhuman primate testing and prevailing mechanical theories of the time to draw conclusions on the mechanisms of brain contusions and bleeding (Table 7-1). This previous seminal literature provides a valuable resource of recorded kinematic data and correlated neuropathological analysis that, when combined with previous work in this dissertation and novel investigative tools, can provide novel insight to the mechanisms of these potentially catastrophic injuries.

Table 7-1: Summary of Live Animal Testing Investigating Intracranial Bleeding

Author	Year	Species	Number	Direction
Ommaya	1968	Rhesus Monkeys	50	Sagittal Inertial Loading
Ommaya	1971	Rhesus Monkeys	67	Sagittal Impact Frontal and Occipital
Gennarelli	1972	Squirrel Monkeys	25	Sagittal Helmeted Loading, Minimal Impact
Gennarelli	1979	Rhesus Monkeys	30	Sagittal Helmeted Loading, Minimal Impact
Ono	1980	Multiple	63	Sagittal Frontal and Occipital Impacts, Helmeted and Un-Helmeted

7.2.1.1 Ommaya *et al.* - 1968

In this study, 50 rhesus monkeys were positioned in a cart that was allowed to move freely down a linear track (Ommaya 1968). The cart was rapidly accelerated forward using a pneumatic piston, simulating a rear end vehicle collision. By pushing the cart, this study provided inertial loading to the head that resulted in high angular accelerations without an impact (Figure 7-1). Following the acceleration event, brains were dissected from the skull to observe macroscopic pathology.

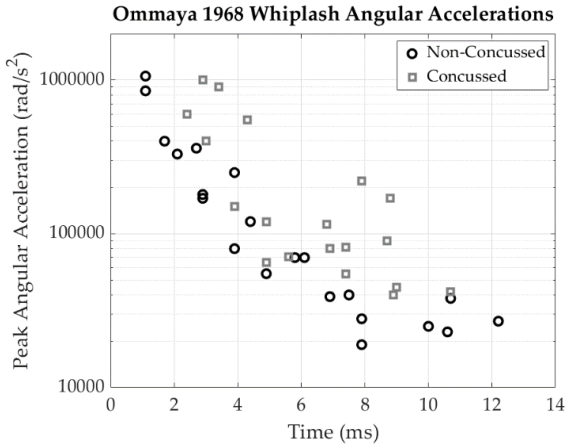

Figure 7-1: Peak angular acceleration and duration of 40 impact tests (Ommaya 1968)

7.2.1.2 Ommaya *et al.* - 1971

This study consisted of 67 head impact tests on adult rhesus monkeys (42 impacts to the midoccipital region and 25 to the mid frontal region) with the goal of a midsagittal axis of symmetry (Ommaya 1971). Impacts were delivered approximately through the head center of gravity (Figure 7-2) using an explosive cartridge that applied 3500 – 4000 N of force over 2 – 4 ms. This resulted in tangential skeletal linear velocities of 12 – 16 m/s and angular velocities of 150 – 250 rad/s. To limit the number of skull fractures from frontal impacts, a plate was positioned over the forehead and face to provide a path of load distribution away from facial structures. Four hours after impact, the specimens were sacrificed and the brains were dissected to investigate macroscopic damage.

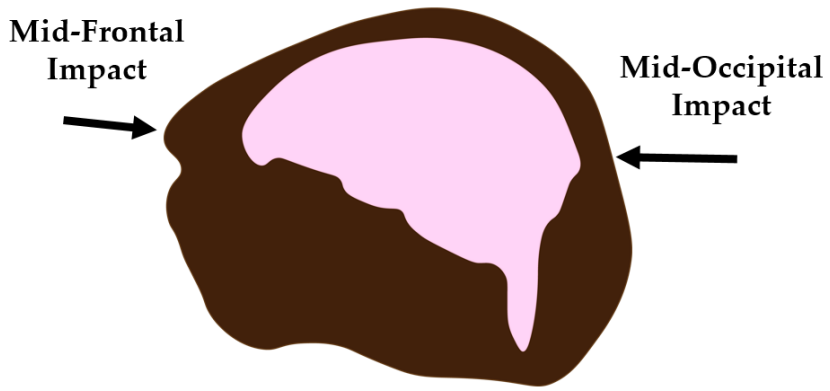

Figure 7-2: Frontal and occipital impact sites directed approximately through the head center of gravity (Ommaya 1971)

7.2.1.3 Gennarelli *et al.* - 1972

This test series consisted of 25 squirrel monkey acceleration tests (Gennarelli 1972). Each monkey was rigidly fastened to a helmet that was linked to a pneumatic device

capable of delivering precise linear and angular accelerations through the sagittal plane. Of the 25 tests, 12 provided a predominantly linear translation of the head while 13 generated a combined linear translation and angular rotation. The resulting head accelerations were measured using high-speed video and are listed in Table 7-2. Following impact, the specimens were sacrificed and the brains were dissected for analysis of macroscopic damage.

Table 7-2: Summary of Acceleration Magnitudes (Gennarelli 1972)

Test Type	Peak Linear Acceleration (g)	Peak Angular Acceleration (rad/s^2)	Duration (ms)
Linear	1230	NA	6
Linear	1140	NA	6.5
Linear	1058	NA	7.0
Linear	854	NA	7.0
Linear	830	NA	6.5
Linear	812	NA	7.0
Linear	802	NA	7.5
Linear	768	NA	6.5
Linear	734	NA	8.0
Linear	665	NA	7.5
Combined	1025	317,000	6.5
Combined	1025	317,000	5.5
Combined	961	297,000	7.0
Combined	783	242,000	7.0
Combined	728	225,000	7.0
Combined	713	220,000	7.0
Combined	710	219,000	7.0
Combined	706	218,000	7.0
Combined	700	216,000	7.0
Combined	488	151,000	7.5
Combined	402	124,000	7.5
Combined	387	120,000	8.0
Combined	348	108,000	7.5

7.2.1.4 Gennarelli *et al.* - 1979

For this study, 30 rhesus monkeys were tested using a pneumatic linkage system that rotates a helmet fixed to the animals head through the sagittal plane without a direct impact (Gennarelli 1979). Angular accelerations about the head center of gravity were between 18,000 and 120,000 rad/sec^2, and tangential linear accelerations of the head CG were between 190 and 1500 g. Following testing, animals were sacrificed immediately or after 1 week, and brains were dissected and analyzed for macroscopic damage.

7.2.1.5 Ono *et al.* - 1980

This investigation used 63 monkeys of various species (Japanese monkey, rhesus monkey, crab eating monkey, and baboon) to investigate the role of kinematic input (angular vs. linear) and impact surface area (distributed vs. focal) on brain bleed injuries and skull fractures (Ono 1980). Each test used a pneumatic impactor that impacts either the head of the monkeys or a force distributing mask. Impacts were applied from a heavy mass to both the frontal and occipital region at velocities from 5 – 28 m/s. Measured linear accelerations of the head ranged from 240 – 1,100 g, angular accelerations ranged from 6,000 to 250,000 rad/sec^2, and durations were between 2 and 18 ms. Monkeys that survived experimentation were sacrificed 18 hrs. to 1 week following impact and the brains were fixed and dissected for macroscopic damage analysis.

7.2.2 Finite Element Modeling of Past Experimental Conditions

Over the course of nearly 50 years, novel tools have been introduced that provide additional insight to the results determined in these seminal articles, one being finite element (FE) modeling. While material models in FE modeling limit the absolute quantitative measures modeling can provide (Eckersley 2020), it is valuable to investigate the role of geometry in relative pressure and strain distributions within the head. For this study the SIMon model was used (Takhounts 2003). The SIMon head model was developed for open access use by the National Highway Traffic Safety Administration to asses head injury in car accidents. The model consists of anatomically representative cerebellum, cerebrum, CSF-dura layer, ventricles, brainstem, falx, foramen magnum, bridging vessels, and skull. It represents a 50th percentile male modeled with a rigid skull and soft tie-break interface for the skull to CSF-dura and CSF-dura to brain interaction.

Using LS-Prepost and LS-DYNA, rigid skull kinematics were prescribed to the SIMon model based on the range of sagittal impacts from previously described live animal testing. Angular and linear accelerations of 66,666 rad/s^2 and 475 g are applied to the head over the duration of 0.003 s. Nine separate simulations were applied, summarized in Table 7-3. Element pressure and effective strain in the model were output at 20 kHz.

Table 7-3: Summary of SIMon Model Impact Conditions

Direction of Impact	Linear Accel. Applied?	Angular Accel. Applied?
Occipital	Yes	No
Occipital	No	Yes
Occipital	Yes	Yes
Frontal	Yes	No
Frontal	No	Yes
Frontal	Yes	Yes
Lateral	Yes	Yes
Lateral	Yes	No
Lateral	No	Yes

7.2.3 Retrospective Study of Brain Bleed Cases

Access to patient files at the Duke Hospital was obtained through the Duke Health IRB under protocol ID Pro00102614. A filter pulled CT scan radiology notes on patients with subdural hematoma from the years 2013 – 2019. Files were sorted by the patient's medical record number (MRN), and only files with novel MRNs were recorded to prevent duplicate records from multiple scans on the same patient. Patients with preexisting conditions relevant to subdural hematomas (chronic subdural, craniotomies, burr holes from previous surgery, cancer) as well as patients with open head wounds were excluded from analysis. Finally, only cases where the location of the subdural bleed and impact evidence are noted by the radiologist are recorded. This eliminates files from patients who developed subdural hematomas from non-impact events. For each file, I noted the location of the subdural hematoma, and the location of external indications of injury (lacerations, subgleal hematomas, scalp hematomas).

Based on the results of the finite element simulations, each case was sorted based on the relation of injury and impact site. Cases were designated as injury under the impact site, a bleed at a location of expected peak strain, or a bleed at an unexpected location.

7.3 Results

7.3.1 Results of Live Animal Tests in Literature

7.3.1.1 Ommaya *et al.* - 1968

Of the 50 tests conducted, 19 of the specimens were determined to have a concussion and 15 of those displayed macroscopic damage in the form of surface hemorrhages, primarily subdural (Ommaya 1968). The primary locations are illustrated in Figure 7-3 and consist of parietal parasagittal zones, medial supra callosal surfaces, frontal temporal lobes, temporo-occipital cerebral surfaces, and the brainstem.

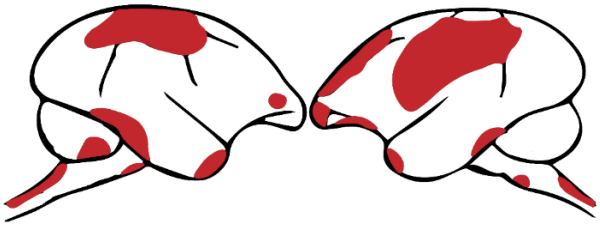

Sagittal View of Bleeding Locations

Ventral (Left) and Dorsal (Right) Surface Bleeding Locations

Figure 7-3: Illustration based on Ommaya *et al.* of the combined bleeding locations of all 15 tests that resulted in macroscopic damage (Ommaya 1968). Of note are the temporo-occipital surfaces and parietal parasagittal zones.

7.3.1.2 Ommaya *et al.* - 1971

Of the 42 occipital impacts, 22 showed macroscopic evidence of bleeding without skull fracture while 10 saw fracture of the occipital bone (Ommaya 1971). A majority of the lesions associated with occipital impact without fracture are contre-coup and seen in the frontal and temporal lobes (Figure 7-4). In the tests where fracture was present, coup lesions were the predominant injury seen. In the 25 frontal impacts, very few lesions were seen in the absence of skull fracture, except for one set of bilateral lesions on the upper medulla oblongata. Additional analysis found that while subdural hematomas were more difficult to produce than contusions, they were often associated with the frontal location of the brain, and not necessarily sub adjacent to impact sites.

Figure 7-4: Lateral (left), ventral (center), and dorsal (right) illustrations of cumulative contusion and bleeding locations of the 22 occipital tests without fracture based on Ommaya *et al.* (*Ommaya 1971*). Of note, majority of injuries localized to ventral frontal and temporal lobes, little bleeding in the parasagittal region.

This paper also reported on the results of a study using a two dimensional gelatin phantom to observe geometric stress concentrations in a sagittal brain rotation with the aid of a polariscope. These results are illustrated in Figure 7-5 where darker spots indicate

locations of higher stress. The highest stress concentrations are in both the parasagittal region and frontal poles.

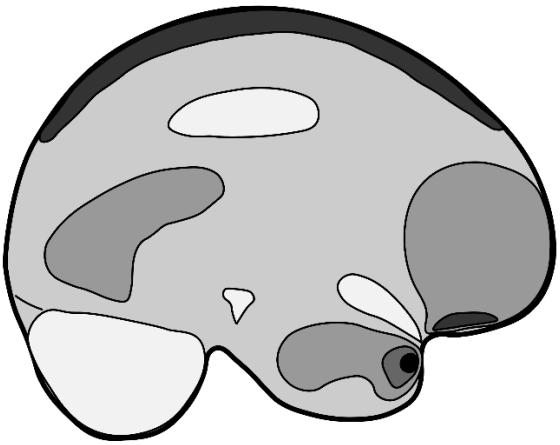

Figure 7-5: Results of a study investigating stress concentrations due to rotation in the sagittal plane based on Ommaya *et al. (Ommaya 1971)*. Highest concentration stresses are in both the parasagittal region and frontal poles.

7.3.1.3 Gennarelli *et al.* - 1972

Specimens that experienced primarily linear accelerations experienced fewer and less obvious lesions than the specimens that experienced additional rotational acceleration (Gennarelli 1972). Of the animals that experienced only linear acceleration at the CG, subdural blood was seen in only eight of the cases and the anterior 5 mm of the front pole was affected. With the addition of rotational acceleration at the CG, 20 specimens experienced subdural blood. These cases were more severe covering both entire frontal lobes, and in some instances found on the temporal pole. Bleeding was more prevalent in the parasagittal region than the lateral region. Contusions in this study were considered hemorrhagic lesions that reveal disruption of cortical structure. The contusions were seen

in both sets of experiments, but were more prominent in tests with only linear acceleration of the CG. As in the previous studies, the contusions were found in the mid frontal region away from the midline. Contusions were often small (2-4 mm), circular or oval in shape, and surrounded by a halo of bleeding. Additionally, the contusions resulted in a conical shape of damage into the cortical tissue.

7.3.1.4 Gennarelli *et al.* - 1979

Thirty of the specimens in this test displayed contusions: nine with both frontal and temporal contusions, eight with only frontal contusions, and thirteen with neither frontal nor temporal contusions (Gennarelli 1979). When they appeared, frontal contusions were located on either the inferior or antero-dorsal surface while temporal contusions were found at the tip; similar to the contusions of Ommaya 1971 (Ommaya 1971). The kinetic inputs required to generate both temporal and frontal contusions were statistically significantly larger than those required to create frontal contusions only.

7.3.1.5 Ono *et al.* - 1980

This study analyzed three separate groups, Group A: severe impacts using a mask to distribute impact load and limiting head motion to linear acceleration, Group B: severe impacts using a mask to distribute impact load and allowing rotational head motion, and Group C: moderate impacts with no mask to distribute load and allowing rotational head motion (Ono 1980). Of the 26 monkeys tested in Group A, only slight subarachnoid hemorrhages were seen with no other intracranial bleeds or contusions. In Group B: 12

tests did not result in fracture, and seven showed contusions and or subarachnoid hemorrhage. These were located in three primary regions: the parasagittal region, the basal surface and tips of the frontal and temporal lobes, and brain stem. In Group C, the impacts were considered mild, but the 18 subjects experienced multiple impacts. Pathological analysis did not find any bleeding or contusions present in the parasagittal region, but contusions were present on the inferior surface and ellipse of the frontal lobe and the tip of the temporal lobe.

7.3.2 Finite Element Modeling Results

Peak pressure and effective strain plots of the combined acceleration occipital, frontal, and lateral tests are found below (Figure 7-6, Figure 7-7, Figure 7-8, Figure 7-9, Figure 7-10, and Figure 7-11). The distribution patterns of the only linear and only angular inputs are similar to the combined loading distributions. There are several key takeaways. Peak negative pressures occur on the at the poles and inferior surface of the frontal and temporal lobes in an occipital impact, and near the base of the occipital lobes and superior portion of the cerebellum in frontal impacts. The peak negative pressure for the same kinematic input is 200 kPa more negative during an occipital impact than a frontal impact. Peak effective strains are seen primarily in the parasagittal region, brain stem, and frontal/occipital convexities for both frontal and occipital impacts. For lateral impacts, peak negative pressure and strain are seen in similar locations on the contre-coup. Finally,

for all impact types, peak negative pressures occur sooner and over a shorter displacement than peak strain values.

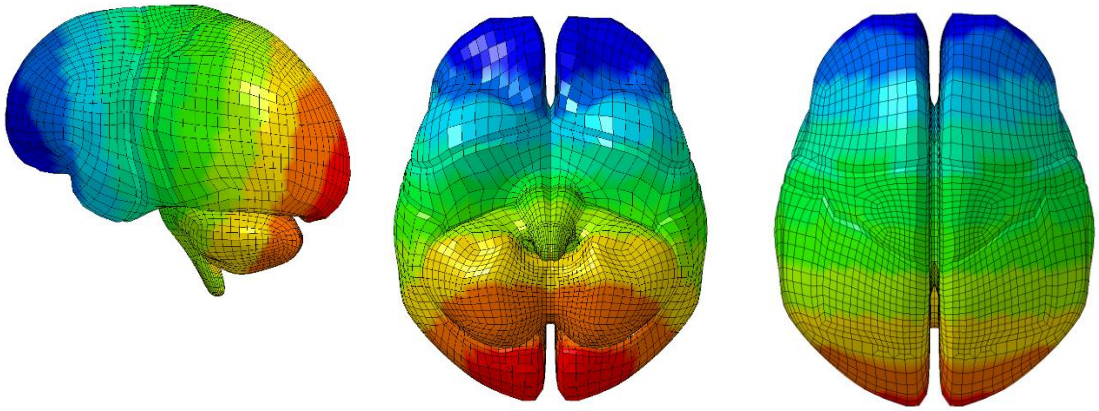

Figure 7-6: Peak pressure distribution from an occipital impact , blue indicates negative pressure while red indicates positive pressure. Peak negative pressures occur on the inferior surface of the frontal and temporal lobes.

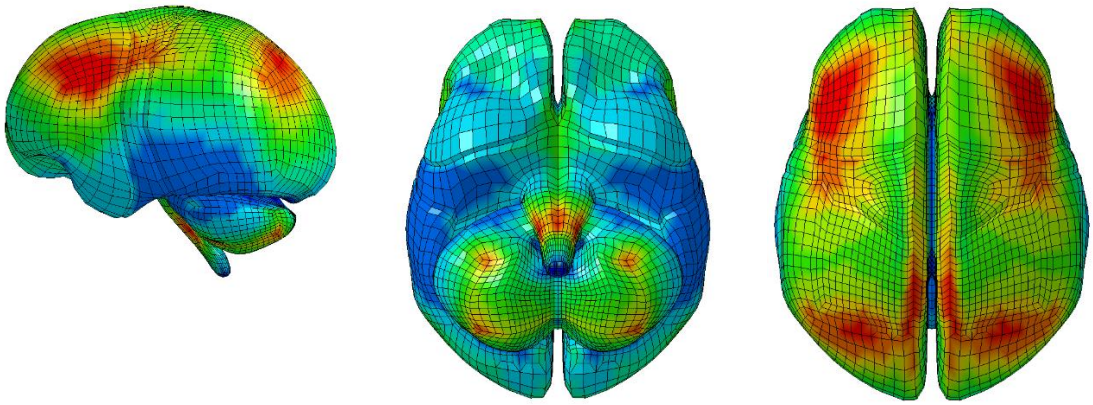

Figure 7-7: Peak strain distribution from an occipital impact , red indicates locations of highest strain. Peak surface strains occur in the parasagittal region as well as frontal and occipital convexities.

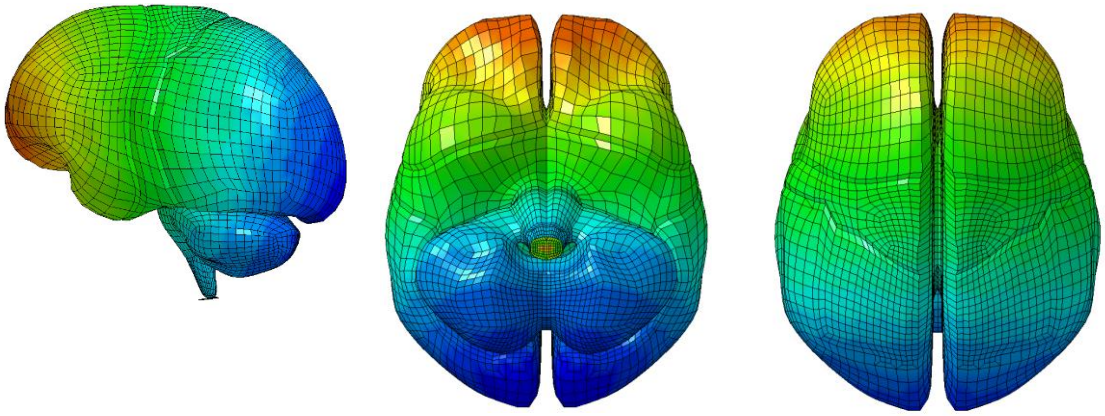

Figure 7-8: Peak pressure distribution from a frontal impact , blue indicates negative pressure while red indicates positive pressure. Peak negative pressures occur on the surface of the occipital lobes and superior cerebellum.

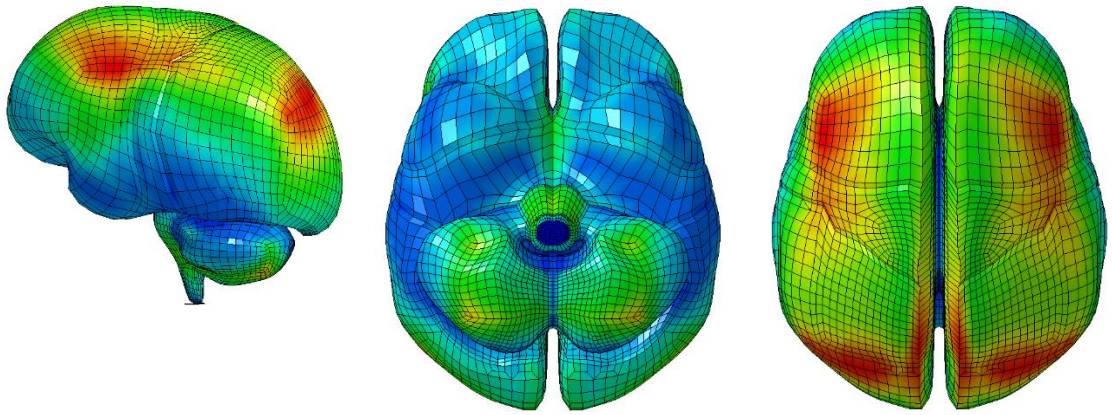

Figure 7-9: Peak strain distribution from a frontal impact , red indicates locations of highest strain. Peak surface strains occur in the parasagittal region as well as frontal and occipital convexities.

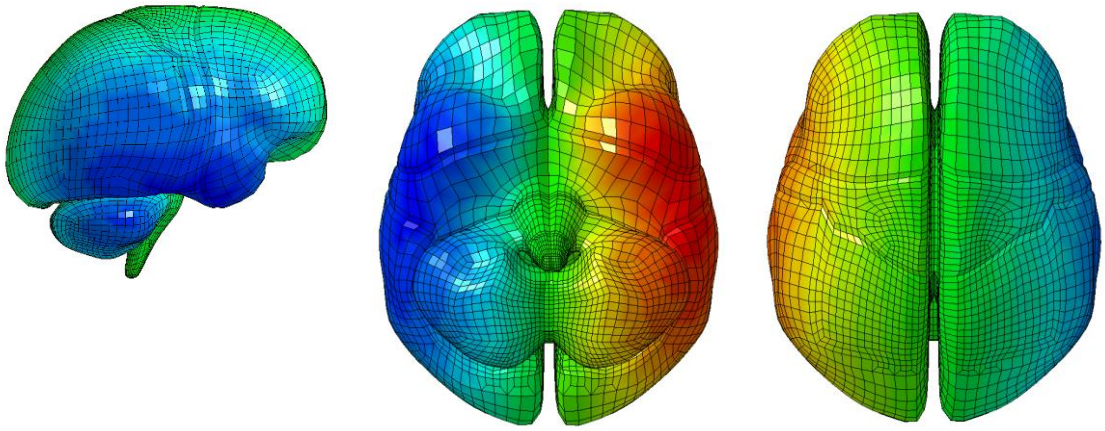

Figure 7-10: Peak pressure distribution from a lateral impact , blue indicates negative pressure while red indicates positive pressure. Peak negative pressures occur on the contre-coup lateral temporal and occipital lobes.

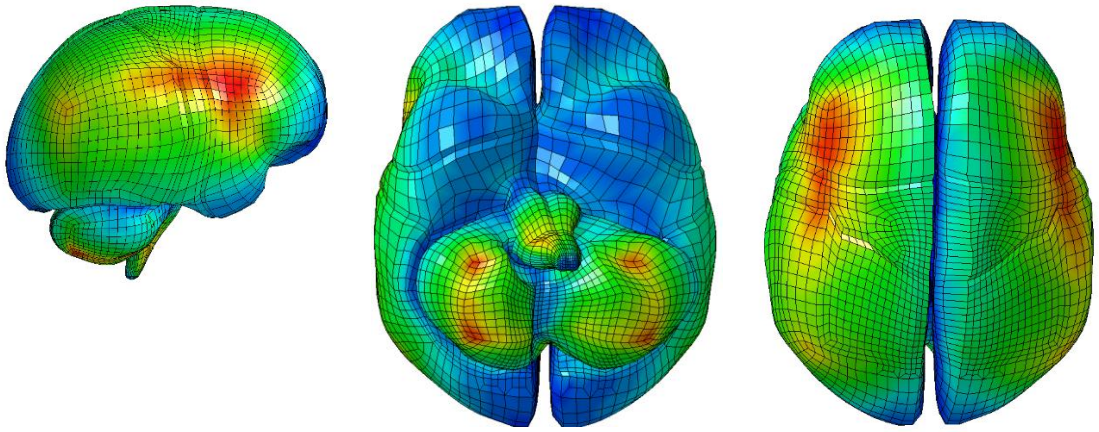

Figure 7-11: Peak strain distribution from a lateral impact , red indicates locations of highest strain. Peak surface strains occur in the base of the cerebellum and fronto-temporal interface.

7.3.3 Retrospective Study of Brain Bleed Cases

Of the cases observed between 2013 and 2019, 314 provided sufficient data on both injury and impact location. Of those 314 cases, 228 did not have any indication of skull fracture. Subdural bleeds were found at locations of expected peak strain based of the

location of impact in 56% of the 228 cases. Additionally bleeding was found under the impact site in 29% of the cases. The rest of the cases showed bleeding in areas of expected peak negative pressure, or unexpected locations not associated with a hypothesized injury mechanism.

7.4 Discussion

This work set the foundation for mechanistic study of brain bleeds proliferating numerous surrogate and finite element studies (Huang 1999, Kleiven 2003, Migueis 2019) that focus on determining thresholds of intracranial damage using vessel shearing from angular acceleration as the sole mechanism. Cavitation was lost as a mechanistic contributor to intracranial damage (Panzer 2012), however, at the time cavitation formation was only a theory, and had not been shown to occur in blunt impact. In light of the work in this dissertation and current mechanistic theories, this data can be reassessed to provide evidence for the continual study of the clinical implications of cavitation.

The first point to address in these live animal tests is whether the impacts and accelerations are severe enough to generate transient CSF cavitation. Conservative cubed root of mass scaling from the smallest squirrel monkeys (head mass ~ 0.06 kg) to the pigs used in Chapter 6 (head mass ~ 3 kg), yields a biomechanical scaling coefficient of 0.27 (Panzer 2014). Based on this, the linear acceleration values from most of the translation only tests scale to the approximate threshold of cavitation formation found in Chapter 6. However, in a majority combined translational and rotational tests, the scaled kinematics

are significantly higher than the 50% risk of cavitation, indicating cavitation is plausible during these tests based on the thresholds developed in this dissertation.

Several of these seminal studies attempted to compare the effect of linear translation vs angular translation on intracranial injuries. Since fewer injuries were seen in translational tests than combined rotational and translational tests, they determined that rotational input to the system was the primary driver of these injuries. This conclusion however, assumes the kinematic inputs to each system are the same. The tangential linear acceleration in a majority of tests is the same in both the translational and combined kinematic conditions. This means that additional rotational input will significantly increase the local stresses and strains experienced at the injury site resulting in qualitatively more severe outcomes. Because these kinematic conditions are not comparable, the conclusions between effects of linear and angular kinematics on intracranial injuries cannot be made from these series of tests. This highlights how the complex geometry of the head prevents decoupling of angular and linear kinematics because global application of one form of input can result in localized response of both.

There are three assumptions found in the seminal work that need to be reconsidered. First is cavitation can only be created by linear accelerations of the head CG. This is untrue, because while linear accelerations generate inertial pressure gradients for cavitation, a purely rotational input to a system will still result in localized linear accelerations away from the point of rotation. This can induce phenomenon commonly

associated with translational inputs, often more easily because rotational input is often coupled with linear translation of the head CG.

The second assumption is the maximum shear strain profiles, illustrated in Ommaya 1971 and the finite element simulations, are the best predictors of intracranial injury location. This is supported for subdural and subarachnoid hemorrhages that are commonly associated with the parasagittal region and superior surface of the cortex (Figure 7-3) (Ommaya 1968, Gennarelli 1972, Ono 1980). However, a majority of intracranial contusions appear on the poles and inferior surface of the frontal and temporal lobes, and are rarely seen in the parasagittal region (Figure 7-4) (Ommaya 1971, Gennarelli 1979, Ono 1980). This pattern of injury is strongly reflected in the distribution of negative pressures from a combined kinematic loading event.

The third assumption is a given accelerative event, regardless of direction, results in the same contre-coup dynamic pressure response. This assumption reflects the state of the art cavitation theory at the time these papers were created. This theory used symmetric geometries and cylindrical surrogates. However, the geometric differences between the frontal and occipital regions of the head influence the magnitude of pressure localizations. The finite analysis shows that for a given kinematic input negative pressures created from an occipital impact can be 200 kPa more negative than those in a frontal impact (Figure 7-12). Additionally, for a given impact, the peak strain values are nearly identical in both magnitude and location for occipital and frontal impacts (Figure 7-13).

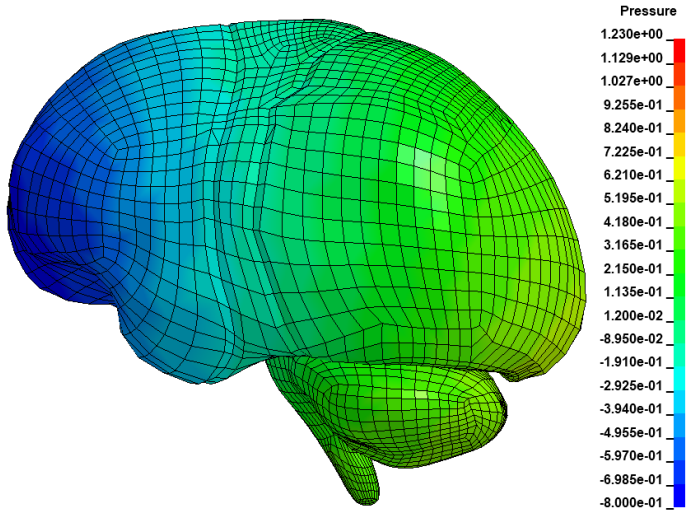

Occipital Impact

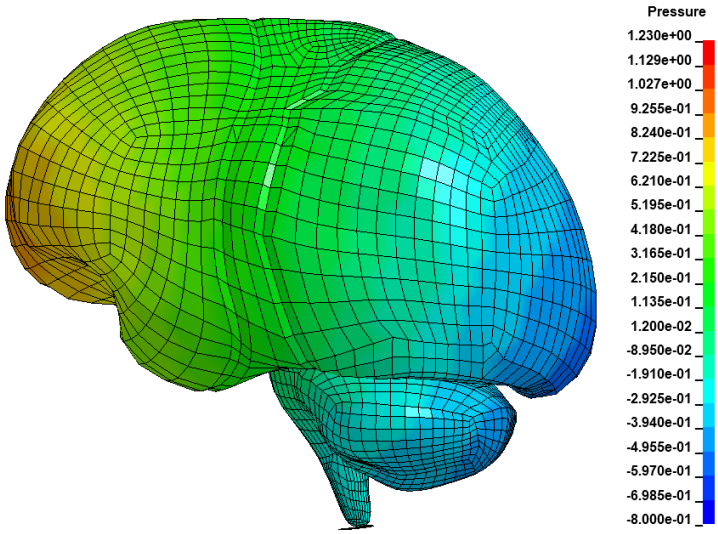

Frontal Impact

Figure 7-12: Peak negative pressure distributions in MPa of the same kinematic inputs for a frontal impact vs an occipital impact. The lowest pressure in an occipital input is approximately -200 kPa the lowest pressure of a frontal input.

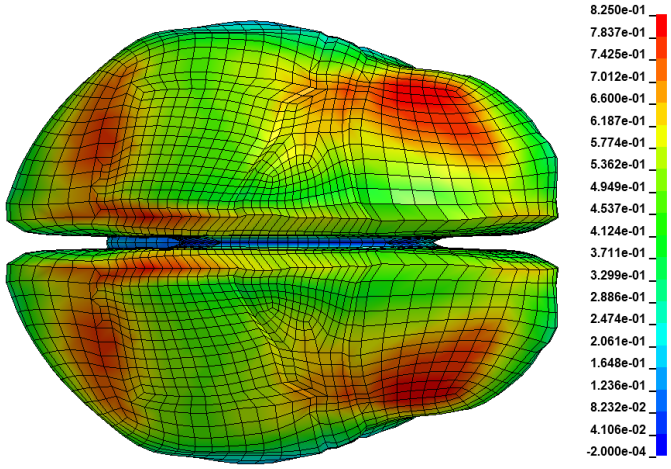

Occipital Impact

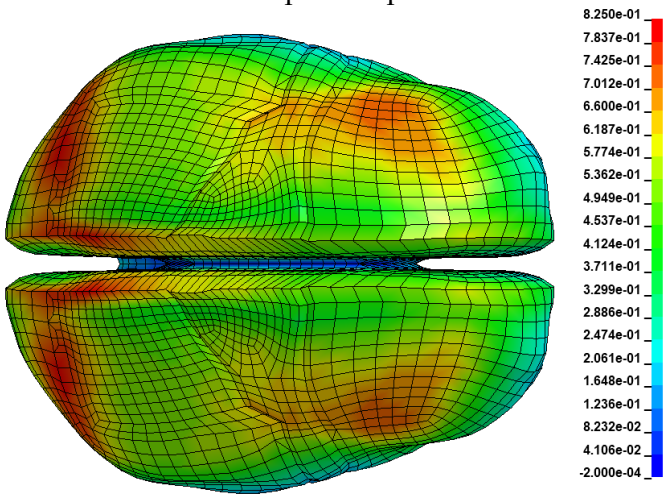

Frontal Impact

Figure 7-13: Peak effective strain distributions for an occipital and frontal impact with the same magnitude kinematic inputs. Both magnitude and location of distribution are simila.

After reconsidering these assumptions and taking into account additional information from novel tools and the work completed in this dissertation, what can a reanalysis of this data provide with respect to the clinical implications of transient cavitation? While there is no method to precisely determine if transient cavitation

occurred in these past live animal tests, scaling indicates the kinematic inputs were higher than cavitation thresholds determined in this dissertation. These seminal five papers can be separated into work that primarily reported on contusions (Ommaya 1971, Gennarelli 1979, Ono 1980) and work that reported on subdural bleeding (Ommaya 1968, Gennarelli 1972, Ono 1980).

In the tests that report contusion, primary injury locations are consistent with locations of peak low pressure seen in the finite element models (inferior surface of frontal and temporal lobes) (Figure 7-14). Very few contusions are reported at the parasagittal interface and cortex convexities (locations of peak brain strain). Gennarelli *et al.* 1979 reported contusions were more easily generated on the frontal lobes than the temporal lobes, and nearly all tests with temporal lobe contusions had corresponding frontal lobe contusions (Gennarelli 1979). This also aligns with the pressure distribution from a sagittal impact that shows negative pressures are not as significant in the temporal lobes (Figure 7-6). Ommaya *et al.* 1971 noted that contusions were more difficult to produce in frontal impacts than in occipital impacts. This phenomenon is best explained by the pressure difference of approximately -200 kPa between occipital and frontal impacts as opposed to brain strain, which is nearly identical for both frontal and occipital impacts (Figure 7-12, Figure 7-13). Because the nuances of parenchymal contusions from these seminal live animal tests can be explained by negative pressure distributions provides strong evidence that transient cavitation is a mechanistic origin of these injuries.

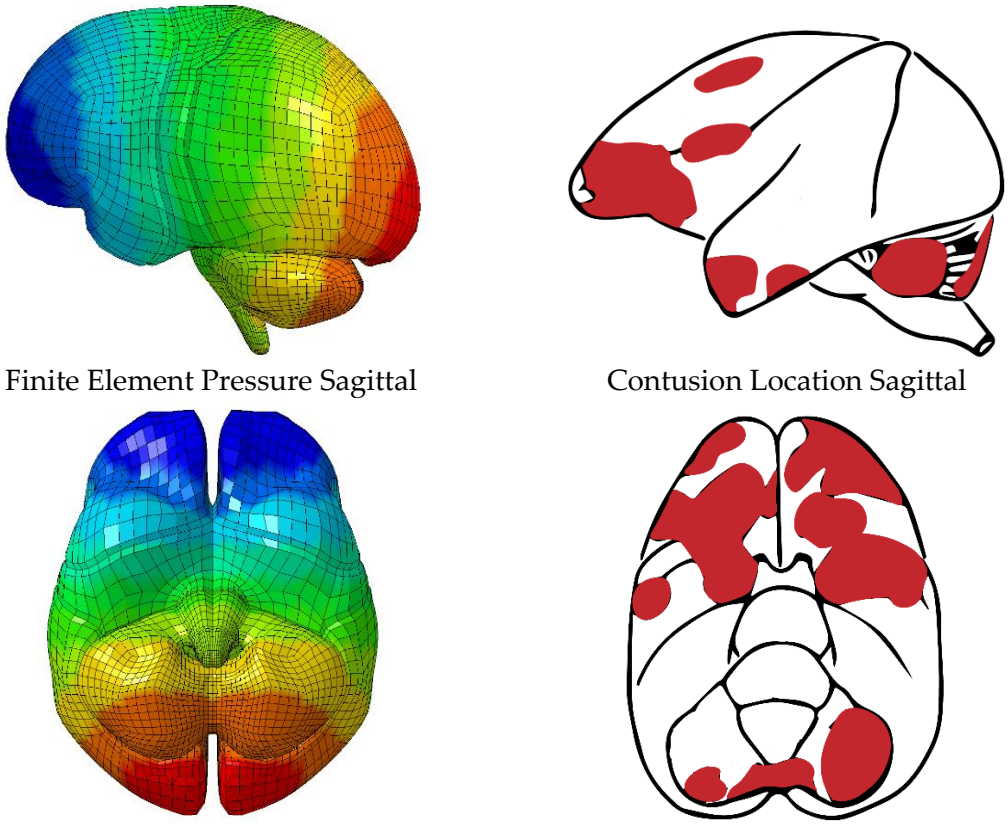

Figure 7-14: Comparison diagram of pressure distributions from finite element modeling and contusion locations from Ommaya *et al.* (Ommaya 1971). Comparison shows direct correlation between negative pressure regions (blue) and brain contusions. Finite element simulation was representative of occipital impacts that created contusions.

Trends observed on the role of skull compliance and contusion shape provide additional evidence cavitation is a mechanism of brain contusions. Ommaya *et al.* mentions how skull 'distortion' plays a role in lowering contusion thresholds by nearly double (Ommaya 1971). Ono *et al.* finds impact tests creating skull deformation more readily produce contusions (Ono 1980). As determined in Chapter 5 of this dissertation, the presence of container deformations can make it easier to induce cavitation. While

primarily focused on subdural hematomas, Gennarelli *et al.* made note of multiple contusions. They were described as 2-4 mm, circular or ovoid in shape, were surrounded by a halo of bleeding, and resulted in a conical shape of damage to the cortical tissue (Gennarelli 1972). This description is the exact pattern of damage expected from transient cavitation collapse. The size and shape of the bubble would be nearly spherical and limited to 2-4 mm by constraints of the CSF layer and a conical damage pattern is expected as force from a shockwave or microjet is dissipated as it travels through tissue. This additional evidence provides a strong case that cavitation may be a primary mechanism of brain contusions.

Studies that reported primarily subdural bleeding had higher associated linear and angular accelerations than tests associated with contusions (Ommaya 1966, Gennarelli 1972, Ono 1980). Subdural bleeding was seen in locations throughout the brain, but was localized to the parasagittal region, cerebral convexities and frontal poles (Figure 7-3). These injury locations reflect the locations of both peak strain observed in both the impact finite element impact simulations (Figure 7-7, Figure 7-9) and peak stress observed in the gelatin phantom simulation presented by Ommaya *et al.* (Figure 7-5, Figure 7-15) (Ommaya 1971). It should be mentioned that in numerous tests, subdural bleeds were seen in combination with contusions (Gennarelli 1972, Ono 1980). While the primary mechanism of subdural bleeds appears to be strain generated by motion of the skull relative to the brain, the threshold of accelerations to create these injuries appears to

be higher than what is required to generate contusions. While unknown, it is hypothesized that contusions occurred in most subdural bleeding cases, but were not reported because severe bleeding obscured them.

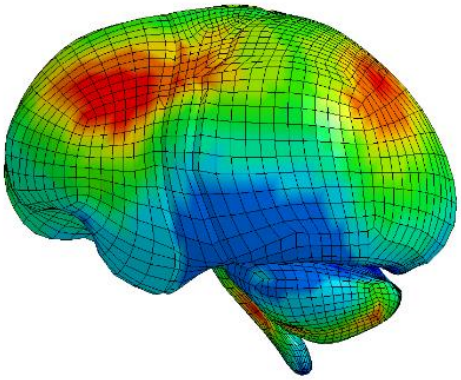

Finite Element Strain Sagittal

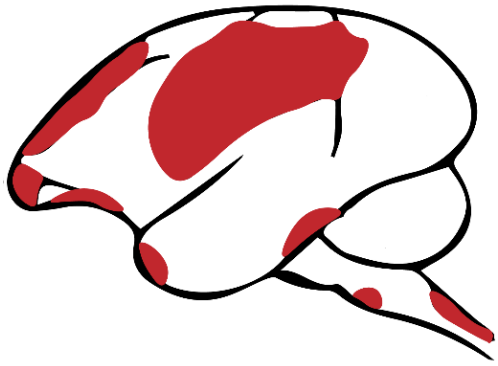

Subdural Bleeding Locations Sagittal

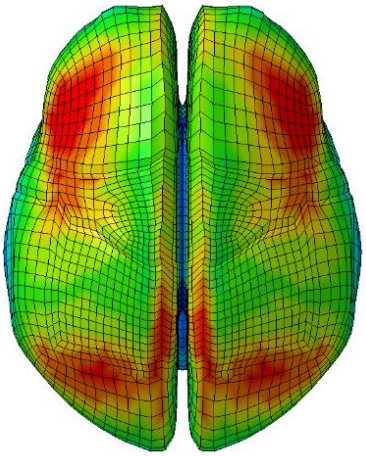

Finite Element Strain Superior Axial

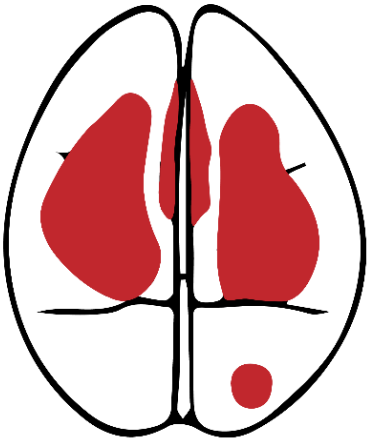

Subdural Bleeding Locations Superior Axial

Figure 7-15: Comparison diagram of brain surface strain distributions from finite element modeling and subdural bleed locations from Ommaya *et al. (Ommaya 1968)*. Comparison shows direct correlation between peak strain regions (red) and subdural bleeds. Finite element simulation was representative of occipital impacts that created subdural bleeds.

While past live animal experiments provide strong evidence transient cavitation is a primary mechanism of brain contusions from blunt impact, they do not provide

support that this injury pattern will translate to humans. Gurdjian *et al.* collected 72 autopsied cases of patients who suffered a total of 210 traumatic brain contusions (Gurdjian 1963). While there is no mention of impact direction, contusions are most numerous on the inferior surface of the frontal and temporal lobes and the lateral temporal surface. These are the locations of peak negative pressure for either occipital or lateral impacts. As mentioned previously, frontal impacts will produce negative pressures of a lower magnitude due to the geometry of the head, making occipital contusions less likely. Very few contusions are seen on the cerebral convexities or parasagittal region (locations of high cerebral strain during rotation). Sano *et al.* investigated 63 autopsies and was able to catagorize head injuries down by direction of impact (SANO 1967). As in the live animal tests, 90% of occipital impacts displayed contusions at the tip of the frontal and temporal lobes, while frontal impacts displayed primarily coup injuries. For lateral impacts, coup and contre-coup injuries occurred with similar frequencies. Contre-coup injuries were primarily acute subdural hematoma and brain contusions, and the lateral tip of the frontal lobe was not involved in these injuries. Because similar locations experience peak strain and negative pressures for lateral impacts (Figure 7-12, Figure 7-13), it is difficult to differentiate the mechanistic origin of lateral injuries without additional evidence. Finally, original work conducting a retrospective analysis of brain bleed cases found that a majority of bleeds can be explained by locations of peak strain or are directly under the impact site. These three human investigations indicate evidence

seen in previous live animal tests (transient cavitation induces brain contusions and peak tissue strain from differential movement between the skull and brain induces subdural bleeding) translates to human systems as well.

There are a number of limitations in this reanalysis that minimize the conclusions that can be drawn. The first is that there is no method to directly assess cavitation during these past seminal tests. While the input kinematics are above the scaled thresholds for cavitation determined by Chapter 6, no acoustic instrumentation was used. Next, while geometrically and anatomically accurate, the limitations in material properties of the SIMon model prevent the use of absolute values of pressure and strain for analysis. Results of the SIMon model can only be used to observe general trends in pressure and strain and make relative comparisons between models. Finally, all these tests were limited to only the sagittal plane. While this is a common direction of loading, it would be beneficial to have additional evidence indicating the trends seen in this analysis hold for coronal and axial rotations.

7.5 Conclusions

The goal of this work was to use novel tools and insight to conduct a reanalysis of seminal live subhuman primate tests that investigated intracranial bleeding. This work provides mechanistic evidence that brain contusions are a potential result of transient cavitation collapse, and subdural bleed are potentially caused by strains generated from relative motion between the skull and intracranial contents. Brain contusions were

commonly located in regions of peak negative pressures found in FE modeling such as the inferior surfaces and poles of the frontal and temporal lobes. Subdural bleeding was commonly observed in the parasagittal region and cranial vertices, areas of peak strain found in FE modeling and two dimensional stress analysis. Observations from the live subhuman primate testing were reflected in analysis of human data from reported autopsies and a retrospective hospital case review. This work in combination with the cadaveric pig tests presented in Chapter 5 provide convincing evidence transient cavitation collapse has potential clinical implications. This result is foundational to the understanding of blunt TBI and the development of injury criterion and prevention strategies. Further work must be conducted to further elucidate the role of cavitation in blunt impact TBI.

8. Conclusions

8.1 Major Contributions

Cavitation has been theorized as a mechanism of traumatic brain injury since the mid 1900's, and has been the focus of numerous research investigations using surrogate heads, frozen cadavers, and *ex-vivo* testing. However, limitations in imaging and experimental methods have made it impossible to study cavitation in an uncompromised, biofidelic model. Because of this, there was a lack of foundational knowledge surrounding cavitation formation during blunt impact events. Recent advances in high-speed imaging and acoustic sensing have enabled this work to develop an acoustic biomarker to investigate the role of cavitation in blunt impact neurotrauma, and show that blunt impacts to the head can result in cavitation formation. The work presented in this dissertation fills numerous knowledge gaps previously surrounding blunt impact cavitation and provides a foundation to investigate this phenomenon further.

It is imperative to understand the factors that influence blunt impact kinematics because they dictate the behavior of transient cavitation formation. One common theory is increasing neck muscle strength or activation will reduce head kinematics by recruiting additional effective mass, thereby reducing the risk of TBI. In Chapter 3, this theory was deemed false. Using a combined multibody and finite element cervical neck model, this work showed that due to the anatomy of the neck, head-neck coupling is low, and any benefit from increased neck strength is negligible compared to other impact factors. This

conclusion points to the need to focus more on limiting the number and magnitude of impacts and less on neck and muscle strength.

Current state of the art tools are limited in their ability to study the role of cavitation in blunt impact neurotrauma primarily because of the barrier the skull provides. In Chapter 4, a novel tool was developed, using advancements in high-speed imaging and acoustic sensing, that was capable of detecting cavitation during blunt impacts without the need to compromise the intracranial cavity. The tool is an acoustic biomarker that takes advantage of the wideband noise emitted upon cavitation collapse. Acoustic sensors listen for wideband emissions upon collapse, and wavelet transforms differentiate acoustic emissions of cavitation collapse from blunt impact noise.

Stiff, yet compliant structures (skull and supporting tissues) contain the biological materials where transient cavitation occurs. It is imperative to understand the role container compliance plays in the dynamics of bubble formation to develop a better understanding of transient cavitation in biological systems. In Chapter 5, experimental acrylic head surrogates and a numerical finite element model were used to determine the presence the compliance of the container wall is a primary driver of cavitation formation and a foramen or membrane influences the size of bubble growth.

Up to this point in time, blunt impact transient cavitation has not been observed in the intracranial cavity of an uncompromised soft tissue model. In Chapter 6, a fresh non-frozen full body pig model and the acoustic biomarker developed in Chapter 5 were

used to detect intracranial transient cavitation collapse in uncompromised soft tissue. The data show that intracranial soft tissue cavitation occurs at impact levels below catastrophic injury such as open skull fracture, DAI, or massive hemorrhaging.

Multiple impacts to a given specimen were required to develop the results of Chapter 6. Therefore, while cavitation was detected, no conclusions could be drawn surrounding the clinical implications of transient cavitation collapse in blunt impact TBI. In Chapter 7, clinical implications of transient cavitation were explored through the reanalysis of seminal live subhuman primate studies conducted from the 1960s – 1980s. This reanalysis took advantage of advances in finite element modeling and cavitation theory not available to the authors at the time of their experimentation. The data shows that brain contusions correspond to locations of peak negative pressure and are most likely the result of transient cavitation collapse. Limitations in methodology prevent conclusions of this work from directly linking cavitation to clinical implications, and further work is needed to understand the role cavitation has in blunt impact brain injuries.

Prior to this dissertation, work on blunt impact cavitation had been restricted to non biological surrogates, *ex-vivo* testing, and compromised cadavers, all with significant limitations that prohibit the direct study of intracranial transient CSF cavitation. This restriction is due to the inability to image or detect transient CSF cavitation through the skull. The culmination of this work summarized biological conditions that influence cavitation, developed a tool to detect cavitation through the skull, showed blunt impacts

to the head can induce transient cavitation under biologically relevant conditions, and provided evidence based on seminal subhuman primate testing that cavitation has clinical implications for blunt impact TBI.

8.2 Minor Contributions

There are multiple minor contributions determined in this work complementary to the primary investigation. In lieu of using human participants or cadavers, investigators often use a mechanical surrogate - either a Hybrid III (HIII) neck attached to a dummy head or a freely dropped dummy head form (free-head) when conducting head impact testing. In Chapter 3, it was determined the biofidelic limitations of Hybrid III and free head experimental conditions must be recognized when reporting results. Depending on the injury metrics used, the neck type can have varying consequences.

In Chapter 5, the overall container compliance was found to be more significant in the incidence of cavitation than the presence of a single compliant membrane. However, data shows that a compliant membrane resulted in larger bubble size. Since cavitation fluid is nearly incompressible, the presence of an elastic membrane allows for rapid volume expansion and enables the bubble to grow. This is important because the skull has features (such as the foramen magnum) that will also allow for this expansion.

While conducting live animal experiments is beyond the scope of this dissertation, in Chapter 6 a methodology was developed that enables the study of clinical implications of transient cavitation using a cadaveric pig model. This sub-study displayed three

important results. First, blood was not seen in dissection when heparin was injected prior to euthanasia, and Evans blue reach all portions of the cerebral vasculature. Next, breaches in the blood brain barrier may be indicated by diffuse coloration of the Evans blue in neurological tissue. Finally, cavitation is still observed with the biofidelic experimental addition of a pressurized vasculature.

Finally, when investigating the clinical implications of transient cavitation in traumatic brain injury in Chapter 7, subdural bleeding was found to be associated with locations of high strain caused by shearing of the skull relative to the brain. Additionally, subdural bleeds were more difficult to induce in the subhuman primate models through sagittal plane impacts than brain contusions. This conclusion is supported by trends seen in a retrospective analysis of brain bleed cases.

8.3 Future Work

Even though this dissertation has provided noteworthy contributions towards building our understanding of transient cavitation in blunt impact TBI, a lot of important work remains. This work was limited to full body pig cadaver models, and while this study laid the foundation for perfused vasculature tests to mimic a live animal, only two successful tests were conducted. The next step in this work will be to continue these tests in order to fine-tune the procedure to be sensitive for intracranial damage, and provide enough tests to have statistical power for direct conclusions of clinical implications for cavitation. Following cadaveric tests, it will be important to carry out a similar procedure

using live pigs to ensure the trends still hold. Additionally, live animal tests will enable the investigation of the immune response following cavitation and impact, and use of more sensitive histological tests for intracranial tissue damage.

A significant amount of work conducted in this dissertation is limited to impacts that produced motion within the sagittal plane. Autopsy data analyzed in Chapter 7 indicated this phenomenon might also occur during impacts that result in motion through the coronal plane. In addition to more cadaver tests with impact to the frontal bone, future work should develop a methodology that investigates this phenomenon in the coronal plane. This will require new surgical procedures, sensor placement, and impacting device. This work was also limited to short duration impacts due to the stiff interaction between the head and 70A shore impactor. Future work should investigate the sensitivity of these phenomenon to impact stiffness that would widen the applicable scenarios of this work.

Currently, the method of determining cavitation from an acoustic signal requires human input that can provide some subjectivity. Future work will aim to develop an algorithm that does not rely on human observation of a colored wavelet transform, and instead uses statistical thresholds and comparisons to determine cavitation from an acoustic signal. This would be aided by the development of a deep learning/machine learning model that use a variety of acrylic surrogate test conditions to train.

References

ADELOYE, A., K. R. KATTAN AND F. N. SILVERMAN (1975). "Thickness of the normal skull in the American blacks and whites." American Journal of Physical Anthropology **43**(1): 23-30.

ALSHAREEF, A., J. S. GIUDICE, J. FORMAN, D. F. SHEDD, K. A. REYNIER, T. WU, S. SOCHOR, M. R. SOCHOR, R. S. SALZAR AND M. B. PANZER (2020). "Biomechanics of the Human Brain During Dynamic Rotation of the Head." Journal of Neurotrauma(ja).

BARSHES, N., A. DEMOPOULOS AND H. H. ENGELHARD (2005). Anatomy and physiology of the leptomeninges and CSF space. Leptomeningeal Metastases, Springer**:** 1-16.

BASS, C. R., M. B. PANZER, K. A. RAFAELS, G. WOOD, J. SHRIDHARANI AND B. CAPEHART (2012). "Brain injuries from blast." Annals of biomedical engineering **40**(1): 185-202.

BECKWITH, J. G., R. M. GREENWALD AND J. J. CHU (2012). "Measuring head kinematics in football: correlation between the head impact telemetry system and Hybrid III headform." Annals of biomedical engineering **40**(1): 237-248.

BENNETT, C. M., M. MILLER AND G. WOLFORD (2009). "Neural correlates of interspecies perspective taking in the post-mortem Atlantic Salmon: an argument for multiple comparisons correction." Neuroimage **47**(Suppl 1): S125.

BIGLER, B. (2020). Shock Propagation in Mechanical Models of Traumatic Brain Injury, Duke University.

BRENNEN, C. E. (2014). Cavitation and bubble dynamics, Cambridge University Press.

BROGLIO, S. P., J. J. SOSNOFF, S. SHIN, X. HE, C. ALCARAZ AND J. ZIMMERMAN (2009). "Head impacts during high school football: a biomechanical assessment." Journal of athletic training **44**(4): 342-349.

BRUNEAU, D. (2019). Investigation of Head and Brain Response in Football Helmet Impacts using a Finite Element Model of the Head and Neck with Active Muscle, University of Waterloo.

BURGESS, M., I. APOSTOLAKIS AND E. KONOFAGOU (2018). "Power cavitation-guided blood-brain barrier opening with focused ultrasound and microbubbles." Physics in Medicine & Biology **63**(6): 065009.

CANCHI, S., K. KELLY, Y. HONG, M. A. KING, G. SUBHASH AND M. SARNTINORANONT (2017). "Controlled single bubble cavitation collapse results in jet-induced injury in brain tissue." Journal of the mechanical behavior of biomedical materials **74**: 261-273.

CARSTENSEN, E. L., S. GRACEWSKI AND D. DALECKI (2000). "The search for cavitation in vivo." Ultrasound in medicine & biology **26**(9): 1377-1385.

CDC (2003). Report to Congress on Mild Traumatic Brain Injury in the United States. C. f. D. C. a. Prevention.

CDC (2014). Surveillance Report of Traumatic Brain Injury-related Emergency Department Visits, Hospitalizations, and Deaths. C. f. D. Control.

CHANCEY, V. C., D. OTTAVIANO, B. S. MYERS AND R. W. NIGHTINGALE (2007). "A kinematic and anthropometric study of the upper cervical spine and the occipital condyles." Journal of biomechanics **40**(9): 1953-1959.

CHATELIN, S., A. CONSTANTINESCO AND R. WILLINGER (2010). "Fifty years of brain tissue mechanical testing: from in vitro to in vivo investigations." Biorheology **47**(5-6): 255-276.

CHEN, H., A. A. BRAYMAN, M. R. BAILEY AND T. J. MATULA (2010). "Blood vessel rupture by cavitation." Urological research **38**(4): 321-326.

CHRISTMAN, D. R. (1972). Dynamic properties of poly (methylmethacrylate)(PMMA)(Plexiglas), General Motors Technical Center Warren MI Materials and Structures Lab.

COLEMAN, A., M. CHOI AND J. SAUNDERS (1996). "Detection of acoustic emission from cavitation in tissue during clinical extracorporeal lithotripsy." Ultrasound in Medicine and Biology **22**(8): 1079-1087.

COLLINS, C. L., E. N. FLETCHER, S. K. FIELDS, L. KLUCHUROSKY, M. K. ROHRKEMPER, R. D. COMSTOCK AND R. C. CANTU (2014). "Neck strength: a protective factor reducing risk for concussion in high school sports." The journal of primary prevention **35**(5): 309-319.

COLLINS, M. W., A. P. KONTOS, E. REYNOLDS, C. D. MURAWSKI AND F. H. FU (2014). "A comprehensive, targeted approach to the clinical care of athletes following sport-related concussion." Knee Surgery, Sports Traumatology, Arthroscopy **22**(2): 235-246.

CULLEN, D. K., J. P. HARRIS, K. D. BROWNE, J. A. WOLF, J. E. DUDA, D. F. MEANEY, S. S. MARGULIES AND D. H. SMITH (2016). "A porcine model of traumatic brain injury via head rotational acceleration." Injury Models of the Central Nervous System: Methods and Protocols: 289-324.

DIBB, A. T., C. A. COX, R. W. NIGHTINGALE, J. F. LUCK, H. C. CUTCLIFFE, B. S. MYERS, K. B. ARBOGAST, T. SEACRIST AND C. R. BASS (2013). "Importance of muscle activations for biofidelic pediatric neck response in computational models." Traffic injury prevention **14**(sup1): S116-S127.

DIBB, A. T., H. C. CUTCLIFFE, J. F. LUCK, C. A. COX, B. S. MYERS, C. R. BASS, K. B. ARBOGAST, T. SEACRIST AND R. W. NIGHTINGALE (2014). "Pediatric head and neck dynamics in frontal impact: Analysis of important mechanical factors and proposed neck performance corridors for 6-and 10-year-old ATDs." Traffic injury prevention **15**(4): 386-394.

DIBB, A. T., R. W. NIGHTINGALE, V. C. CHANCEY AND L. E. FRONHEISER (2006). "Comparative structural neck responses of the THOR-NT, Hybrid III, and human in combined tension-bending and pure bending." Stapp car crash journal **50**: 567.

DOD (2009). VA DoD clinical practice guidelines. D. o. V. Affairs. Washington, DC.

DOPERAK, J., K. ANDERSON, M. COLLINS AND K. EMAMI (2019). "Sport-related concussion evaluation and management." Clinics in sports medicine **38**(4): 497-511.

DOUGAN, C., S. GALARZA, C. BARNEY, S. CAI, A. CROSBY AND S. PEYTON (2020). "Brain Mechanics Drive Cavitation and Fracture Response." Bulletin of the American Physical Society.

ECKERSLEY, C. P., J. OP'T EYNDE, M. Z. ABRAMS, W. Y. ALLEN, M. LI, J. YAO AND C. R. BASS (2020). Acoustic Detection of Blunt-Induced Cavitation in the Head. International Research Council on the Biomechanics of Injury.

ECKNER, J. T., A. GOSHTASBI, K. CURTIS, A. KAPSHAI, E. MYYRA, L. M. FRANCO, M. FAVRE, J. A. JACOBSON AND J. A. ASHTON-MILLER (2018). "Feasibility and Effect of Cervical Resistance Training on Head Kinematics in Youth Athletes: A Pilot Study." American journal of physical medicine & rehabilitation **97**(4): 292-297.

ECKNER, J. T., Y. K. OH, M. S. JOSHI, J. K. RICHARDSON AND J. A. ASHTON-MILLER (2014). "Effect of neck muscle strength and anticipatory cervical muscle activation on the kinematic response of the head to impulsive loads." The American journal of sports medicine **42**(3): 566-576.

EIBAND, A. M. (1959). "Human tolerance to rapidly applied accelerations: a summary of the literature."

ESPINDOLA, D., S. LEE AND G. PINTON (2017). "Shear shock waves are observed in the brain." arXiv preprint arXiv:1705.10672.

FINKELSTEIN, E., P. S. CORSO AND T. R. MILLER (2006). The incidence and economic burden of injuries in the United States, Oxford University Press, USA.

FRY, F. AND J. BARGER (1978). "Acoustical properties of the human skull." The Journal of the Acoustical Society of America **63**(5): 1576-1590.

GANPULE, S., N. DAPHALAPURKAR, M. P. CETINGUL AND K. RAMESH (2018). "Effect of bulk modulus on deformation of the brain under rotational accelerations." Shock waves **28**(1): 127-139.

GENNARELLI, T., A. OMMAYA AND L. THIBAULT (1971). Comparison of translational and rotational head motions in experimental cerebral concussion. Proc. 15th Stapp Car Crash Conference.

GENNARELLI, T. A., J. M. ABEL, H. ADAMS AND D. GRAHAM (1979). "Differential tolerance of frontal and temporal lobes to contusion induced by angular acceleration." SAE Transactions: 3503-3514.

GENNARELLI, T. A., L. THIBAULT AND A. K. OMMAYA (1972). Pathophysiologic responses to rotational and translational accelerations of the head, SAE Technical Paper.

GENNARELLI, T. A. AND L. E. THIBAULT (1982). "Biomechanics of acute subdural hematoma." Journal of Trauma and Acute Care Surgery **22**(8): 680-686.

GIAMMARINARO, B., F. COULOUVRAT AND G. PINTON (2016). "Numerical simulation of focused shock shear waves in soft solids and a two-dimensional nonlinear homogeneous model of the brain." Journal of biomechanical engineering **138**(4): 041003.

GIAMMARINARO, B., D. ESPÍNDOLA, F. COULOUVRAT AND G. PINTON (2018). "Focusing of Shear Shock Waves." Physical Review Applied **9**(1): 014011.

GOELLER, J., A. WARDLAW, D. TREICHLER, J. O'BRUBA AND G. WEISS (2012). "Investigation of cavitation as a possible damage mechanism in blast-induced traumatic brain injury." Journal of neurotrauma **29**(10): 1970-1981.

GROSS, A. G. (1958). "A new theory on the dynamics of brain concussion and brain injury." Journal of neurosurgery **15**(5): 548-561.

GURDJIAN, E. S., H. LISSNER AND L. PATRICK (1963). Concussion: mechanism and pathology. Proceedings: American Association for Automotive Medicine Annual Conference, Association for the Advancement of Automotive Medicine.

HAMHABER, U., D. KLATT, S. PAPAZOGLOU, M. HOLLMANN, J. STADLER, I. SACK, J. BERNARDING AND J. BRAUN (2010). "In vivo magnetic resonance elastography of human brain at 7 T and 1.5 T." Journal of Magnetic Resonance Imaging **32**(3): 577-583.

HANIFF, S. AND P. A. TAYLOR (2017). "In silico investigation of blast-induced intracranial fluid cavitation as it potentially leads to traumatic brain injury." Shock Waves **27**(6): 929-945.

HENDEE, S. P., R. M. GREENWALD AND J. J. CRISCO (1998). "Static and dynamic properties of various baseballs." Journal of Applied Biomechanics **14**: 390-400.

HERBERT, E., S. BALIBAR AND F. CAUPIN (2006). "Cavitation pressure in water." Physical Review E **74**(4): 041603.

HUANG, H.-M., M.-C. LEE, W.-T. CHIU, C.-T. CHEN AND S.-Y. LEE (1999). "Three-dimensional finite element analysis of subdural hematoma." Journal of Trauma and Acute Care Surgery **47**(3): 538-544.

HUKKELHOVEN, C. W., A. J. RAMPEN, A. I. MAAS, E. FARACE, J. D. F. HABBEMA, A. MARMAROU, L. F. MARSHALL, G. D. MURRAY AND E. W. STEYERBERG (2006). "Some prognostic models for traumatic brain injury were not valid." Journal of clinical epidemiology **59**(2): 132-143.

ILYICHEV, V., V. KORETZ AND N. MELNIKOV (1989). "Spectral characteristics of acoustic cavitation." Ultrasonics **27**(6): 357-361.

JAMES, S. L., A. THEADOM, R. G. ELLENBOGEN, M. S. BANNICK, W. MONTJOY-VENNING, L. R. LUCCHESI, N. ABBASI, R. ABDULKADER, H. N. ABRAHA AND J. C. ADSUAR (2019). "Global, regional, and national burden of traumatic brain injury and spinal cord injury, 1990–2016: a systematic analysis for the Global Burden of Disease Study 2016." The Lancet Neurology **18**(1): 56-87.

JIN, X., Z. FENG, V. MIKA, H. LI, D. C. VIANO AND K. H. YANG (2017). "The role of neck muscle activities on the risk of mild traumatic brain injury in American football." Journal of biomechanical engineering **139**(10): 101002.

JOHNSON, C. L., M. D. MCGARRY, E. E. VAN HOUTEN, J. B. WEAVER, K. D. PAULSEN, B. P. SUTTON AND J. G. GEORGIADIS (2013). "Magnetic resonance elastography of the brain using multishot spiral readouts with self-navigated motion correction." Magnetic resonance in medicine **70**(2): 404-412.

JONES, B. H., M. CANHAM-CHERVAK, S. CANADA, T. A. MITCHENER AND S. MOORE (2010). "Medical surveillance of injuries in the US military: descriptive epidemiology and recommendations for improvement." American journal of preventive medicine **38**(1): S42-S60.

KANDEL, E., J. SCHWARTZ, T. JESSELL, S. SIEGELBAUM AND A. J. HUDSPETH (2013). Principles of Neural Science, McGraw-Hill Companies.

KING, A. I., K. H. YANG, L. ZHANG, W. HARDY AND D. C. VIANO (2003). Is head injury caused by linear or angular acceleration. IRCOBI conference.

KLEIVEN, S. (2003). "Influence of impact direction on the human head in prediction of subdural hematoma." Journal of neurotrauma **20**(4): 365-379.

KNAPP, R. T. (1955). "Recent investigations of the mechanics of cavitation and cavitation damage." Transactions of the ASME **77**: 1045-1054.

KNUTSEN, A. K., A. D. GOMEZ, M. GANGOLLI, W.-T. WANG, D. CHAN, Y.-C. LU, E. CHRISTOFOROU, J. L. PRINCE, P. V. BAYLY AND J. A. BUTMAN (2020). "In vivo estimates of axonal stretch and 3D brain deformation during mild head impact." Brain Multiphysics: 100015.

KONTOS, A. P. AND M. W. COLLINS (2018). Concussion: A Clinical Profile Approach to Assesment and Treatment, American Psychological Association.

LESSLEY, D. J., R. W. KENT, J. R. FUNK, C. P. SHERWOOD, J. M. CORMIER, J. R. CRANDALL, K. B. ARBOGAST AND B. S. MYERS (2018). "Video analysis of reported concussion events in the National Football League during the 2015-2016 and 2016-2017 seasons." The American journal of sports medicine **46**(14): 3502-3510.

LI, M., B. LAN, G. SANKIN, Y. ZHOU, W. LIU, J. XIA, D. WANG, G. TRAHEY, P. ZHONG AND J. YAO (2019). "Simultaneous photoacoustic imaging and cavitation mapping in shockwave lithotripsy." IEEE transactions on medical imaging.

LIU, Y. K., K. KRIEGER, G. NJUS, K. UENO AND M. CONNORS (1982). "Cervical spine stiffness and geometry of the young human male." DTIC Document.

LO, J., L. CHAN AND S. FLYNN (2020). "A systematic review of the incidence, prevalence, costs, and activity/work limitations of amputation, osteoarthritis, rheumatoid arthritis, back pain, multiple sclerosis, spinal cord injury, stroke, and traumatic brain injury in the United States: a 2019 update." Archives of physical medicine and rehabilitation.

LUBOCK, P. AND W. GOLDSMITH (1980). "Experimental cavitation studies in a model head-neck system." Journal of Biomechanics **13**(12): 1041-1052.

MAAS, A. I., N. STOCCHETTI AND R. BULLOCK (2008). "Moderate and severe traumatic brain injury in adults." The Lancet Neurology **7**(8): 728-741.

MANSELL, J., R. T. TIERNEY, M. R. SITLER, K. A. SWANIK AND D. STEARNE (2005). "Resistance training and head-neck segment dynamic stabilization in male and female collegiate soccer players." Journal of athletic training **40**(4): 310.

MARGULIES, S. S. AND L. E. THIBAULT (1992). "A proposed tolerance criterion for diffuse axonal injury in man." Journal of biomechanics **25**(8): 917-923.

MARJOUX, D., D. BAUMGARTNER, C. DECK AND R. WILLINGER (2008). "Head injury prediction capability of the HIC, HIP, SIMon and ULP criteria." Accident Analysis & Prevention **40**(3): 1135-1148.

MATLAGA, B. R., J. A. MCATEER, B. A. CONNORS, R. K. HANDA, A. P. EVAN, J. C. WILLIAMS, J. E. LINGEMAN AND L. R. WILLIS (2008). "Potential for cavitation-mediated tissue damage in shockwave lithotripsy." Journal of endourology **22**(1): 121-126.

MATWEB. (2019). "Overview of Materials for Cast Acrylic."

MCCRORY, P., W. MEEUWISSE, J. DVORAK, M. AUBRY, J. BAILES, S. BROGLIO, R. C. CANTU, D. CASSIDY, R. J. ECHEMENDIA AND R. J. CASTELLANI (2017). "Consensus statement on concussion in sport—the 5th international conference on concussion in sport held in Berlin, October 2016." Br J Sports Med: bjsports-2017-097699.

MCELHANEY, J. H., J. L. FOGLE, J. W. MELVIN, R. R. HAYNES, V. L. ROBERTS AND N. M. ALEM (1970). "Mechanical properties of cranial bone." Journal of biomechanics **3**(5): 495-511.

MCELHANEY, J. H., J. W. MELVIN, V. L. ROBERTS AND H. D. PORTNOY (1973). Dynamic characteristics of the tissues of the head. Perspectives in biomedical engineering, Springer**:** 215-222.

MCKEE, A. C. AND D. H. DANESHVAR (2015). The neuropathology of traumatic brain injury. Handbook of clinical neurology, Elsevier. **127:** 45-66.

MEANEY, D. F., B. MORRISON AND C. D. BASS (2014). "The mechanics of traumatic brain injury: a review of what we know and what we need to know for reducing its societal burden." Journal of biomechanical engineering **136**(2): 021008.

MERTZ, H. J., P. PRASAD AND G. NUSHOLTZ (1996). "Head injury risk assessment for forehead impacts." Stapp Car Crash Journal.

MIGUEIS, G., F. FERNANDES, M. PTAK, M. RATAJCZAK AND R. A. DE SOUSA (2019). "Detection of bridging veins rupture and subdural haematoma onset using a finite element head model." Clinical Biomechanics **63**: 104-111.

MIHALIK, J. P., J. T. BLACKBURN, R. M. GREENWALD, R. C. CANTU, S. W. MARSHALL AND K. M. GUSKIEWICZ (2010). "Collision type and player anticipation affect head impact severity among youth ice hockey players." Pediatrics **125**(6): e1394-e1401.

MIHALIK, J. P., K. M. GUSKIEWICZ, S. W. MARSHALL, R. M. GREENWALD, J. T. BLACKBURN AND R. C. CANTU (2011). "Does cervical muscle strength in youth ice hockey players affect head impact biomechanics?" Clinical Journal of Sport Medicine **21**(5): 416-421.

MOHAN, P., D. MARZOUGUI AND C.-D. KAN (2009). "Development and validation of hybrid iii crash test dummy." SAE Technical Paper.

MOORE, D. F., R. A. RADOVITZKY, L. SHUPENKO, A. KLINOFF, M. S. JAFFEE AND J. M. ROSEN (2008). "Blast physics and central nervous system injury."

MOORE, K., A. DALLEY AND A. AGUR (2014). Clinically Oriented Anatomy.

NEWMAN, J. A. (1980). Head injury criteria in automotive crash testing, SAE Technical Paper.

NEWMAN, J. A. AND N. SHEWCHENKO (2000). "A proposed new biomechanical head injury assessment function-the maximum power index." SAE Technical Paper.

NHTSA (2011). Occupant Crash Protection 571.208, Department of Transportation.

NIGHTINGALE, R. W., J. H. MCELHANEY, W. J. RICHARDSON AND B. S. MYERS (1996). "Dynamic responses of the head and cervical spine to axial impact loading." Journal of biomechanics **29**(3): 307-318.

NUSHOLTZ, G. S., L. G. GLASCOE AND E. B. WYLIE (1997). Cavitation during head impact, SAE Technical Paper.

NUSHOLTZ, G. S., P. LUX, P. KAIKER AND M. A. JANICKI (1984). "Head impact response—Skull deformation and angular accelerations." SAE transactions: 800-833.

NUSHOLTZ, G. S., B. WYLIE AND L. G. GLASCOE (1995). "Cavitation/boundary effects in a simple head impact model." Aviation, space, and environmental medicine **66**(7): 661-667.

NUSHOLTZ, G. S., B. E. WYLIE AND L. G. GLASCOE (1995). "Internal cavitation in simple head impact model." Journal of neurotrauma **12**(4): 707-714.

O'CONNOR, K. L., S. ROWSON, S. M. DUMA AND S. P. BROGLIO (2017). "Head-impact–measurement devices: a systematic review." Journal of athletic training **52**(3): 206-227.

OMMAYA, A. AND A. HIRSCH (1971). "Tolerances for cerebral concussion from head impact and whiplash in primates." Journal of biomechanics **4**(1): 13-21.

OMMAYA, A. K., F. FAAS AND P. YARNELL (1968). "Whiplash injury and brain damage: an experimental study." Jama **204**(4): 285-289.

OMMAYA, A. K., R. L. GRUBB AND R. A. NAUMANN (1971). "Coup and contre-coup injury: observations on the mechanics of visible brain injuries in the rhesus monkey." Journal of neurosurgery **35**(5): 503-516.

OMMAYA, A. K., A. E. HIRSCH AND J. L. MARTINEZ (1966). The role of whiplash in cerebral concussion, SAE Technical Paper.

ONO, K., A. KIKUCHI, M. NAKAMURA, H. KOBAYASHI AND N. NAKAMURA (1980). "Human Head Tolerance to Sagittal Impact—Reliable Estimation Deduced from Experimental Head Injury Using Subhuman Primates and Human Cadaver Skulls." SAE Transactions: 3837-3866.

PANZER, M. B. (2012). Numerical Simulation of Primary Blast Brain Injury, Duke University.

PANZER, M. B., B. S. MYERS, B. P. CAPEHART AND C. R. BASS (2012). "Development of a finite element model for blast brain injury and the effects of CSF cavitation." Annals of biomedical engineering **40**(7): 1530-1544.

PANZER, M. B., G. W. WOOD AND C. R. BASS (2014). "Scaling in neurotrauma: how do we apply animal experiments to people?" Experimental neurology **261**: 120-126.

PISHCHALNIKOV, Y. A., O. A. SAPOZHNIKOV, M. R. BAILEY, J. C. WILLIAMS JR, R. O. CLEVELAND, T. COLONIUS, L. A. CRUM, A. P. EVAN AND J. A. MCATEER (2003). "Cavitation bubble cluster activity in the breakage of kidney stones by lithotripter shockwaves." Journal of endourology **17**(7): 435-446.

PLESSET, M. S. (1949). "The dynamics of cavitation bubbles." Journal of applied mechanics **16**: 277-282.

RAPET, J., Y. TAGAWA AND C.-D. OHL (2019). "Shear-wave generation from cavitation in soft solids." Applied Physics Letters **114**(12): 123702.

RAYLEIGH, L. (1917). "VIII. On the pressure developed in a liquid during the collapse of a spherical cavity." The London, Edinburgh, and Dublin Philosophical Magazine and Journal of Science **34**(200): 94-98.

REGASA, L. E., Y. AGIMI AND K. C. STOUT (2019). "Traumatic brain injury following military deployment: evaluation of diagnosis and cause of injury." The Journal of head trauma rehabilitation **34**(1): 21-29.

REID, S., G. RAVIV AND S. REID JR (1981). "Neck muscle resistance to head impact." Aviation, space, and environmental medicine **52**(2): 78-84.

REYNIER, K. A., A. ALSHAREEF, E. J. SANCHEZ, D. F. SHEDD, S. R. WALTON, N. K. ERDMAN, B. T. NEWMAN, J. S. GIUDICE, M. J. HIGGINS AND J. R. FUNK (2020). "The effect of muscle activation on head kinematics during non-injurious head impacts in human subjects." Annals of Biomedical Engineering **48**(12): 2751-2762.

SALZAR, R. S., D. TREICHLER, A. WARDLAW, G. WEISS AND J. GOELLER (2017). "Experimental investigation of cavitation as a possible damage mechanism in blast-induced traumatic brain injury in post-mortem human subject heads." Journal of neurotrauma **34**(8): 1589-1602.

SANO, K., N. NAKAMURA, K. HIRAKAWA, H. MASUZAWA, K. HASHIZUME, T. HAYASHI AND S. FUJII (1967). "Mechanism and dynamics of closed head injuries." Neurologia medico-chirurgica **9**: 21-33.

SCHMIDT, J. D., K. M. GUSKIEWICZ, J. T. BLACKBURN, J. P. MIHALIK, G. P. SIEGMUND AND S. W. MARSHALL (2014). "The influence of cervical muscle characteristics on head impact biomechanics in football." The American journal of sports medicine **42**(9): 2056-2066.

SHELDON, C., R. PUDENZ AND J. RESTARSKI (1946). The lucite calvarium, a method for direct observation of the brain. II. Cranial trauma and brain movement, Naval Medical Research Institute and US Naval Hospital, Research Project X-182, Report.

SHRIDHARANI, J. K. (2016). Injury Detection and Localization in the Spine using Acoustic Emission, Duke University.

SIMONEAU, M., M. DENNINGER AND T. C. HAIN (2008). "Role of loading on head stability and effective neck stiffness and viscosity." Journal of biomechanics **41**(10): 2097-2103.

SINGH, D. AND D. S. CRONIN (2015). Investigation of cavitation using a modified Hopkinson apparatus. Dynamic Behavior of Materials, Volume 1, Springer**:** 177-183.

SUN, T., G. SAMIOTAKI, S. WANG, C. ACOSTA, C. C. CHEN AND E. E. KONOFAGOU (2015). "Acoustic cavitation-based monitoring of the reversibility and permeability of ultrasound-induced blood-brain barrier opening." Physics in Medicine & Biology **60**(23): 9079.

SUSSMAN, E. S., A. L. HO, A. V. PENDHARKAR AND J. GHAJAR (2016). "Clinical evaluation of concussion: the evolving role of oculomotor assessments." Neurosurgical focus **40**(4): E7.

TAKHOUNTS, E. G., R. H. EPPINGER, J. Q. CAMPBELL, R. E. TANNOUS, E. D. POWER AND L. S. SHOOK (2003). On the development of the SIMon finite element head model. SAE CONFERENCE PROCEEDINGS P, SAE; 1999.

TAKHOUNTS, E. G., S. A. RIDELLA, V. HASIJA, R. E. TANNOUS, J. Q. CAMPBELL, D. MALONE, K. DANELSON, J. STITZEL, S. ROWSON AND S. DUMA (2008). Investigation of traumatic brain injuries using the next generation of simulated injury monitor (SIMon) finite element head model, SAE Technical Paper.

TANG, H., C. C. J. WANG, D. BLANKSCHTEIN AND R. LANGER (2002). "An investigation of the role of cavitation in low-frequency ultrasound-mediated transdermal drug transport." Pharmaceutical research **19**(8): 1160-1169.

TEASDALE, G. AND B. JENNETT (1974). "Assessment of coma and impaired consciousness: a practical scale." The Lancet **304**(7872): 81-84.

THIBAULT, L. E. AND T. A. GENNARELLI (1985). Biomechanics of diffuse brain injuries, SAE Technical Paper.

TIERNEY, R. T., M. R. SITLER, C. B. SWANIK, K. A. SWANIK, M. HIGGINS AND J. TORG (2005). "Gender differences in head-neck segment dynamic stabilization during head acceleration." Med Sci Sports Exerc **37**(2): 272-279.

TORRENCE, C. AND G. P. COMPO (1998). "A practical guide to wavelet analysis." Bulletin of the American Meteorological society **79**(1): 61-78.

UNTERHARNSCHEIDT, F. (1971). Translational versus rotational acceleration-animal experiments with measured input, SAE Technical Paper.

VAN ORMAN, J., J. KERWIN, S. VIDHATE, B. DÁVILA-MONTERO, R. MEJIA-ALVAREZ, D. PERL AND A. WILLIS (2020). Sulcal Cavitation During Head Impact and Correlating with Mild Traumatic Brain Injury Neuropathology (4372), AAN Enterprises.

VASAVADA, A. N., S. LI AND S. L. DELP (2001). "Three-dimensional isometric strength of neck muscles in humans." Spine **26**(17): 1904-1909.

VIANO, D. C., I. R. CASSON AND E. J. PELLMAN (2007). "Concussion in professional football: biomechanics of the struck player—part 14." Neurosurgery **61**(2): 313-328.

WHITE, D., G. CURRY AND R. STEVENSON (1978). "The acoustic characteristics of the skull." Ultrasound in medicine & biology **4**(3): 225-252.

WHITE, P., G. CLEMENT AND K. HYNYNEN (2006). "Longitudinal and shear mode ultrasound propagation in human skull bone." Ultrasound in medicine & biology **32**(7): 1085-1096.

WREDE, A. (2019). "Controlled cavitation design and investigation of its effect in traumatic-brain injuries."

YOUNG, F. R. (1989). Cavitation. Berkshire, UK, McGraw-Hill Book Company.

YOUNG, J. W. (1993). Head and face anthropometry of adult US civilians, FEDERAL AVIATION ADMINISTRATION WASHINGTON DC OFFICE OF AVIATION MEDICINE.

YU, A. W. (2019). Blast-Induced Neurotrauma and the Cavitation Mechanicsm of Injury, Duke University.

ZHONG, P., I. CIOANTA, F. H. COCKS AND G. M. PREMINGER (1997). "Inertial cavitation and associated acoustic emission produced during electrohydraulic shock wave lithotripsy." The Journal of the Acoustical Society of America **101**(5): 2940-2950.

ZHONG, P., Y. ZHOU AND S. ZHU (2001). "Dynamics of bubble oscillation in constrained media and mechanisms of vessel rupture in SWL." Ultrasound in medicine & biology **27**(1): 119-134.

ZHU, S., F. H. COCKS, G. M. PREMINGER AND P. ZHONG (2002). "The role of stress waves and cavitation in stone comminution in shock wave lithotripsy." Ultrasound in medicine & biology **28**(5): 661-671.

Biography

Christopher Eckersley attended Duke University as an undergraduate earning a dual degree in Biomedical and Mechanical Engineering in May of 2016. In the fall of 2016, he returned to Duke University for graduate school in the Injury Biomechanics Laboratory under Dr. Cameron R. 'Dale' Bass. In pursuit his PhD, Christopher earned a Masters of Science in Biomedical Engineering in December of 2018. In April 2021, Christopher defended his doctoral thesis, earning his PhD in Biomedical Engineering.

Refereed Manuscripts:

Eckersley CP, Op't Eynde L, Abrams MZ, Yu AW, Li M, Yao J, Bass CR (2020) *Acoustic Detection of Blunt Induced Cavitation in the Head.* International Research Council on Biomechanics of Injury Proceedings 2020

Eckersley CP, Nightingale RW, Luck JF, Bass CR (2019) *The Role of Cervical Muscles in Mitigating Concussion.* Journal of Science and Medicine in Sport, vol. 22(6)

Eckersley CP, White TR, Cutcliffe HC, Shridharani JK, Wood GW, Bass CR (2018) *Comparing Foul Tip Impact Attenuation of Baseball Catcher Masks Using Head Impact Metrics.* PLOS One, vol. 13(6)

Eckersley CP, Cox CA, Ortiz-Paparoni MA, Lutz RH, Sell TC, Bass CR (2018) *A Real Pain in the Neck: Design Limits on Magnitude and Location of Head Supported Mass.* Personal Armour Systems Symposium 2018: Proceedings

Eckersley CP, Nightingale RW, Luck JF, Bass CR (2017) *Effect of Neck Musculature on Head Kinematic Response Following Blunt Impact.* International Research Council on Biomechanics of Injury Proceedings 2017

Op't Eynde J, Yu AW, **Eckersley CP**, Bass CR (2020) *Primary blast wave protection in combat helmet design: A historical comparison between present day and World War I.* PLOS One, vol. 15(2)

Op't Eynde J, **Eckersley CP**, Bass CR (2019) *High-Rate Viscoelastic Shear Model of Porcine Skin, Lung and Liver Tissue.* International Research Council on Biomechanics of Injury Proceedings 2019

Op't Eynde J, Yu AW, **Eckersley CP**, Bass CR (2018) *The Lessons of History: Helmets and Primary Blast.* Personal Armour Systems Symposium 2018: Proceedings

Cox CA, Ortiz-Paparoni MA, Schmidt AL, Shridharani Jk, Salzar RS, **Eckersley CP**, Bass CR (2018) *Men and Women and Helmets and Necks*. Personal Armour Systems Symposium 2018: Proceedings

McGovern B, Luck JF, Gade A, Lake IV, O'Connell D, Cutcliffe HC, Shah KP, Ginalis EE, Lambert CM, Christian N, Kait JR, Yu AW, **Eckersley CP**, Bass CR (2017) *Memory-Guided Oculomotor Task in High School Football Players with ADHD, Post-Concussive Injuries, and Controls.* International Journal of Sport and Health Science